ABSTRACT

Title: DIRECT NUMERICAL SIMULATION OF NON-PREMIXED COMBUSTION WITH SOOT AND THERMAL RADIATION

Yi Wang, Ph.D., 2005

Directed By: Professor A. Trouvé, Department of Fire Protection Engineering

Direct numerical simulation (DNS) is a productive research tool in combustion science used to provide high-fidelity computer-based observations of the micro-physics in turbulent reacting flows. It is also a unique tool for the development and validation of reduced model descriptions used in macro-scale simulations of engineering-level systems. Because of its high demand of computational power, current state-of-the-art DNS remains limited to small computational domains, small Reynolds numbers, and simplified problems corresponding to adiabatic, non-sooting, gaseous flames in simple geometries. This Ph.D. study is part of a multi-institution collaborative research project aimed at using terascale technology to overcome many of the current DNS limitations.

Two different tracks are followed in the present work: a DNS development track, and a DNS production track corresponding to a study of flame-wall interactions. Due to project management issues, the two tracks remain separate in this work. In the first track, we develop numerical and physical models to enhance the capability of our fully compressible DNS solver for turbulent combustion. The

Acoustic Speed Reduction (ASR) method is a new perturbation method designed to reduce the stiffness associated with acoustic waves found in slow flow simulations and to thereby enhance computational efficiency. The Navier-Stokes Characteristic Boundary Conditions (NSCBC) are modified to allow for successful simulations of turbulent counterflow flames. In addition, a semi-empirical soot model and a parallel thermal radiation model based on a ray-tracing method are developed and implemented into our DNS code. All the models are validated, showing that the capability of our DNS tool is greatly enhanced.

In the second track, we perform a DNS study of non-premixed flame-wall interactions. The structure of the simulated wall flames is studied in terms of a classical fuel-air-based mixture fraction and a new variable, called the excess enthalpy variable, which characterizes deviations from adiabatic behavior. Using the excess enthalpy variable, a modified flame extinction criterion is proposed and tested against DNS data.

While beyond the scope of this Ph.D. thesis, it is expected that follow-up studies of flame-wall interactions will take advantage of the new DNS software features developed in the first track of the present work.

DIRECT NUMERICAL SIMULATION OF NON-PREMIXED COMBUSTION WITH SOOT AND THERMAL RADIATION

By

Yi Wang

Dissertation submitted to the Faculty of the Graduate School of the
University of Maryland, College Park, in partial fulfillment
of the requirements for the degree of
Doctor of Philosophy
2005

Advisory Committee:
Professor Arnaud Trouvé, Advisor and Chair
Professor James Quintiere
Professor Ugo Piomelli
Professor Kenneth Yu
Professor James Baeder

Dedication

To my parents and my dear Chenchen

Acknowledgements

This work was supported by the Department of Energy, Office of Basic Energy Sciences, SciDAC Computational Chemistry Program (Grant No. DE-FG02-01ER15227). Interactions with other participants to our SciDAC project are gratefully acknowledged.

I am indebted to my advisor, Professor Arnaud Trouvé, for bringing me into the exciting field of combustion and fire science, for his careful guidance that ensures I receive a sound and fruitful education, and for his meticulous instructions, limitless patience and sustained encouragements. I appreciate everything Professor Trouvé has done for me from the bottom of my heart.

I am also grateful to my advisory committee and all the professors who have helped me with my research and study. Special thanks go to Professor Quintiere and Professor Piomelli for the wonderful classes they taught, and many helpful discussions on my research.

My study and research in the University of Maryland have greatly benefited from discussions with many fellow graduate students, among them, Dr. Nathasak Boonmee, Carlos Cruz, Jennifer Logue, Tingguang Ma, Ali Rangwala, Yunyong Utiskul, Dr. Kaoru Wakatsuki, Jianming Yang and Xiaobo Yao. Last but not least, I would specially thank Tingguang Ma for sharing with me his enormous knowledge in fire safety science and for inspiring me to work in this field.

Table of Contents

Dedication ii
Acknowledgements iii
Table of Contents iv
List of Figures vi
Chapter 1: Introduction 1
1.1. DNS of Reacting Flows 1
1.2. DNS Solver S3D 8
1.3. DNS Software Developments and DNS Studies 10
Chapter 2: ASR Method 11
2.1. Introduction 11
2.2. Theory 14
The Pressure Gradient Scaling (PGS) Method 15
The Acoustic Speed Reduction (ASR) Method 19
2.3. Results 23
Non-Reacting Flow Tests 23
Reacting Flow Tests 28
2.4. Conclusion 36
Chapter 3: Improved Characteristic Boundary Conditions 38
3.1. Introduction 38
3.2. Review of Navier-Stokes Characteristic Boundary Conditions 40
3.3. Application to Laminar Counterflow 46
The Original LODI Method 47
The LODI Method Enhanced by Multi-dimensional Effects 50
A Modified Nonreflecting Outflow Boundary Condition 56
Laminar Counterflow Flames 59
3.4. Application to Turbulent Counterflow 62
Nonreacting Turbulent Counterflow 63
Turbulent Counterflow Flames 65
3.5. Concluding Remarks 67
Chapter 4: Soot Model 69
4.1. Introduction 69
4.2. Semi-empirical Soot Models 71
4.3. Implementation in S3D and Validation 75
Chapter 5: Thermal Radiation 82
5.1. Introduction 82
5.2. Discrete Transfer Method 84
5.3. Parallelization of DTM 91
5.4. Implementation of Parallel DTM 93
5.5. Validation Tests for Parallel DTM Code 96
5.6. Coupled Radiation-CFD Simulations 109
5.7. Concluding remarks 111
Chapter 6: DNS of Non-Premixed Flame-Wall Interactions 113

6.1. Introduction 113
6.2. Numerical Configuration 117
6.3. DNS Results 124
Wall-Flame Structure 124
Wall-Flame Extinction 138
Wall Surface Heat Flux 144
6.4. Conclusion 145
Chapter 7: Conclusion and Future Directions 148
Appendices 151
A: Alternative Forms of the Energy Equation 151
B: A Mathematical Derivation of the ASR Transformation 153
C: An Extension of the Burke-Schumann Solution 160
Bibliography 166

List of Figures

Figure 2-1. Right-traveling acoustic wave without PGS or ASR. The simulation correspond to air at standard temperature and pressure conditions, T = 300 K, p = 1 atm. Figures (a) and (b) show the acoustic pressure and x-velocity perturbations versus spatial distance at 3 successive times; solid line: t = 0; dashed line: t = 7.2 μs; dash-dotted line: t = 14.4 μs. The perturbations travel across the (one-dimensional) computational domain at the speed of sound, $c \approx 348.0$ m/s. 24

Figure 2-2. Right-traveling acoustic wave with ASR (α = 10). The simulation conditions and plotting parameters are identical to those of Fig. 1. Solid line: t = 0; dashed line: t = 7.2 μs; dash-dotted line: t = 14.4 μs. The perturbations travel across the computational domain at an ASR-modified pseudo-speed of sound, $c \approx 34.8$ m/s. 24

Figure 2-3. Hydrostatic pressure variations versus vertical distance. The simulations correspond to air at standard temperature, pressure and gravity conditions, T = 300 K, p = 1 atm, $g_x = -9.81$ m/s^2 (gravity is pointing into the negative x-direction). Figure (a) presents results obtained both without PGS or ASR (solid line) and with ASR (dashed line, α = 10). Figure (b) presents results obtained with PGS (solid line, α = 10). Compared to Fig. (a), pressure variations in Fig. (b) are amplified by a factor α^2 = 100..... 26

Figure 2-4. Two-dimensional laminar Poiseuille flow configuration. The simulations correspond to air at standard temperature and pressure conditions, T = 300 K, p = 1 atm, moving steadily along the x-direction between 2 solid plates (located at y = 0 and 1 cm) and driven by a prescribed pressure drop between the duct inlet (x = 0) and outlet (x = 10 cm), $\Delta p_x \approx -0.22$ Pa. The bottom plot presents iso-contours of x-velocity and shows that the flow remains one-dimensional across the computational domain. The top insert presents a cross-stream x-velocity profile; this velocity profile features a classical parabolic shape and a y-averaged velocity $\bar{u} \approx 1$ m/s..... 27

Figure 2-5. Mass flow rate per unit depth in PGS- and ASR-modified simulations of a two-dimensional laminar Poiseuille flow (see figure 2-4). Top curve (circle symbols): ASR; bottom curve (square symbols): PGS. The figure shows that while the ASR-solution is insensitive to the value of α, the PGS-solution strongly depends on it. In PGS, the pressure-driven mass flow rate through the duct is incorrectly reduced by a factor α^2. 28

Figure 2-6. Two-dimensional laminar premixed flame configuration. The simulations correspond to an initially plane, steady, lean, methane-air flame perturbed by an incoming stoichiometric pocket. Methane-air combustion is described using single-step chemistry. The figure presents iso-contours of the initial methane mass fraction

distribution: the gray region on the left ($x < 0.7$ cm) corresponds to lean reactants ($\phi = 0.7$); the black round-shaped region near (x,y) ≈ (0.4 cm, 1 cm) corresponds to the stoichiometric perturbation ($\phi = 1$); the white region on the right ($x > 0.7$ cm) corresponds to combustion products ($Y_{CH4} = 0$). 30

Figure 2-7. Unsteady response of a lean, methane-air, laminar premixed flame to an incoming stoichiometric pocket (see figure 2-6). Iso-contours of the fuel mass reaction rate $\dot{\omega}_{CH4}$ obtained at time $t \approx 0.014$ s. $\dot{\omega}_{CH4}$ is expressed in cgs units (g/s-cm^3). Figure (a) presents results obtained without PGS or ASR; figure (b) presents results obtained with ASR ($\alpha = 10$). 31

Figure 2-8. Unsteady response of a lean, methane-air, laminar premixed flame to an incoming stoichiometric pocket (see figure 2-6). Iso-contours of the fluid temperature T obtained at time $t \approx 0.014$ s. T is expressed in Kelvin units (K). Figure (a) presents results obtained without PGS or ASR; figure (b) presents results obtained with ASR ($\alpha = 10$). 31

Figure 2-9. Unsteady response of a lean, methane-air, laminar premixed flame to an incoming stoichiometric pocket (see figure 2-6). Iso-contours of the x-velocity component u obtained at time $t \approx 0.014$ s. u is expressed in cgs units (cm/s). Figure (a) presents results obtained without PGS or ASR; figure (b) presents results obtained with ASR ($\alpha = 10$). 32

Figure 2-10. Unsteady response of a lean, methane-air, laminar premixed flame to an incoming stoichiometric pocket (see figure 2-6). The plot shows the time history of the total fuel mass reaction rate ($\dot{\omega}_{CH4}$ is space-averaged over the computational domain); solid line: without PGS or ASR; dashed line: with ASR ($\alpha = 10$). The total reaction rate is normalized by its initial value. 32

Figure 2-11. One-dimensional laminar premixed flame configuration. The simulations correspond to a plane, steady, lean ($\phi = 0.4$), hydrogen-air flame. Hydrogen-air combustion is described using detailed chemical kinetics. solid line: without PGS or ASR; dashed line: with ASR ($\alpha = 4$). The ASR curve has been arbitrarily shifted to the right to facilitate the comparison with the fully compressible curve. (a) The figure presents the temperature variations across the flame; (b) spatial variations of the OH mass reaction rate $\dot{\omega}_{OH}$ across the flame. $\dot{\omega}_{OH}$ is expressed in cgs units (g/s-cm^3)... 34

Figure 2-12. Structure of a lean, hydrogen-air, laminar premixed flame (see figure 2-11). The figure presents the pressure variations across the flame; solid line: without PGS or ASR; dashed line: with ASR ($\alpha = 4$). The ASR curve has been arbitrarily shifted to the right to facilitate the comparison with the fully compressible curve. ... 35

Figure 3-1. The configuration and initial condition for nonreacting counterflow tests. The solid lines represent streamlines and the arrows indicate the flow direction. 48

Figure 3-2. Temporal variations of the maximum and minimum pressure with the hard inflow boundary conditions. 48

Figure 3-3. Pressure and the x-directional velocity fields with nonreflecting inflow conditions at t = 10 msec. 49

Figure 3-4. Pressure and x-directional velocity fields for the three test cases at t = 10 msec. 54

Figure 3-5. Temporal variations of the maximum pressure and the mean inlet velocity at x = 0 for Cases (a)–(c)..... 56

Figure 3-6. The steady pressure and x-directional velocity fields using modified non-reflecting outflow boundary conditions equation (3.23) with a = 0.01. The inflow velocity is 30 m/s. 59

Figure 3-7. The steady H_2-air nonpremixed counterflow: (a) streamlines (solid) and temperature (dotted) and (b) pressure isocontours..... 61

Figure 3-8. The temperature and x-directional velocity profiles of the initial and steady H_2-air nonpremixed counterflow flame. 62

Figure 3-9. The temporal variations of (a) the imposed and calculated velocities and (b) the minimum pressure at $x = 0$ and $y = l_y/2$ for a nonreacting counterflow for various choices of a. 64

Figure 3-10. The temporal evolution of vorticity (top) and temperature (bottom) fields in hydrogen-air nonpremixed counterflow. From left to right, t = 0.1, 0.3, and 0.8 msec. 66

Figure 3-11. The temporal variations of the maximum and minimum pressures for turbulent nonpremixed counterflow flame..... 67

Figure 3-12. Scatter plot of temperature versus scalar dissipation rate χ along the stoichiometric line at t = 0, 0.1, 0.3, and 0.8 msec. 67

Figure 4-1. Steady solution of the laminar counterflow diffusion flame. Red solid line: streamwise velocity; Green solid line: temperature; Blue dash-dotted line: soot volume fraction; Purple dashed line: source term in soot mass fraction equation. Last three quantities are non-dimensionalized for a better illustration..... 78

Figure 4-2. Comparison of S3D soot quantities with experimental and reference computational data. The S3D predictions use the original model coefficients. (a): soot number density. (b): soot volume fraction. 79

Figure 4-3. Comparison of computed soot quantities with experimental and computational data. Modified model coefficients are used. (a): soot number density. (b): soot volume fraction. 81

Figure 5-1. Illustration of the domain decomposition and the ray tracing technique in the Discrete Transfer Method. 86

Figure 5-2. Illustration of computation of the radiative source term in the Discrete Transfer Method..... 89

Figure 5-3. Illustration of a domain decomposition parallelization scheme..... 92

Figure 5-4. Illustration of the geometry of test case 1. 96

Figure 5-5. Test case 1: nondimensional wall radiative heat flux for three different optical thickness cases. (a) $\kappa L=0.1$ (b) $\kappa L=1.0$ (c) $\kappa L=10.0$. 97

Figure 5-6. Test case 1: Nondimensional wall radiative heat flux calculated using different number of processors (1,2,4,9): $\kappa L=1.0$..... 98

Figure 5-7. Test case 1: Distribution of the radiative power density (w/m^3) calculated using different number of processors: $T_g=1000k$, $\kappa L=1.0$. a) single processor b) four processors. 99

Figure 5-8. Convergence test. Results are obtained using 256 rays for DTM and 64 processors for parallel computations. The dashed curve is for the DTM computation at the first time step of the CFD simulation, and the solid curve is for the second time step. 102

Figure 5-9. Convergence test. Results are obtained using 256 rays for DTM and 64 processors for parallel computations. The dashed curve: convergence criterion. The solid curve: total radiative heat loss..... 102

Figure 5-10. Number of iterations needed for DTM using different number of processors. Results shown are for the first time step. Number of rays per boundary cell: 256..... 103

Figure 5-11. Scalability test for the DTM solver. Wall-clock time recorded is the time used for DTM solver for the first time step in a DTM-CFD coupled simulation..... 103

Figure 5-12. Test case 2: Spatial variations of the radiative power density normal to the flame. Comparison between DTM, DOM, and the optically thin model..... 106

Figure 5-13. See the caption of figure 5-9. The plank mean absorption coefficient κ is modified to achieve a different optical thickness. (a): κ is increased to 10 times the original value. (b): κ is increased to 100 times the original value. 107

Figure 5-14. Ray refinement test for DTM. Data are also compared with OTM and DOM (S2-S8 approximation). Numbers of rays used for DTM are 6×6, 8×8, 10×10, 12×12, 16×16, 20×20 and 26×26. First row ((a) and (b)): using the true value of κ. Second row ((c) and (d)): κ is increased 10 times. Third row ((e) and (f)): κ is increased 100 times. Figures in the left column ((a), (c) and (e)): volume integrated

radiative power. Figures in the right column ((b), (d) and (f)): relative error compared with the results computed by DTM with 900 rays. 108

Figure 5-15. Snapshots of temperature (flood) and vorticity (black lines) isocontour for four consequent time instants. From left to right, t = 0, 3, 5, and 15 msec. 110

Figure 5-16. Temporal variations of (a) the total heat release rate, and (b) radiative fraction. 111

Figure 5-17. Comparison of the time variation of the total heat release rate between DTM and OTM. 111

Figure 6-1. Flame response to changes in the fuel-air mixing rate in a steady, one-dimensional, plane, laminar, diffusion counter-flow flame configuration. The top curve (squares) corresponds to numerical data obtained with OPPDIF using detailed chemistry [147] and molecular transport; the bottom curve (triangles) corresponds to numerical data obtained with S3D and using single-step chemistry (equations (6-1)-(6-2)) and unity Lewis numbers. 119

Figure 6-2. Numerical configuration corresponding to a turbulent ethylene-air diffusion flame stabilized near a solid wall. The computational domain is two-dimensional and features a turbulent inflow boundary at x = 0 (flow is from left to right); a solid wall boundary at y = 0; and non-reflecting boundaries at x = 8 cm and y = 4 cm. The turbulent inflow boundary is used both for air and fuel injection. The plot shows a typical snapshot of temperature iso-contours and is taken from a simulation in which the wall is assumed adiabatic. 121

Figure 6-3. Instantaneous spatial variations of: (a) fluid temperature (in units of K); (b) fuel mass reaction rate (in units of kg/m^3/s). Figure (c) presents the location of the corresponding stoichiometric iso-contour of the fuel-air-based mixture fraction Z. Case 1 solution. 126

Figure 6-4. see caption of figure 6-3. Case 2 solution. 127

Figure 6-5. see caption of figure 6-3. Case 3 solution. Two wall-induced flame extinction events are observed in figure (b), near (x = 0.8 cm; y = 0.2 cm) and (x = 5.5 cm; y = 0.2 cm). Figure (c) also presents the spatial variations of the excess enthalpy variable H. 128

Figure 6-6. Scatter plot of temperature versus fuel-air-based mixture fraction. Case 2 solution. The DNS data correspond to an arbitrarily chosen time in the simulation, and are compared to two reference curves: the adiabatic Burke-Schumann solution (squares, equation (C4)), and one laminar flame profile (circles). The laminar profile corresponds to a steady, one-dimensional, plane, laminar counter-flow flame, with χ_{st} = 36.3 s^{-1}. 130

Figure 6-7. Scatter plot of flame temperature versus fuel-air mixing rate. Case 2 solution. The DNS data correspond to an arbitrarily chosen time period of 10 ms in

the simulation, and are compared to reference data points (circles). The reference data points correspond to steady, one-dimensional, plane, laminar counter-flow flames. 132

Figure 6-8. Scatter plot of temperature versus fuel-air-based mixture fraction. Case 4 solution. The DNS data correspond to an arbitrarily chosen time in the simulation, and are compared to the adiabatic Burke-Schumann solution (squares, equation (C4)). 134

Figure 6-9. Scatter plot of flame temperature versus fuel-air mixing rate. Case 4 solution. The DNS data correspond to an arbitrarily chosen time period of 10 ms in the simulation, and are compared to reference data points (circles). The reference data points correspond to (adiabatic) steady, one-dimensional, plane, laminar counter-flow flames. 134

Figure 6-10. Scatter plots of flame temperature versus fuel-air-based mixture fraction. Case 3 solution. The DNS data correspond to a time in the simulation that is flame-extinction-free, and to three different x-locations: (a) $x = 0$; (b) $x = 1.97$ cm; (c) $x = 7.9$ cm. The DNS raw data (diamonds) are also compared to the adiabatic Burke-Schumann solution (solid line, equation (A4)), and to reference data (squares) processed according to the extended Burke-Schumann solution in equation (6-4).. 137

Figure 6-11. Flame extinction detection scheme. The scheme consists in monitoring the variations of the flame weakness factor, $R = (\chi_{st} / \chi_{st,ext}) \approx (\chi_{st} / \chi_{st,ext}^{ad}) \times \exp(-\beta H_{st})$. The upper plot shows the flame location in physical space while the lower plot shows the corresponding variations of R as a function of arc length along the flame contour. The flame weakest spots are readily identified as peak values of R in the lower plot, and flame extinction is predicted to occur for R above a critical value (*i.e.* $R \geq 1$ in equation (6-7)). 141

Figure 6-12. Variations of the flame temperature T_{st} with the flame weakness factor R, at selected flame locations. Case 2 (triangles) and case 4 (lines) solutions. The DNS data correspond to several flame weak spots, as identified using the detection algorithm presented in figure 6-11. The DNS data are compared to reference data points (circles). The reference data points correspond to (adiabatic) steady, one-dimensional, plane, laminar counter-flow flames. 143

Figure 6-13. Probability density function (PDF) of the wall surface heat flux. Case 3 (solid line) and case 4 (dashed line) solutions. The PDF data are accumulated both in space, along the entire wall surface at $y = 0$, and in time, over a time period of 20 ms. 145

Chapter 1: Introduction

1.1. DNS of Reacting Flows

With the fast development of modern computers and advanced computational methods, numerical simulations have acquired an important role in almost every scientific and engineering discipline. In particular, computational fluid dynamics (CFD) has been widely utilized as a supplement or even replacement of the traditional, oftentimes very expensive, experiments in both scientific study and engineering applications. Successful applications of CFD can be found in different fields including mechanical engineering, chemical engineering, aeronautics and astronautics, environmental sciences, bio-engineering, etc.

Based on how we treat the turbulence, there are hierarchies of solution methods to the Navier-Stokes equations [1]: Reynolds-averaged Navier-Stokes simulation (RANS), large eddy simulation (LES) and direct numerical simulation (DNS). RANS solves averaged N-S equations, and is usually limited to steady problems (or leads to difficulties when applied to unsteady problems). The effects of turbulent fluctuations that appear in Reynolds stresses are modeled, and the computational resource requested by RANS is relatively limited. LES is a higher-level numerical approach to turbulent flows. It resolves turbulent eddies that are large on the computational grid, while it models the effect of eddies that are smaller than the grid size [2, 3]. The large-scale motions are usually greatly affected by the flow geometry and contain most of the kinetic energy of the turbulent flow, while the small-scale eddies tend to be more homogeneous and universal, therefore easier to

model. The computational cost for LES is considerably higher than in RANS, since it requires a fairly fine mesh and provides three-dimensional and time dependent solution. It is especially true for wall-bounded turbulent flows, where the computational cost of LES is highly dependent on the Reynolds number [4]. Recently LES/RANS have been applied to real full-scale engineering problems with complex geometries, for example: flow over an aircraft [5], combustion inside a gas turbine [6], large scale fires in a building [7], etc. Although some of the simulations are somewhat under-resolved and the models used still questionable, they do illustrate the state-of-the-art of CFD and reflect the urgent needs for engineering applications.

DNS directly descretizes the Navier-Stokes (N-S) equations and solves them numerically [1]. All the turbulent length scales, from the integral scale down to the Kolmogrov scale, are resolved on the fine grid. DNS is considered as a numerical experiment and provides great amount of valuable data that are not fully available from experimental measurements: velocities, pressure, scalars, as well as their variations in space and time. However due to the expensive computational cost, DNS is restricted to low Reynolds numbers and simple geometries. The applications of DNS to the building-block turbulent flow configurations, like isotropic decaying turbulence [8], boundary layer [9], channel flow [10, 11] etc., have provided new insights into the turbulent flow physics and also the databases used to assess and develop models for LES and RANS.

CFD of reacting flows is an active research area for both combustion and fire science. Compared with non-reacting flows, numerical simulations of turbulent combustion are more difficult. First of all, the energy equation is inevitably coupled

with the momentum equations due to the large chemical heat release. In addition, a large number of scalar mass species equations are usually required to treat the gas-phase chemical reaction with reasonable accuracy. (Pollutant predictions, like NOx and soot, require more complex descriptions of the chemistry.) Also, thermal radiation is not negligible at the typically high flame temperatures. Both chemical reaction and radiative heat transfer are highly non-linear processes, and impose extra difficulties in turbulence models for reacting flows. Most turbulent combustion models have some *ad hoc* nature, and are not adequate to treat turbulent flames with complex phenomena, like ignition, extinction, flame-wall interactions and so on. Therefore, DNS emerges as a useful research tool to provide high-fidelity computer-based observations of the micro-physics in turbulent reacting flows, and help developing reduced model descriptions used in macro-scale simulations of engineering-level systems [12, 13].

In DNS, we directly discretize Navier-Stokes equations and solve them numerically. However, even for non-reacting flows, the high computational cost dictates that DNS has to be limited to low Reynolds number cases. For reacting flows, it is just simply not feasible with current computational resources to include in a single simulation all the known physics, like thermal/acoustic dilatation, realistic three-dimensional turbulence, detailed chemical kinetics, thermal radiation, etc. Simplifications in certain aspects are usually adopted to make the simulations tractable. The simplifying assumptions used vary from one study to another, for example: constant density or variable density flow, two-dimensional or three-dimensional configuration, single-step chemistry or detailed kinetics, neglecting

thermal radiation or not, and so on. The choice of the DNS formulation is a trade-off between the objectives of a specific study and the available computer resources. The DNS data therefore have limitations, but on the other hand, they do increase our understanding of the complicated micro-scale physics in turbulent combustion.

Early attempts in DNS of reacting flows used a single-step global chemistry and a constant density assumption, so that available numerical codes developed for non-reacting incompressible turbulent flow could be directly used and the temperature and mass species equations are resolved in a post-processing stage. The feedback of chemical heat release to the turbulent field is neglected in these studies and the focus is on the effect of turbulence on the flame topology and structure. Rutland and Trouvé [14] used this assumption to study a premixed flame propagating through decaying three-dimensional isotropic turbulent flow. The constant density assumption was also adopted recently in studies of more complex problems like nonpremixed flames near extinction [15], premixed flame-wall interactions in a turbulent channel flow [16], and extinction/reignition in a diffusion flame [17].

Most current DNS studies adopt a variable density formulation, however some use a two-dimensional configuration to reduce the computational overhead brought by other complexities, like variable density [18] or a detailed treatment of the chemical kinetics [19-21]. Two-dimensional configurations are not suitable for non-reacting DNS, since the vortex stretching mechanism responsible for the turbulent kinetic energy cascade is intrinsically three-dimensional. However it remains quite valuable when studying flame responses to turbulence-like random fluctuations, because the local reaction zones retain a one-dimensional laminar structure in the

flamelet regime [22], and also because the probability of finding locally cylindrical (2D) flame sheets is much higher than that of 3D spherical flame surfaces [12]. In general, two-dimensional simulations are typically justified when three-dimensional simulations are out of the reach of available computational resources. Two-dimensional configurations are also used for parametric studies as in reference [23] or as a first try in making observations of new physics, for instance: auto-ignition [20] and detailed chemistry effect of H_2 enrichment on lean premixed methane-air flame [21], etc.

DNS data for premixed combustion are usually analyzed in the framework of flamelet theory [24]. In the flamelet combustion regime, chemical reaction takes place in thin layers designated as flamelets which are convected and distorted by the turbulent flow field but retain their laminar flame structure. Therefore flame wrinkling is the major mechanism responsible for the increase in turbulent flame speed. Trouvé and Poinsot [25] examined the wrinkling effect of turbulence on the flame surface in a configuration of a premixed flame embedded in an isotropic decaying turbulence field. Using DNS data, they evaluated the different terms appearing in the flame surface density equation. Zhang and Rutland [26] focused on a different aspect of flame-turbulence interactions: the effect of the flame on the turbulent flow. In their study, turbulence was introduced from the inlet boundary, so that a stationary turbulent premixed flame can be maintained inside the computational domain (the equivalent of a numerical wind tunnel). The authors found that the heat release greatly increases turbulent kinetic energy. From the analysis of the turbulent kinetic energy budget, they concluded that pressure related terms are the major

mechanism that represents the flame effect on turbulence. Veynante et al. [23] studied the turbulent flux of the mean reaction progress variable and the flame surface density. Their study revealed the existence of two different regimes for turbulent transport: counter-gradient diffusion occurs when the flow field new the flame is dominated by thermal dilatation, whereas gradient diffusion occurs when the flow field near the flame is dominated by the turbulent motions. The flamelet concept generally requires chemical reaction to occur at fast time-scales and short length-scales relative to the turbulence. This regime was identified in a premixed turbulent combustion diagram by Poinsot et al. [18] from a series of DNS of premixed flame vortex interactions, where the flame is interacting with vortices with well defined length and velocity scales.

Turbulent non-premixed flames in the flamelet regime were also studied with DNS. Chen and Kollmann [27] simulated an initially planar and unstrained laminar diffusion flame interacting with decaying homogeneous turbulence. They examined the shape and the wrinkling of the iso-mixture-fraction surfaces, and found that the wrinkling of mixture fraction surfaces is reduced by heat release effects. Bédat et al. [28] performed both two-dimensional and three-dimensional DNS of a similar configuration with reduced chemistry. They found that the flamelet viewpoint was adequate to describe the heat release process, but not as successful for NO_x formation. Van Kalmthout and Veynante [29] analyzed the flame surface density models for nonpremixed flames in a two-dimensional spatially-developing turbulent reacting mixing layer. Various terms contributing to the transport equation of flame surface density were evaluated using DNS data. Similar to what was done earlier for

premixed flames, Cuenot and Poinsot [30] performed a DNS study of diffusion flame-vortex interactions and proposed a diagram delineating the laminar flamelet region, an unsteady effect region, a curvature effect region and a quenched region.

Recently more complex combustion phenomena have been studied by DNS, including auto-ignition [20, 31], extinction and reignition [17], triple flame and partially premixed flame [32, 33], flame-wall interaction [16, 34], spray combustion [35, 36], etc.

The growth and progress in DNS of turbulent reacting flows are very encouraging. However our ability to accurately simulate interesting combustion problems is now constrained by two aspects: first, the high demand for computational power; second, the lack of an adequate numerical description of some complex physics: for instance, an accurate mechanism for soot formation, a numerical treatment of radiative heat transfer and liquid fuel sprays, etc. Current (gigascale) state-of-the-art DNS remains limited to small computational domains and to simplified problems corresponding to adiabatic, non-sooting, gaseous flames in simple geometries. The objective of the current project is to enhance the current DNS capability with new numerical and physical modeling capabilities for tera-scale computing platforms. With the new developments, we hope to extend the domain of application of DNS to new problems with more complex physics, or to compute the same problems with more efficiency. The current study is part of a multi-institutional collaboration with University of Michigan, University of Wisconsin and Sandia National Laboratory [37]. Different groups share the same software platform, but have responsibilities of different developments. We will, in the following section,

introduce our DNS solver, followed with a description of the content of current Ph.D. study.

1.2. DNS Solver S3D

Our current DNS code, called S3D, is a fully compressible Navier-Stokes solver. It solves the governing equations for gaseous, multi-component, reacting flows as the following:

$$\begin{cases} \dfrac{\partial \rho}{\partial t} + \dfrac{\partial}{\partial x_j}(\rho u_j) = 0 & (1.1) \\ \dfrac{\partial}{\partial t}(\rho Y_k) + \dfrac{\partial}{\partial x_j}(\rho Y_k u_j) = -\dfrac{\partial}{\partial x_j}(\rho Y_k V_{k,j}) + \dot{\omega}_k, \quad 1 \le k \le N_s & (1.2) \\ \dfrac{\partial}{\partial t}(\rho u_i) + \dfrac{\partial}{\partial x_j}(\rho u_i u_j) = -\dfrac{\partial p}{\partial x_i} + \dfrac{\partial \tau_{ij}}{\partial x_j} + \rho g_i, \quad 1 \le i \le 3 & (1.3) \\ \dfrac{\partial}{\partial t}(\rho E) + \dfrac{\partial}{\partial x_j}(\rho E u_j) = -\dfrac{\partial}{\partial x_j}(p u_j) + \dfrac{\partial}{\partial x_j}(\tau_{ij} u_i) - \dfrac{\partial q_j}{\partial x_j} + \rho g_j u_j & (1.4) \end{cases}$$

where t is time, x_j the spatial coordinate in the j-direction, ρ the mass density, u_j the j-component of flow velocity, Y_k the species k mass fraction, $V_{k,j}$ the j–component of molecular diffusion velocity for species k, $\dot{\omega}_k$ the species k mass reaction rate, p the pressure, τ_{ij} the ij-component of the viscous stress tensor, g_i the i-component of gravity acceleration, E the total energy per unit mass (internal energy plus kinetic energy) and q_j the heat flux vector. Equation (1.2) is written for $1 \le k \le N_S$, where N_S is the total number of species in the gaseous mixture; equation (1.3) is written for all 3 components of momentum, $1 \le i \le 3$. Assuming Newtonian fluid behavior, τ_{ij} is linearly related to the velocity gradient tensor:

$$\tau_{ij} = \mu\left(\frac{\partial u_i}{\partial x_j} + \frac{\partial u_j}{\partial u_i} - \frac{2}{3}\delta_{ij}\frac{\partial u_k}{\partial x_k}\right). \tag{1.5}$$

Furthermore, in equation (1.4), E and q_j are defined as follows:

$$\begin{cases} E = e + \left(\dfrac{u_j u_j}{2}\right) = \left(\displaystyle\sum_{k=1}^{N_s} h_k Y_k - \frac{p}{\rho}\right) + \left(\frac{u_j u_j}{2}\right), \\ h_k = h_k^0 + \displaystyle\int_{T_0}^{T} c_{p,k} dT, \\ q_j = -\lambda\dfrac{\partial T}{\partial x_j} + \rho\displaystyle\sum_{k=1}^{N_s} h_k Y_k V_{k,j} + q_{r,j}, \end{cases} \tag{1.6}$$

where h_k is the total enthalpy per unit mass (chemical enthalpy plus thermal enthalpy), h_k^0 the chemical enthalpy of formation (evaluated at reference temperature T_0) and $c_{p,k}$ the specific heat at constant pressure, all 3 quantities referring to species k; and where λ is the mixture thermal conductivity, T the temperature, $q_{r,j}$ radiative heat flux. Finally, equations (1.1)-(1.4) also require the equation of state. We assume that the fluid is ideal gas:

$$p = \rho R T \sum_{k=1}^{N_s} \frac{Y_k}{M_k} = \rho\left(\frac{R}{M}\right)T, \tag{1.7}$$

where R is the ideal gas constant, M_k the molecular weight of species k and M the molecular weight of the gaseous mixture.

S3D solves the above equations in discretized form on a Cartesian rectangular grid. It uses an eighth order central finite difference scheme [38] for spatial discretization. The high order scheme is non-dissipative and ensures the high fidelity of the direct numerical simulation. The time advancement method is a fourth order, six stage, low storage, explicit Runge-Kutta scheme [39]. Because the time

advancement scheme is fully explicit, the time step is constrained by acoustic and convective Courant-Friedrichs-Lewy (CFL) stability condition, as well as diffusive Fourier stability condition and conditions associated with the resolved chemical time scale. The characteristic-based boundary conditions [40, 41] are satisfied. One-sided finite difference schemes with reduced order of accuracy are used near the boundary to represent spatial derivatives. At the boundary cells, the accuracy is reduced to third order. S3D has a CHEMKIN compatible description of chemical kinetics [42]. And it is a massively parallel code based on domain decomposition using Message Passage Interface (MPI) libraries.

1.3. DNS Software Developments and DNS Studies

The present Ph.D. work has two separate tracks. In the first track, numerical and physical models are developed to enhance the DNS capability of S3D. The new developments include a pseudo-compressibility method that alleviates the acoustic stiffness of the fully compressible formulation (chapter 2), a new boundary condition scheme that allows turbulent counterflow flame simulations (chapter 3), a two-equation semi-empirical soot formation model (chapter 4), and a parallel thermal radiation solver based on a ray-tracing method (chapter 5). In the second track, S3D is applied to study an interesting combustion phenomenon: turbulent non-premixed flame-wall interactions (chapter 6). The DNS study of flame-wall interactions does not take advantage of the new features developed in the first track. However, follow-up studies will benefit from the new developments and thereby achieve more efficient and more realistic simulations.

Chapter 2: ASR Method

2.1. Introduction

Different mathematical formulations may be found in the literature for the DNS description of the flow and combustion processes. These formulations correspond to different degrees of complexity in the treatment of chemistry and molecular transport, as well as to different choices made in the handling of flow compressibility. The choice of an adequate formulation is a key step in many studies, aimed at optimizing, for a given particular problem, the trade-off between performance, accuracy and computational cost.

We consider in this chapter the problem of how to handle flow compressibility. We consider this problem in the context of a DNS solver with an explicit time integrator, at least for the treatment of convective transport. In DNS, explicit or semi-explicit integration is the preferred approach for time advancement as the associated stability time step restriction serves to guarantee adequate resolution and high-levels of accuracy. In this context, while a fully compressible formulation has the capability of treating a large range of flow problems (from subsonic to supersonic), it is also severely constrained by the need to resolve fast acoustic wave motions and is therefore not well suited to treat low Mach number problems characterized by widely different flow and acoustic speeds.

A number of methods have been proposed in the literature to remove or modify the acoustic time step restriction found in fully compressible, explicit formulations [43]. One class of methods is the zero Mach number approach where the mathematical formulation of the flow problem is modified in order to filter out

acoustic waves [44-48]. The zero Mach number approach is computationally efficient for slow flow problems but this efficiency is achieved at the cost of a reduced domain of application (the flow must remain in the incompressible regime, *i.e.* flow Mach numbers must remain below 0.3) and of an increased complexity in the numerical algorithms. The increased complexity results from: the decomposition of the pressure variable into a spatially-invariant thermodynamic component (often a constant) and an aerodynamic component; the subsequent handling of aerodynamic pressure variations via a Poisson equation; and the taxing demand of an elliptic solver to invert the Poisson problem.

Other methods generally retain some form of compressibility and thereby preserve the original hyperbolic character of the governing equations. One approach seeks to exploit the flexibility found in operator splitting techniques and consists in applying an implicit time integration treatment to the "ill-conditioned" compressible part of the flow dynamics while maintaining an explicit treatment for convective transport. An example of this approach is the Barely Implicit Correction (BIC) method proposed in [49]. Acoustic motions are still present in the BIC method, but computational efficiency is increased by withdrawing the initial demand for a representation of acoustic signals within the explicit stability boundaries.

An alternative approach is the artificial compressibility or pseudo-compressibility approach [50, 51]. In this approach, the governing equations are manipulated prior to a numerical treatment in order to modify the acoustic wave physics. In [50], Choi & Merkle propose to differentiate between the following two sub-categories: (1) preconditioning methods where the time derivatives in the original

compressible system of equations are pre-multiplied by a matrix that provides artificial control of the system eigenvalues, *i.e.* artificial control of the travel speeds of acoustic modes; (2) perturbation methods where the right-hand-side of the governing equations are modified according to some suitable scaling arguments with the effect that acoustic waves are again replaced by slower-moving pseudo-acoustic modes. These two sub-categories share many similarities and achieve increased efficiency by decreasing the gap between flow and acoustic speeds. Preconditioning methods adopt an applied mathematics view point and start from a classical spectral analysis of the partial differential equations, while perturbation methods borrow more from a fluid mechanics view point and start from series expansions of the flow variables in terms of a characteristic Mach number.

Our objective in the present study is to evaluate the potential of pseudo-compressibility methods in the context of our DNS solver S3D. We consider in the following the pseudo-compressibility methods proposed in [52, 53]. These methods are perturbation methods in the terminology introduced by Choi & Merkle [50] and are particularly attractive since they may be implemented with relatively modest effort (*i.e*. limited software modification) in a flow solver where a fully compressible formulation is adopted. In [52], O'Rourke & Bracco propose to artificially increase the flow and flame Mach numbers using a scaling transformation applied to the problem variables. A related study by Ramshaw, O'Rourke & Stein [53] proposes a slightly different method, called Pressure Gradient Scaling (PGS). PGS is based on a straightforward modification of the pressure gradient in the momentum equation. This modification results in an artificial decrease of acoustic speeds and allows again for a

more efficient computation. Both methods in [52, 53] use a re-scaling of pressure perturbations and a side effect is that pressure variations are dramatically amplified: if the acoustic speed is decreased by a factor α, pressure variations are amplified by a factor α^2. While insignificant for problems with nearly homogeneous pressure, this side-effect leads to difficulties in the case of problems with external pressure gradients, for instance ducted flow problems.

We consider in the present study a variation of the PGS method with the objective of extending the method to the case of problems with external pressure gradients. The original and modified PGS methods are presented in section 2.2. Both methods are implemented into S3D and evaluated in a series of benchmark flow and flame problems in section 2.3.

2.2. Theory

Government equations for compressible reacting flow (equations (1.1)-(1.4)) contain a range of time scales associated with convective, diffusive, reactive as well as acoustic phenomena. Time accurate simulations of reacting flows call for adequate time resolution of convection, diffusion and chemical reaction but in many cases, do not require fine resolution of the acoustic physics. In S3D, however, time integration is based on a high-order explicit Runge-Kutta scheme that cannot discriminate between relevant and irrelevant dynamics. While fully explicit time integration has attractive features such as simplicity, ease-of-use and efficient parallel computing implementation, one well-known drawback is that fast acoustic motions contribute to, and often dominate the stability time step limitation. For instance, the time step Δt is restricted in S3D by a classical Courant-Friedrichs-Lewy (CFL) condition:

$$\Delta t \le CFL \times \underbrace{\min}_{\substack{1\le j\le 3 \\ \text{all nodes}}} \left(\frac{\Delta x_j}{|u_j + c|}; \frac{\Delta x_j}{|u_j - c|} \right), \tag{2.1}$$

where min(Q) designates the minimum value of a quantity Q over all 3 spatial directions and all computational nodes; and where Δx_j is the local spatial increment of the computational grid in the j-direction, c the local speed of sound, and CFL a number that depends on the stability properties of the numerical scheme and is of order 1. Equation (2.1) may be re-written as:

$$\Delta t \le CFL \times \underbrace{\min}_{\substack{1\le j\le 3 \\ \text{all nodes}}} \left(\frac{\Delta x_j}{|u_j|} \times \frac{|Ma_j|}{|1 + Ma_j|} \right), \tag{2.2}$$

where $Ma_j = (u_j/c)$ is the local flow Mach number in the j-direction. In incompressible flow problems, Ma_j is a small quantity and equation (2.2) shows that Δt is in that case approximately proportional to Ma_j. Hence, as $Ma_j \rightarrow 0$, the acoustic stability constraint in equations (2.1)-(2.2) leads to a dramatic decrease in computational efficiency.

The Pressure Gradient Scaling (PGS) Method

The loss of computational efficiency is discussed in the following as a stiffness problem since it is a direct consequence of flow and acoustic speeds being widely different. The PGS method of [53] proposes to reduce the problem stiffness via a modification of the pressure gradient term in equation (1.3):

$$\frac{\partial}{\partial t}(\rho u_i) + \frac{\partial}{\partial x_j}(\rho u_i u_j) = -\frac{1}{\alpha^2}\frac{\partial p}{\partial x_i} + \frac{\partial \tau_{ij}}{\partial x_j} + \rho g_i, \tag{2.3}$$

where α is an arbitrary coefficient taken greater than 1.

This modification of the momentum equation leads to a corresponding modification of the balance equation for kinetic energy and although the equation for internal energy is unmodified in PGS, the equation for total energy E must also include an extra term:

$$\frac{\partial}{\partial t}(\rho E)+\frac{\partial}{\partial x_j}(\rho E u_j)=-\frac{\partial}{\partial x_j}(p u_j)+\frac{\partial}{\partial x_j}(\tau_{ij}u_i)-\frac{\partial q_j}{\partial x_j}+\rho g_j u_j+\left(1-\frac{1}{\alpha^2}\right)u_j\frac{\partial p}{\partial x_j}\,. \quad (2.4)$$

The effect of these modifications may be simply illustrated by considering a one-dimensional test problem TP1 corresponding to wave propagation in an inviscid, non-reacting, ideal gas, in the absence of gravity. The PGS system of equations for total mass, x_1-momentum and energy may be written as:

$$\left.\begin{aligned}
&\frac{\partial \rho}{\partial t}+\frac{\partial}{\partial x_1}(\rho u_1)=0,\\
&\frac{\partial u_1}{\partial t}+u_1\frac{\partial u_1}{\partial x_1}+\frac{1}{\rho\alpha^2}\frac{\partial p}{\partial x_1}=0,\\
&\frac{\partial p}{\partial t}+u_1\frac{\partial p}{\partial x_1}+\gamma p\frac{\partial u_1}{\partial x_1}=0,
\end{aligned}\right\} \quad (2.5)$$

where γ is the ratio of specific heats of the gaseous mixture; and where the energy equation has been cast as an equation for pressure. (In Appendix A, we present several alternative forms of energy equation.) This system of three scalar equations may be conveniently re-written as a matrix equation:

$$\frac{\partial \mathbf{U}}{\partial t}+\mathbf{A}_{x_1}\cdot\frac{\partial \mathbf{U}}{\partial x_1}=\mathbf{0}\,,$$

where $\mathbf{U}$ is the vector of unknowns, $\mathbf{U}=(\rho,u_1,p)^T$, and $\mathbf{A}_{x_1}$ is a (3×3) matrix whose coefficients are readily obtained from the system (2.5) above. This matrix formulation facilitates a wave analysis since for instance, the eigenvalues of $\mathbf{A}_{x_1}$ may be directly

interpreted as the propagation speeds of the different waves embedded in equations (2.5). One finds that perturbations may propagate at convective speed u_1 or acoustic speeds ($u_1 \pm c$), where c is the PGS-modified speed of sound:

$$c = \frac{1}{\alpha}\sqrt{\frac{\gamma p}{\rho}} = \frac{1}{\alpha}\sqrt{\frac{\gamma RT}{M}}\,. \tag{2.6}$$

This result shows that the effect of the PGS scaling in equations (2.3) and (2.4) is to reduce the speed of sound waves by a factor α. This reduction in the stiffness allows in turn for a faster time integration of the governing equations: as seen in equations (2.1) and (2.2), time increments may be increased by a factor of order α. Reference [53] argues that in problems with nearly homogeneous pressure, the PGS modifications will have little impact on the accuracy of the flow solution as long as the artificially increased flow Mach numbers Ma remain in the incompressible range ($Ma < 0.3$).

The difficulties that arise in problems with non-homogeneous pressure are now examined in more detail. As discussed in [53], in addition to a modification of the speed of sound c, PGS also produces an amplification of pressure variations by a factor α^2. This effect may be illustrated by considering a second one-dimensional test problem TP2 corresponding to steady flow in an inviscid, non-reacting, ideal gas, in the presence of gravity. The PGS system of equations for total mass, x_1-momentum and energy may be written as:

$$\left.\begin{aligned} &\frac{\partial}{\partial x_1}(\rho u_1) = 0, \\ &u_1 \frac{\partial u_1}{\partial x_1} + \frac{1}{\rho \alpha^2} \frac{\partial p}{\partial x_1} = g_1, \\ &u_1 \frac{\partial p}{\partial x_1} + \gamma p \frac{\partial u_1}{\partial x_1} = 0. \end{aligned}\right\} \tag{2.7}$$

Combining the last two equations of (2.7), one finds the following expression for the pressure gradient:

$$\frac{\partial p}{\partial x_1} = \rho g_1 \alpha^2 \left(1 - Ma^2\right),$$

where *Ma* is a modified Mach number based on the speed of sound in equation (2.6). Assuming a low Mach number flow, this result shows that the effect of PGS in problem TP2 is to amplify the pressure gradient by a factor α^2. It is worth emphasizing that a simple re-scaling of the gravity acceleration vector will not fix this problem since a re-scaling of g_1 would correspond to an unacceptable change in the flow Froude number, *i.e.* a change in the balance between inertial and gravitational forces.

Thus, the domain of validity of PGS is restricted to problems where the corresponding amplification of pressure variations remains acceptable. Problems where the flow dynamics are controlled by external pressure gradients, for instance ducted flow problems, are *a priori* outside the reach of a PGS treatment. We now propose a variation of the PGS method, called the Acoustic Speed Reduction (ASR) method, that achieves a decrease in speed of acoustic waves similar to PGS while preserving the pressure gradient.

The Acoustic Speed Reduction (ASR) Method

In ASR, the momentum equation is unchanged while the energy equation is modified with the addition of an extra term. The exact form of this extra term is first postulated as a starting point and then justified based on both a detailed analysis of problems TP1 and TP2 and further insights on how to extrapolate the ASR treatment to flame problems. A more rigorous mathematical derivation of ASR based on asymptotic expansions of the governing equations (valid for weakly compressible flows) is presented in Appendix B.

The ASR-modified equation for total energy takes the form:

$$\frac{\partial}{\partial t}(\rho E)+\frac{\partial}{\partial x_j}(\rho E u_j)=-\frac{\partial}{\partial x_j}(p u_j)+\frac{\partial}{\partial x_j}(\tau_{ij}u_i)-\frac{\partial q_j}{\partial x_j}+\rho g_j u_j+\left(1-\frac{1}{\alpha^2}\right)\frac{\gamma p}{\gamma-1}\left\{\frac{\partial u_j}{\partial x_j}\right\}_{ac}, \tag{2.8}$$

where α is an arbitrary coefficient taken greater than 1; and where $\{\partial u_j/\partial x_j\}_{ac}$ designates the acoustic component of flow dilatation (see below).

In order to compare ASR to PGS, let us consider again the simplified problems TP1 and TP2 introduced above. We consider for now that the acoustic component of flow dilatation is simply equal to the total flow dilatation, $\{\partial u_j/\partial x_j\}_{ac}=\{\partial u_j/\partial x_j\}$. The ASR system of equations for TP1 may be written as:

$$\left.\begin{aligned}&\frac{\partial \rho}{\partial t}+\frac{\partial}{\partial x_1}(\rho u_1)=0,\\&\frac{\partial u_1}{\partial t}+u_1\frac{\partial u_1}{\partial x_1}+\frac{1}{\rho}\frac{\partial p}{\partial x_1}=0,\\&\frac{\partial p}{\partial t}+u_1\frac{\partial p}{\partial x_1}+\frac{\gamma p}{\alpha^2}\frac{\partial u_1}{\partial x_1}=0,\end{aligned}\right\} \tag{2.9}$$

where the energy equation has been cast as an equation for pressure. An eigenmode analysis shows that the eigenvalues of the ASR system (2.9) are identical to that of the PGS system (2.5), and that the expression for the ASR-modified speed of sound is that given in equation (2.6). Thus, ASR shares with PGS the ability to reduce the speed of sound waves by an arbitrary factor α.

We now consider problem TP2. The corresponding ASR system of equations may be written as:

$$\left.\begin{aligned} &\frac{\partial}{\partial x_1}(\rho u_1) = 0, \\ &u_1 \frac{\partial u_1}{\partial x_1} + \frac{1}{\rho}\frac{\partial p}{\partial x_1} = g_1, \\ &u_1 \frac{\partial p}{\partial x_1} + \frac{\gamma p}{\alpha^2}\frac{\partial u_1}{\partial x_1} = 0. \end{aligned}\right\} \tag{2.10}$$

Combining the last two equations of (2.10), we get the new ASR expression for the pressure gradient:

$$\frac{\partial p}{\partial x_1} = \rho g_1 \left(1 - Ma^2\right),$$

where *Ma* is a modified Mach number based on the speed of sound in equation (2.6). Assuming a low Mach number flow, this result is independent of α and is a good approximation to the exact solution. TP2 shows that contrary to PGS, ASR does not amplify pressure gradients.

We now turn to the problem of providing a final expression for $\left\{\partial u_j / \partial x_j\right\}_{ac}$. Like in PGS, the basic idea in ASR is to manipulate terms in the governing equations that are small (of order Ma^2) and do not contribute much to the slow flow dynamics.

The manipulation achieves an artificial decrease in acoustic speeds without changing the order 1 physics. This argument suggests that the extra term introduced in equation (2.8) cannot be taken as proportional to the total flow dilatation: flow dilatation is not small in a combustion problem. To resolve this difficulty, we consider a general expression for flow dilatation:

$$\frac{\partial u_j}{\partial x_j} = -\frac{1}{\gamma p}\left[\frac{\partial p}{\partial t} + u_j \frac{\partial p}{\partial x_j}\right] + \frac{\gamma - 1}{\gamma p}\left[\tau_{ij}\frac{\partial u_i}{\partial x_j} - \frac{\partial q_j}{\partial x_j} - \sum_{k=1}^{N_S}\left(h_k - \frac{Mc_pT}{M_k}\right)\left(-\frac{\partial}{\partial x_j}(\rho Y_k V_{k,j}) + \dot{\omega}_k\right)\right],$$

where c_p is the specific heat of the gaseous mixture at constant pressure. In the absence of an external pressure gradient, the first term on the right-hand-side of this expression corresponds to the acoustic contribution to the dilatational field and is of order Ma^2; the second term corresponds to the contribution associated with viscous dissipation, heat conduction and heat release and is of order 1. This suggests the following decomposition of flow dilatation:

$$\left.\begin{aligned}
&\frac{\partial u_j}{\partial x_j} = \left\{\frac{\partial u_j}{\partial x_j}\right\}_{ac} + \left\{\frac{\partial u_j}{\partial x_j}\right\}_{th}, \\
&\left\{\frac{\partial u_j}{\partial x_j}\right\}_{ac} = -\frac{1}{\gamma p}\left[\frac{\partial p}{\partial t} + u_j \frac{\partial p}{\partial x_j}\right], \\
&\left\{\frac{\partial u_j}{\partial x_j}\right\}_{th} = \frac{\gamma - 1}{\gamma p}\left[\tau_{ij}\frac{\partial u_i}{\partial x_j} - \frac{\partial q_j}{\partial x_j} - \sum_{k=1}^{N_S}\left(h_k - \frac{Mc_pT}{M_k}\right)\left(-\frac{\partial}{\partial x_j}(\rho Y_k V_{k,j}) + \dot{\omega}_k\right)\right],
\end{aligned}\right\} \qquad (2.11)$$

where $\{\partial u_j / \partial x_j\}_{ac}$ and $\{\partial u_j / \partial x_j\}_{th}$ designate the acoustic and heat transfer components of flow dilatation. Note that this decomposition is not unique since viscous dissipation is of order Ma^2 and could have been incorporated into the acoustic component. In addition, in the presence of an external pressure gradient, the decomposition may have to be reformulated to properly account for non-acoustic

pressure variations. These variations, however, are typically small and numerical tests indicate that alternatives to the expressions proposed in equation (2.11) do not lead to significant changes in the results.

The ASR pressure-dilatation term in equation (2.8) is based on the acoustic contribution to flow dilatation, and this contribution may be evaluated as the difference between total dilatation and its heat transfer component. The final ASR formulation may now be written as follows:

$$\frac{\partial}{\partial t}(\rho E)+\frac{\partial}{\partial x_j}(\rho E u_j)=-\frac{\partial}{\partial x_j}(p u_j)+\frac{\partial}{\partial x_j}(\tau_{ij}u_i)-\frac{\partial q_j}{\partial x_j}+\rho g_j u_j$$
$$+\left(1-\frac{1}{\alpha^2}\right)\frac{\gamma p}{\gamma-1}\frac{\partial u_j}{\partial x_j}$$
$$-\left(1-\frac{1}{\alpha^2}\right)\left[\tau_{ij}\frac{\partial u_i}{\partial x_j}-\frac{\partial q_j}{\partial x_j}-\sum_{k=1}^{N_S}\left(h_k-\frac{Mc_pT}{M_k}\right)\left(-\frac{\partial}{\partial x_j}(\rho Y_k V_{k,j})+\dot{\omega}_k\right)\right]. \tag{2.12}$$

The PGS and ASR modifications described in equations (2.3)-(2.4) and (2.12) above have been implemented into S3D. The software changes are limited and straightforward: they include both a modification of the basic expressions for variations in momentum and energy applied to the interior of the computational domain as well as corresponding adaptations of the characteristic-based boundary condition treatment [40, 41] (the modifications to the boundary scheme are straightforward and are limited to the handling of the modified momentum or energy equations and the corresponding decrease in acoustic speeds). The next section will present numerical results obtained with S3D in a number of test problems, including non-reacting flow problems and laminar flame problems where chemical reaction is treated with single-step or detailed kinetics.

2.3. Results

Non-Reacting Flow Tests

We first consider the one-dimensional test problem TP1 discussed in section 2.2 above. Figure 2-1 presents the simulation of an acoustic wave propagating in quiescent air. The numerical configuration corresponds to a uniform computational mesh, $\Delta x = 100\ \mu$m, while time integration is performed at a pace determined by the acoustic-based CFL stability condition, $\Delta t \approx 0.288\ \mu$s ($\Delta t$ is readily obtained from equation (2.1) using $CFL = 1$ and $c \approx 348$ m/s). The initial profiles for mass density, flow velocity and energy are specified according to linear acoustics theory (see for instance [54]) and with the intent to generate a single right-traveling perturbation. The results presented in figure 2-1 provide a physical description of the propagating acoustic pulse as well as a numerical description of the performance of the right x-boundary condition as the acoustic pulse exits the computational domain. Without PGS or ASR, the propagation speed of the acoustic pulse is the unmodified speed of sound:

$$c = \sqrt{\frac{\gamma RT}{M}} \approx 348.0 \text{ m/s},$$

where $\gamma = 1.4$, $R = 8.314$ J/mol-K, $T = 300$ K, $M \approx 28.84 \times 10^{-3}$ kg/mol.

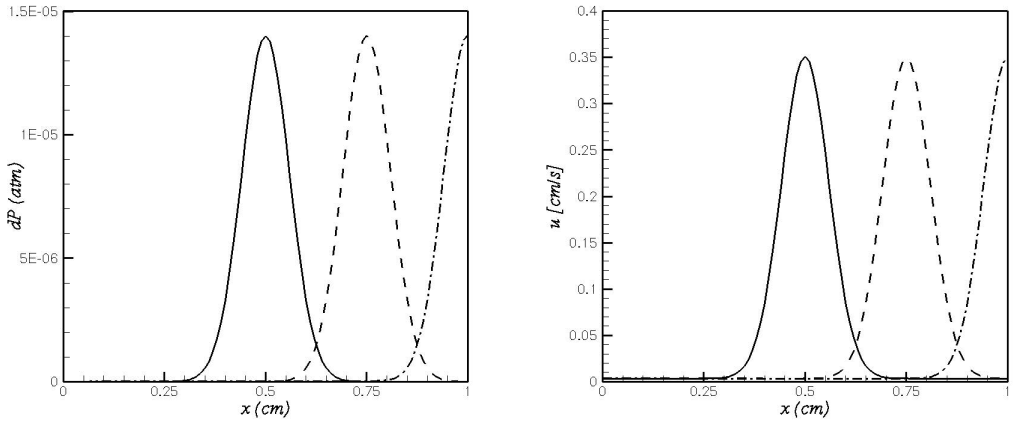

(a) (b)

Figure 2-1. Right-traveling acoustic wave without PGS or ASR. The simulation correspond to air at standard temperature and pressure conditions, T = 300 K, p = 1 atm. Figures (a) and (b) show the acoustic pressure and x-velocity perturbations versus spatial distance at 3 successive times; solid line: t = 0; dashed line: t = 7.2 μs; dash-dotted line: t = 14.4 μs. The perturbations travel across the (one-dimensional) computational domain at the speed of sound, $c \approx$ 348.0 m/s.

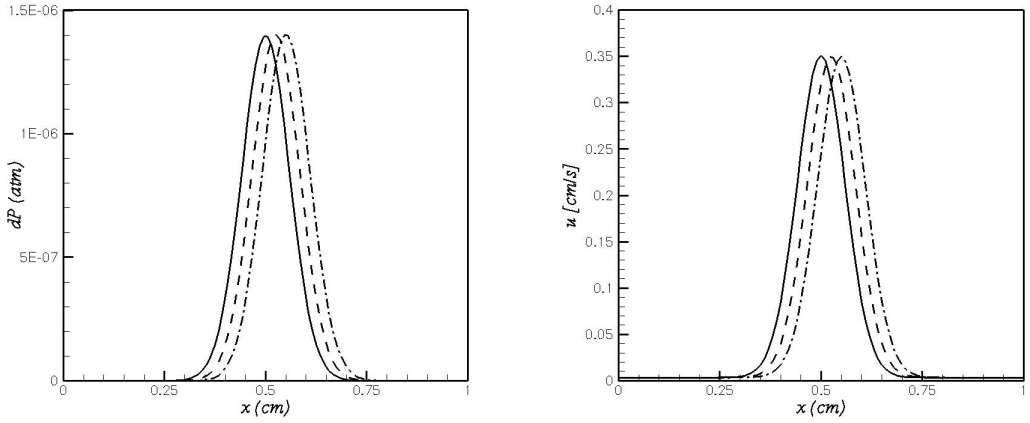

(a) (b)

Figure 2-2. Right-traveling acoustic wave with ASR (α = 10). The simulation conditions and plotting parameters are identical to those of Fig. 1. Solid line: t = 0; dashed line: t = 7.2 μs; dash-dotted line: t = 14.4 μs. The perturbations travel across the computational domain at an ASR-modified pseudo-speed of sound, $c \approx$ 34.8 m/s.

Figure 2-2 presents an ASR-modified simulation of the same isothermal sound propagation problem. The ASR free parameter α is chosen equal to 10. The acoustic evolution is unchanged compared to that obtained without ASR (while not shown

here, this statement also applies to the right x-boundary response to the incoming perturbation), with the important difference that the acoustic pulse propagation takes place at a much reduced speed. Figure 2-2 shows that consistent with equation (2.6), the propagation velocity is reduced by a factor $\alpha = 10$. Also, consistent with equation (2.1), the modified speed of sound allows in turn for a tenfold increase in the computational time step, $\Delta t \approx 2.88$ μs. Similar results were obtained with PGS. Thus, simulations of problem TP1 confirm the ability of PGS and ASR to artificially manipulate the speed of sound and allow for larger computational time steps.

We now turn to the one-dimensional test problem TP2. Figure 2-3 presents results obtained in different S3D simulations and corresponding to slow and steady flow of air evolving in a normal gravity field. The simulations differ only due to the presence or absence of a PGS or ASR treatment. The numerical configuration in figure 2-3 corresponds to a uniform computational mesh, $\Delta x = 10$ mm, and time integration is acoustic-CFL-limited; without PGS or ASR: $\Delta t \approx 28.8$ μs; with PGS or ASR and $\alpha = 10$: $\Delta t \approx 288$ μs. Figure 2-3 compares the PGS and ASR pressure variations and shows that the PGS transformation produces an amplification of the pressure variations by a factor $\alpha^2 = 100$. In contrast, the ASR transformation successfully preserves the hydrostatic pressure gradient, $dp/dx \approx -(\rho g_x) \approx -11.5$ N/m^3 $\approx -1.135\times10^{-4}$ atm/m. Thus, simulations of problem TP2 confirm the ability of ASR to correctly predict the pressure field.

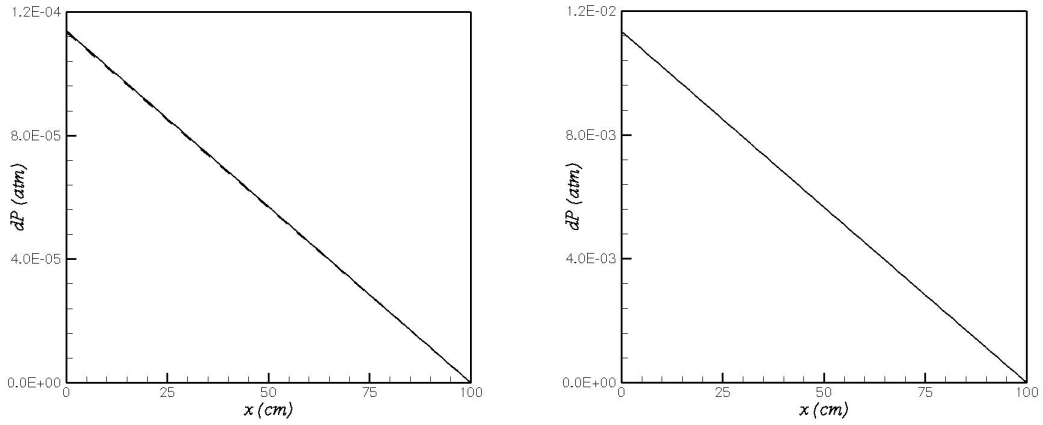

(a) (b)

Figure 2-3. Hydrostatic pressure variations versus vertical distance. The simulations correspond to air at standard temperature, pressure and gravity conditions, T = 300 K, p = 1 atm, g_x = -9.81 m/s^2 (gravity is pointing into the negative x-direction). Figure (a) presents results obtained both without PGS or ASR (solid line) and with ASR (dashed line, α = 10). Figure (b) presents results obtained with PGS (solid line, α = 10). Compared to Fig. (a), pressure variations in Fig. (b) are amplified by a factor α^2 = 100.

Next, we provide an example of a pressure-driven ducted flow configuration where the pressure-preserving capability of ASR is critical to obtaining the correct flow solution. The configuration corresponds to a two-dimensional, plane, steady, laminar flow of air evolving between two (isothermal) solid plates located H = 1 cm apart (figure 2-4). The flow is driven by a prescribed (uniform) streamwise pressure gradient, $dp/dx \approx$ -2.2 N/m^3, and corresponds to a classical one-dimensional Poiseuille flow solution with a parabolic cross-stream velocity distribution (top insert in figure 2-4) and a y-averaged velocity $\overline{u} = (H^2/12\mu)(-dp/dx) \approx 1$ m/s, where μ is the dynamic viscosity of air, $\mu \approx 1.84\times10^{-5}$ (N.s)/m^2. The numerical configuration in figure 2-4 corresponds to a uniform computational mesh, Δx = 400 μm and Δy = 100 μm; and time integration is acoustic-CFL-limited; without PGS or ASR: $\Delta t \approx$ 0.286 μs.

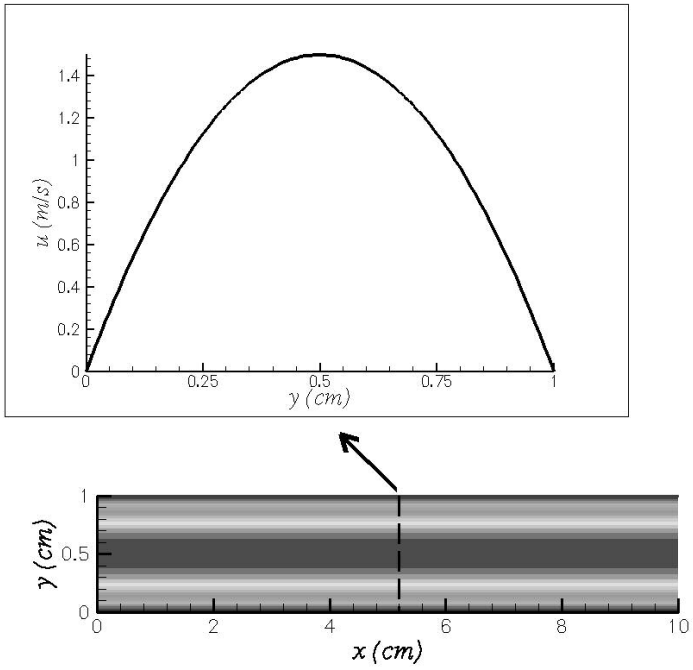

Figure 2-4. Two-dimensional laminar Poiseuille flow configuration. The simulations correspond to air at standard temperature and pressure conditions, T = 300 K, p = 1 atm, moving steadily along the x-direction between 2 solid plates (located at y = 0 and 1 cm) and driven by a prescribed pressure drop between the duct inlet (x = 0) and outlet (x = 10 cm), $\Delta p_x \approx$ -0.22 Pa. The bottom plot presents iso-contours of x-velocity and shows that the flow remains one-dimensional across the computational domain. The top insert presents a cross-stream x-velocity profile; this velocity profile features a classical parabolic shape and a y-averaged velocity $\bar{u} \approx 1\,\mathrm{m/s}$.

It is important to emphasize that in the ducted flow configuration of figure 2-4, the pressure variations are an input to the problem and the primary output of the numerical simulations is the resulting flow field. In figure 2-5, we use the mass flow rate $\dot{m}'$ going through the duct as a global measure of the solution accuracy, and $\dot{m}'$ is evaluated in different simulations performed with PGS or ASR and different values of the free parameter α. The theoretical value for the mass flow rate per unit depth is $\dot{m}' = (\rho H \bar{u}) \approx 1.18 \times 10^{-2}$ kg/(s - m); and figure 2-5 shows that this value is correctly predicted in the simulation without PGS or ASR (*i.e.* when α = 1). Figure 2-5 also shows that while the ASR transformation leaves the flow solution unchanged, the

PGS transformation leads to an incorrect solution where the mass flow rates through the duct is decreased by a factor α^2. This example demonstrates that for problems where pressure is an active part of the flow solution, the pressure-preserving capability of ASR is critical to maintaining solution accuracy.

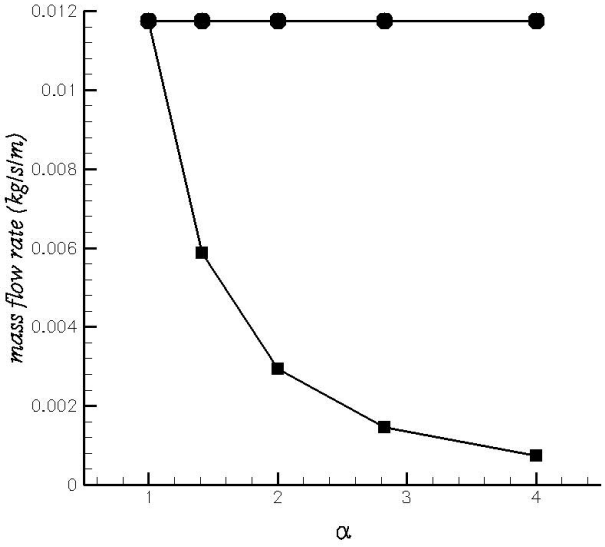

Figure 2-5. Mass flow rate per unit depth in PGS- and ASR-modified simulations of a two-dimensional laminar Poiseuille flow (see figure 2-4). Top curve (circle symbols): ASR; bottom curve (square symbols): PGS. The figure shows that while the ASR-solution is insensitive to the value of α, the PGS-solution strongly depends on it. In PGS, the pressure-driven mass flow rate through the duct is incorrectly reduced by a factor α^2.

Reacting Flow Tests

We now consider the application of ASR to chemically reacting flow problems and present below two examples of ASR-modified numerical simulations of laminar premixed flames. The first example in figure 2-6 corresponds to a two-dimensional, plane flame propagating steadily into a lean methane-air mixture at standard temperature and pressure conditions. The equivalence ratio is $\phi = 0.7$; the flame is

stabilized inside the computational domain by blowing the methane-air mixture across the left boundary ($x = 0$) at a velocity equal to the laminar flame speed, $u = s_L \approx 0.20$ m/s. At initial time, $t = 0$, the methane-air feeding stream is perturbed by the introduction of a small round-shaped fuel-enriched pocket of diameter $D \approx 0.2$ cm and centered near $(x,y) \approx (0.4 \text{ cm}, 1 \text{ cm})$. The equivalence ratio in the pocket is $\phi = 1$. Methane-air combustion is described using a single-step chemistry model proposed in [54] (p. 52) and near-unity Lewis numbers ($Le_{CH4} = 0.99$; $Le_{O2} = 1.08$). The numerical configuration in figure 2-6 corresponds to a uniform computational mesh, $\Delta x \approx 31.3$ μm and $\Delta y \approx 78.4$ μm; and time integration is acoustic-CFL-limited; without PGS or ASR: $\Delta t \approx 0.056$ μs (Δt is readily obtained from equation (2.1) using $CFL = 1.7$ and $c \approx 942$ m/s. Note that the value of the stability parameter CFL has been increased from 1 to 1.7 in order to speed up the calculations. Note also that c designates the maximum value of the speed of sound over the computational domain; the value of c is higher in combustion problems than in inert flow problems due to the higher fluid temperatures).

Figures 2-7, 2-8 and 2-9 provide a physical description of the flame response to the incoming stoichiometric pocket as well as a snapshot comparison between two simulations performed with and without ASR treatment (ASR is used with $\alpha = 10$ and $\Delta t \approx 0.56$ μs). As it passes through the flame, the stoichiometric pocket changes the local burning conditions and thereby leads to: a local increase in flame speed and the subsequent wrinkling of the flame surface (figure 2-7a); a local increase in flame temperature and the post-flame development of a hot spot (figure 2-8a); and a local increase in flow acceleration and the post-flame development of a high-velocity

region (figure 2-9a). Figures 2-7b, 2-8b, and 2-9b show that the ASR-modified simulation correctly reproduces the details that are observed in the fully compressible flame-flow structure. A more global perspective is adopted in figure 2-10 where we use the total methane mass reaction rate (space-averaged over the computational domain) as a measure of the ASR solution accuracy. The agreement between the ASR-modified and fully compressible results is again excellent. And this example shows that the ASR transformation may be successfully applied to combustion problems.

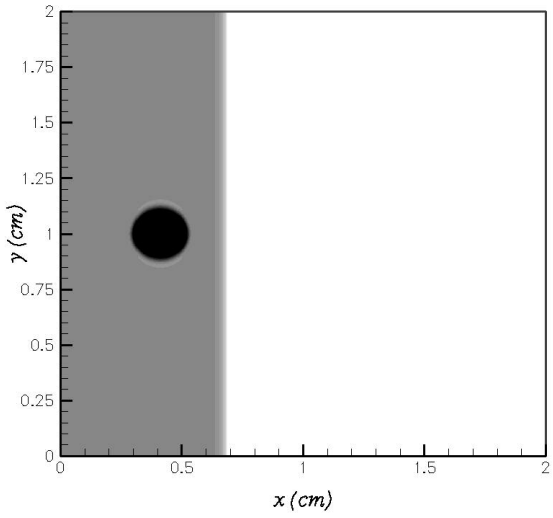

Figure 2-6. Two-dimensional laminar premixed flame configuration. The simulations correspond to an initially plane, steady, lean, methane-air flame perturbed by an incoming stoichiometric pocket. Methane-air combustion is described using single-step chemistry. The figure presents iso-contours of the initial methane mass fraction distribution: the gray region on the left (x < 0.7 cm) corresponds to lean reactants (ϕ = 0.7); the black round-shaped region near (x,y) ≈ (0.4 cm, 1 cm) corresponds to the stoichiometric perturbation (ϕ = 1); the white region on the right (x > 0.7 cm) corresponds to combustion products (Y_{CH4} = 0).

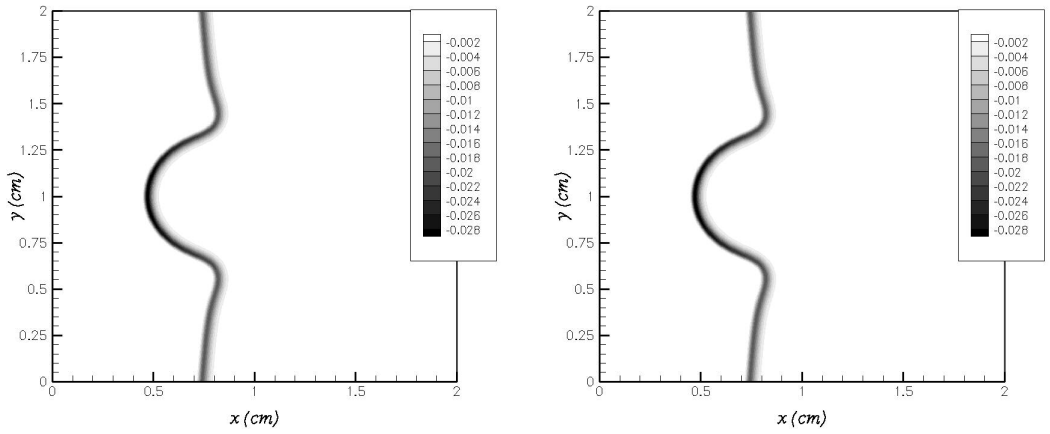

(a) (b)

Figure 2-7. Unsteady response of a lean, methane-air, laminar premixed flame to an incoming stoichiometric pocket (see figure 2-6). Iso-contours of the fuel mass reaction rate $\dot{\omega}_{CH4}$ obtained at time $t \approx 0.014$ s. $\dot{\omega}_{CH4}$ is expressed in cgs units (g/s-cm^3). Figure (a) presents results obtained without PGS or ASR; figure (b) presents results obtained with ASR ($\alpha = 10$).

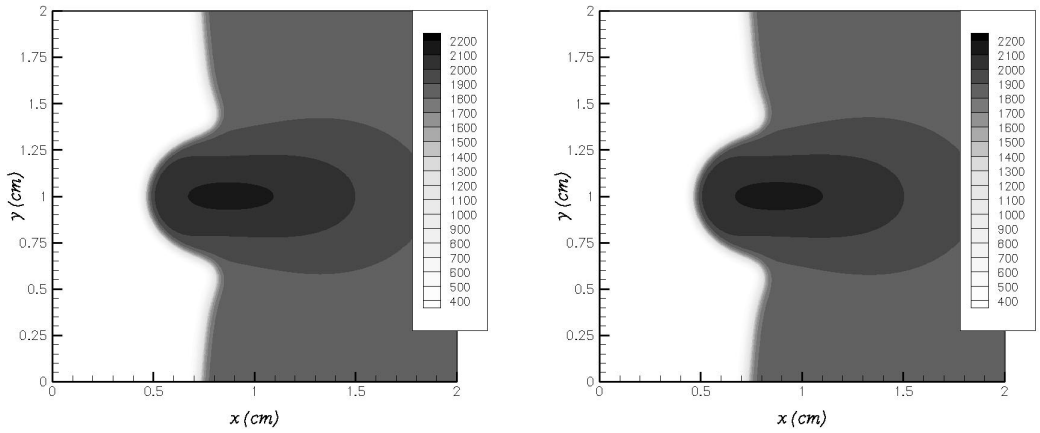

(a) (b)

Figure 2-8. Unsteady response of a lean, methane-air, laminar premixed flame to an incoming stoichiometric pocket (see figure 2-6). Iso-contours of the fluid temperature T obtained at time $t \approx 0.014$ s. T is expressed in Kelvin units (K). Figure (a) presents results obtained without PGS or ASR; figure (b) presents results obtained with ASR ($\alpha = 10$).

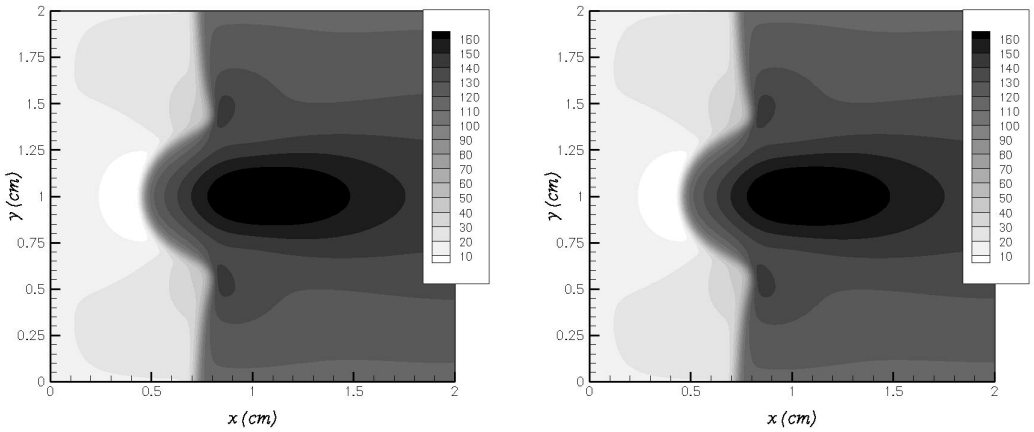

(a) (b)

Figure 2-9. Unsteady response of a lean, methane-air, laminar premixed flame to an incoming stoichiometric pocket (see figure 2-6). Iso-contours of the *x*-velocity component *u* obtained at time $t \approx 0.014$ s. *u* is expressed in cgs units (cm/s). Figure (a) presents results obtained without PGS or ASR; figure (b) presents results obtained with ASR ($\alpha = 10$).

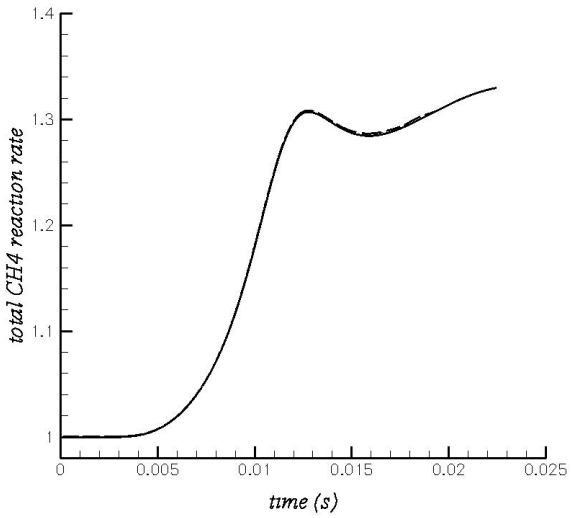

Figure 2-10. Unsteady response of a lean, methane-air, laminar premixed flame to an incoming stoichiometric pocket (see figure 2-6). The plot shows the time history of the total fuel mass reaction rate ($\dot{\omega}_{CH4}$ is space-averaged over the computational domain); solid line: without PGS or ASR; dashed line: with ASR ($\alpha = 10$). The total reaction rate is normalized by its initial value.

We now turn to a second laminar premixed flame problem where chemical reaction is treated with detailed chemical kinetics. The configuration corresponds to a one-dimensional, plane flame propagating steadily into a lean hydrogen-air mixture at

standard temperature and pressure conditions. The equivalence ratio is $\phi = 0.4$; and the flame is stabilized inside the computational domain by blowing the hydrogen-air mixture across the left boundary ($x = 0$) at a velocity equal to the laminar flame speed, $u = s_L \approx 0.21$ m/s. Hydrogen-air combustion is described using a detailed chemistry model proposed in [55] (the chemical scheme uses 9 species and 19 reversible reactions); mass diffusion is described using constant Lewis numbers ($Le_{H2} = 0.32$; $Le_H = 0.19$; all other Lewis numbers are close to unity). The numerical configuration corresponds to a uniform computational mesh, $\Delta x \approx 13.3$ μm; and time integration is acoustic-CFL-limited; without PGS or ASR: $\Delta t \approx 0.04$ μs (Δt is readily obtained from equation (2.1) using $CFL = 2.26$ and $c \approx 751$ m/s, where the value of the stability parameter CFL has been increased to its maximum theoretical value [39]).

Figures 2-11 and 2-12 present a detailed comparison between two simulations performed with and without ASR treatment (ASR is used with $\alpha = 4$ and $\Delta t \approx 0.16$ μs). Note that the exact flame location in those simulations is arbitrary and in the plots, the ASR data have been shifted to the right to facilitate the comparison with the fully compressible results. The agreement between the two solutions is found to be excellent. This statement applies both to the major flow and mixture variables (see the temperature variations displayed in figure 2-11a) as well as to the details of the chemical structure of the flame (see the variations of the hydroxyl radical reaction rate $\dot{\omega}_{OH}$ as displayed in figure 2-11b). For instance, differences in the burnt gas temperature distribution between the fully compressible and ASR solutions are quantified to be less than 0.5 % (figure 2-11a). Similarly, differences in the spatial

variations of $\dot{\omega}_{OH}$ are less than 4 % (figure 2-11b). Figure 2-12 presents another sensitive diagnostic and describes the pressure variations within the flame, from reactants to products. While slight differences in the shape of the two profiles are clearly visible (these differences may indicate that the solutions are still influenced by transients and not perfectly converged), it is also seen that the magnitude of the weak pressure drop across the flame is correctly predicted in the ASR-modified simulation, $\Delta p = \tau \times \left(\rho s_L^2\right) \approx 0.16$ Pa $\approx 1.6\times10^{-6}$ atm, where τ is the flame heat release factor and is a function of both the temperature increase across the flame ΔT and the unburnt gas temperature T_u, $\tau = \Delta T/T_u \approx 3.7$. Note that a PGS treatment would amplify the pressure drop Δp by a factor α^2.

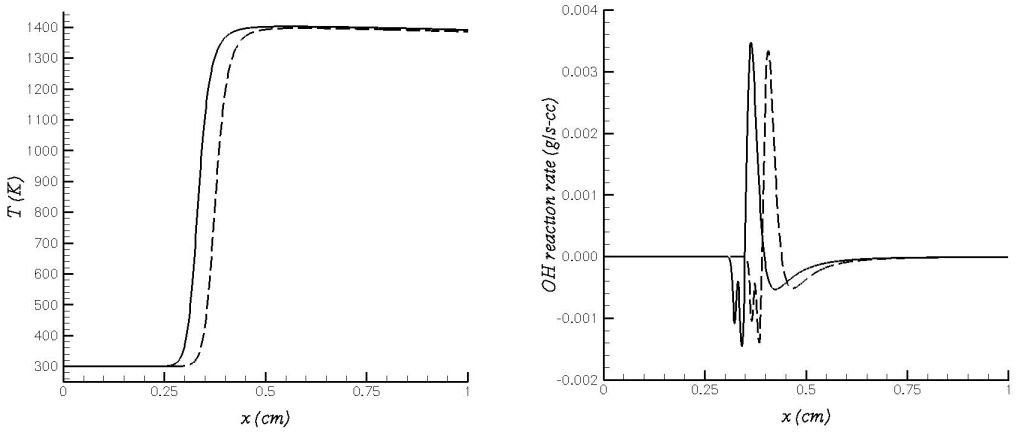

(a) (b)

Figure 2-11. One-dimensional laminar premixed flame configuration. The simulations correspond to a plane, steady, lean ($\phi = 0.4$), hydrogen-air flame. Hydrogen-air combustion is described using detailed chemical kinetics. solid line: without PGS or ASR; dashed line: with ASR ($\alpha = 4$). The ASR curve has been arbitrarily shifted to the right to facilitate the comparison with the fully compressible curve. (a) The figure presents the temperature variations across the flame; (b) spatial variations of the OH mass reaction rate $\dot{\omega}_{OH}$ across the flame. $\dot{\omega}_{OH}$ is expressed in cgs units (g/s-cm^3).

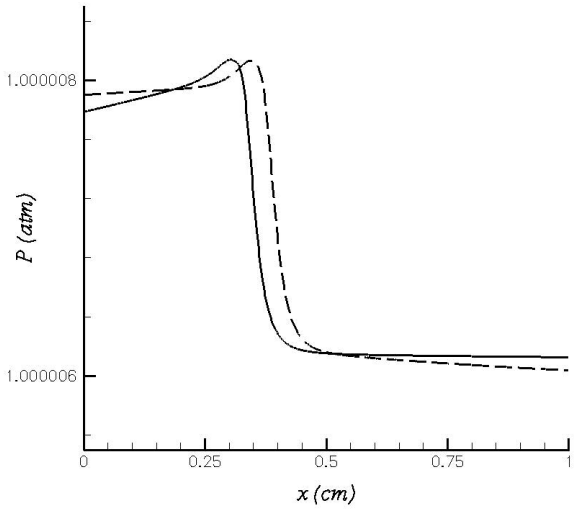

Figure 2-12. Structure of a lean, hydrogen-air, laminar premixed flame (see figure 2-11). The figure presents the pressure variations across the flame; solid line: without PGS or ASR; dashed line: with ASR ($\alpha = 4$). The ASR curve has been arbitrarily shifted to the right to facilitate the comparison with the fully compressible curve.

While this last example indicates that the ASR transformation may be successfully applied to flame problems with detailed chemical kinetics, it is also important to recognize that the gain in computational efficiency allowed by pseudo-compressibility methods may be limited in those problems. The reason for this is that detailed flame modeling features many fast evolving dynamical processes including fast chemical reactions and fast mass diffusion of light radical species. Therefore, in a fully explicit time integration approach like that used in S3D, the time step Δt is as much constrained by chemistry and diffusion as it is constrained by acoustics. In this situation, the removal of the acoustic limitation does not necessarily allow for larger values of Δt. For instance, in the previous lean hydrogen-air flame example, the time step was increased with ASR by a factor $\alpha = 4$, but could not be increased further when using larger values of α. The ASR-based control of Δt was even more limited as richer flames were considered. In the case of a stoichiometric hydrogen-air flame,

the time step was found to be controlled by fast mass diffusion of hydrogen atoms and the ASR modifications remained without significant impact on computational efficiency.

2.4. Conclusion

A pseudo-compressibility method, called the Acoustic Speed Reduction (ASR) method, has been developed to allow for more efficient computations of slow flow problems using an explicit compressible flow solver. The method is similar to the pressure gradient scaling (PGS) method proposed in [53] to the extent that it manipulates terms in the governing equations of order Ma^2, where Ma is a characteristic flow Mach number. ASR is different from PGS in that it achieves a decrease in speed of acoustic waves while preserving the pressure field, and the method can therefore be applied to problems with external pressure gradients.

The original and modified PGS methods have been implemented into a parallel direct numerical simulation (DNS) solver developed for applications to turbulent reacting flows with detailed chemical kinetics. The performance of both pseudo-compressibility methods was studied in a series of benchmark problems. While the benchmark configurations were intentionally kept simple (one- or two-dimensional space domains, laminar flows), they nevertheless included many of the important dynamical features found in combustion problems: sound propagation, gravity, pressure-driven flow, premixed flame propagation. In all tested cases, the ASR method proved successful at improving the computational efficiency while maintaining solution accuracy. For DNS applications, the gain in computational efficiency is large (typically at least an order of magnitude) in non-reacting flow

problems and reacting flow problems with single-step chemistry. The gain may be more limited, however, in reacting flow problems using detailed chemistry. For instance, in a fully explicit time integration approach, the computational time step is often as much constrained by chemistry and diffusion as it is constrained by acoustics, and the ASR-based efficiency gain is in that case moderate to low.

Finally, it is worth mentioning that while the focus of the present discussion is with DNS, the ASR method can also be easily adapted to the large eddy simulation (LES) approach.

Chapter 3: Improved Characteristic Boundary Conditions

3.1. Introduction

The objective of this boundary condition study is to adapt our DNS code S3D to simulate turbulent counterflow flames. The counterflow configuration has served as a canonical geometry to study fundamental characteristics of steady and unsteady laminar flame problems [56, 57]. The one-dimensional flame structure provides a suitable framework for detailed analysis of flame structures, ignition/extinction phenomena, and pollutant formation characteristics. The one-dimensional numerical models can easily incorporate detailed chemistry and molecular transport model [58], thereby allowing comprehensive validation of reaction mechanisms against experimental measurements. A notable recent development is the application of the counterflow systems to the study of turbulent flame problems, both in premixed and non-premixed configurations [59-61]. Like the laminar counterpart, turbulent counterflow flames provide an attractive alternative for the statistical analysis of key variables relevant to turbulent combustion modeling. Despite the simplicity in the experimental setup, however, high-fidelity DNS of turbulent counterflow flames is not a trivial task. The difficulties stems not only from the sheer computational cost required to resolve a range of physical scales, but also from other numerical aspects such as stability and boundary condition treatment.

We consider herein a DNS framework based on high-order numerical methods and a compressible flow formulation. High-order methods allow minimal numerical dissipation and thus high levels of accuracy, but they can also exhibit significant sensitivity to the boundary condition treatment. In the compressible flow formulation,

boundary conditions are handled using suitable extensions of a classical gas dynamics characteristic wave analysis. The objective of the boundary condition scheme is then to specify desired physical constraints (such as prescribed inflow velocities, pressure, or other scalar variables), while suppressing spurious acoustic wave reflections at open boundaries. These two objectives are often mutually exclusive, so that a proper balance between the two has been found to be problem-dependent. In particular, the counterflow configuration has posed an additional challenge due to the presence of two opposing inflow boundaries at which the solution variables need to be specified. The objective of the present study is to overcome these difficulties and extend the domain of application of DNS to counterflow configurations.

The characteristic boundary conditions adopted in S3D was initially developed for the hyperbolic system of Euler equations [62-67]. In this framework, the flow dynamics at any given surface boundary of the computational domain is decomposed into a set of characteristic waves, which allows the identification of incoming and outgoing waves as well as a physically-based treatment of the communication between the interior and exterior of the domain. The characteristic wave decomposition has been adapted by Poinsot and Lele [40] to the Navier-Stokes equations, known as Navier-Stokes characteristic boundary conditions (NSCBC). Further recent developments of NSCBC include an adaptation to multi-component chemically reacting flows [68, 69], a modified treatment of the chemical reaction source terms at the domain boundaries[70], and a low Mach number asymptotic expansion to decouple acoustics from other flow variables for subsonic flow applications [71]. Readers are referred to the paper of Poinsot and Lele [40] for a

detailed presentation of NSCBC, and to the review paper of Colonius [72] for a more general discussion of boundary conditions for compressible flow solvers.

In NSCBC, the locally one-dimensional inviscid (LODI) assumption is implicitly used such that variations are only retained in the direction normal to the computational domain boundary. This assumption has proven relatively robust in previous DNS studies. Note, however, that most previous studies considered unidirectional mean flow (shear layers, jets or boundary layer flows). We will show in this study that a direct application of NSCBC is inadequate when multi-directionality of the flow at the boundaries becomes important, as is the case in the counterflow configuration. An improved NSCBC formulation is then proposed and applied to various test problems to demonstrate the robustness and accuracy of the proposed method.

This chapter is organized as follows. We first briefly review the NSCBC method in the next section. Different variations of NSCBC are then considered in section 3.3 and evaluated in test simulations of non-reacting/reacting laminar counterflow configurations. Based on these tests, a modified NSCBC treatment for inflow and outflow boundaries is finally selected and successfully applied to DNS simulations of turbulent counterflow flames in section 3.4.

3.2. Review of Navier-Stokes Characteristic Boundary Conditions

NSCBC is based on a one-dimensional characteristic analysis of the different waves crossing a given boundary of the computational domain. In the following, we consider a numerical boundary in the x direction. Following Poinsot and Lele [40]

and Sutherland and Kennedy [70], we write the non-conservative form of the Navier-Stokes equations as:

$$\frac{\partial}{\partial t}\begin{bmatrix} u \\ v \\ w \\ \rho \\ p \\ Y_i \end{bmatrix} + \begin{bmatrix} \left(L_5^{(x)} - L_1^{(x)}\right)/\rho c \\ L_3^{(x)} \\ L_4^{(x)} \\ L_2^{(x)} + \left(L_5^{(x)} + L_1^{(x)}\right)/c^2 \\ L_5^{(x)} + L_1^{(x)} \\ L_{5+i}^{(x)} \end{bmatrix} + \begin{bmatrix} \mathbf{v}_t \cdot \nabla_t u \\ \mathbf{v}_t \cdot \nabla_t v + (1/\rho)\partial p/\partial y \\ \mathbf{v}_t \cdot \nabla_t w + (1/\rho)\partial p/\partial z \\ \nabla_t \cdot (\rho \mathbf{v}_t) \\ \mathbf{v}_t \cdot \nabla_t p + \gamma p \nabla_t \cdot \mathbf{v}_t \\ \mathbf{v}_t \cdot \nabla_t Y_i \end{bmatrix} = \begin{bmatrix} d_u \\ d_v \\ d_w \\ d_\rho \\ d_p \\ d_{Y_i} \end{bmatrix} + \begin{bmatrix} s_u \\ s_v \\ s_w \\ s_\rho \\ s_p \\ s_{Y_i} \end{bmatrix}, \qquad (3.1)$$

where $\mathbf{v}$ is the velocity vector, $c = (\gamma RT)^{1/2}$ the speed of sound, and the subscript t represents tangential (y and z) directions. The viscous and source terms at the right hand side are given by:

$$\begin{bmatrix} d_u \\ d_v \\ d_w \\ d_\rho \\ d_p \\ d_{Y_i} \end{bmatrix} = \begin{bmatrix} (1/\rho)\nabla_j \cdot \tau_{j1} \\ (1/\rho)\nabla_j \cdot \tau_{j2} \\ (1/\rho)\nabla_j \cdot \tau_{j3} \\ 0 \\ (\gamma - 1)\left[\tau_{jk} : \nabla_j u_k - \nabla_j \cdot q_j + \sum_{i=1}^{N} \left(h_i - c_p TM/M_i\right)\nabla_j \cdot (\rho Y_i V_{ij})\right] \\ (1/\rho)\nabla_j \cdot (\rho Y_i V_{ij}) \end{bmatrix}, \qquad (3.2)$$

$$\begin{bmatrix} s_u \\ s_v \\ s_w \\ s_\rho \\ s_p \\ s_{Y_i} \end{bmatrix} = \begin{bmatrix} \sum_{i=1}^{N} Y_i f_{ix} \\ \sum_{i=1}^{N} Y_i f_{iy} \\ \sum_{i=1}^{N} Y_i f_{iz} \\ 0 \\ (\gamma - 1)\sum_{i=1}^{N} \left[-\left(h_i - c_p TM/M_i\right)M_i \dot{\omega}_i + \rho Y_i f_{ij} V_{ij}\right] \\ (1/\rho)M_i \dot{\omega}_i \end{bmatrix}, \qquad (3.3)$$

where q_j is the heat flux in direction j, N the total number of species, V_{ij} the diffusion velocity of species i in direction j, M_i the molecular weight of species i, M the mean molecular weight, h_i the specific enthalpy of species i, c_p the mixture isobaric heat capacity, f_{ij} the body force per unit mass on species i in direction j,

and $\dot{\omega}_i$ the molar reaction rate of species i per unit volume. Convective and pressure gradient terms in x-direction are written in the form of $L_k^{(x)}$ $\left(1 \le k \le 5+N\right)$, which are the wave-based quantities obtained from a characteristic analysis of the governing equations along the x-direction. These quantities give the temporal rate of change of the amplitudes of the different waves that cross the x-boundary, and are defined as follows:

$$\mathbf{L^{(x)}} = \begin{bmatrix} L_1^{(x)} \\ L_2^{(x)} \\ L_3^{(x)} \\ L_4^{(x)} \\ L_5^{(x)} \\ L_{5+i}^{(x)} \end{bmatrix} = \begin{bmatrix} \lambda_1^{(x)} \cdot \dfrac{1}{2}\left(\dfrac{\partial p}{\partial x} - \rho c \dfrac{\partial u}{\partial x}\right) \\ \lambda_2^{(x)}\left(\dfrac{\partial \rho}{\partial x} - \dfrac{1}{c^2}\dfrac{\partial p}{\partial x}\right) \\ \lambda_3^{(x)} \dfrac{\partial v}{\partial x} \\ \lambda_4^{(x)} \dfrac{\partial w}{\partial x} \\ \lambda_5^{(x)} \cdot \dfrac{1}{2}\left(\dfrac{\partial p}{\partial x} + \rho c \dfrac{\partial u}{\partial x}\right) \\ \lambda_{5+i}^{(x)} \dfrac{\partial Y_i}{\partial x} \end{bmatrix}, \tag{3.4}$$

where $\lambda_k^{(x)}$ are the characteristic velocities:

$$\lambda_1^{(x)} = u - c, \;\; \lambda_2^{(x)} = \lambda_3^{(x)} = \lambda_4^{(x)} = \lambda_{5+i}^{(x)} = u, \;\; \lambda_5^{(x)} = u + c\,. \tag{3.5}$$

By doing the above transformation based on a characteristic analysis, the problem of specifying inflow/outflow conditions is now changed to the problem of determining the wave amplitude variations $L_k^{(x)}$. For outgoing waves, these variations are computed using information from inside the computational domain and one-sided finite difference expressions. For incoming waves, however, they cannot be computed from outside the computational domain so that additional physical considerations must be made. Poinsot and Lele [40] used the local one-dimensional inviscid (LODI)

assumption in order to provide approximate expressions for the amplitude variations of incoming waves:

$$\frac{\partial}{\partial t}\begin{bmatrix} u \\ v \\ w \\ \rho \\ p \\ Y_i \end{bmatrix} + \begin{bmatrix} \left(L_5^{(x)} - L_1^{(x)}\right)/\rho c \\ L_3^{(x)} \\ L_4^{(x)} \\ L_2^{(x)} + \left(L_5^{(x)} + L_1^{(x)}\right)/c^2 \\ L_5^{(x)} + L_1^{(x)} \\ L_{5+i}^{(x)} \end{bmatrix} = \begin{bmatrix} 0 \\ 0 \\ 0 \\ 0 \\ 0 \\ 0 \end{bmatrix}. \tag{3.6}$$

For example, consider first a subsonic inflow $(0 \le u \le c)$ at the left boundary. All waves are incoming at this boundary, except for one upstream-traveling acoustic wave corresponding to $L_1^{(x)}$ $(\lambda_1^{(x)} \le 0)$. Thus, $L_1^{(x)}$ is computed according to its definition in equation (3.4) and one-sided finite difference estimates of the spatial derivatives, whereas $L_k^{(x)}$ $(2 \le k \le 5+N)$ are determined from the LODI relations. The LODI relations correspond to simplified expressions of the physical boundary conditions that are required for well-posedness [40]. For instance, if we choose to prescribe the inlet flow variables according to known upstream values of the flow velocity vector (u_0, v_0, w_0), temperature T_0, and species mass fractions $Y_{i,0}$, we may get the expressions of incoming waves by invoking vanishing derivatives with respect to time in equation (3.6):

$$\begin{cases} L_3^{(x)} = L_4^{(x)} = L_{5+i}^{(x)} = 0, \\ L_2^{(x)} = \dfrac{2(\gamma-1)}{c^2} L_1^{(x)}, \\ L_5^{(x)} = L_1^{(x)}. \end{cases} \tag{3.7}$$

This set of boundary relations is called “hard-inflow boundary conditions”, and provides a maximum control of the inlet flow variables (all variables are fixed except

for mass density and pressure), while simultaneously leading to a perfect reflection (without damping) of the upstream-traveling acoustic wave energy back into the computational domain [68].

As an alternative, the nonreflecting-inflow conditions maintain a good control of the inlet flow variables while reducing spurious wave reflections at the inflow boundaries [54]. In the nonreflecting-inflow treatment, the inlet values of the flow velocity vector, temperature and species mass fractions are imposed using a set of relaxation terms. The modified LODI relations correspond to a set of linear relaxation constraints between the inflow variables and their prescribed upstream values. A possible choice is:

$$\begin{cases} L_2^{(x)} = \beta_2 (T - T_0), \\ L_3^{(x)} = \beta_3 (v - v_0), \\ L_4^{(x)} = \beta_4 (w - w_0), \\ L_5^{(x)} = \beta_5 (u - u_0), \\ L_{5+i}^{(x)} = \beta_{5+i} (Y_i - Y_{i,0}), \end{cases} \tag{3.8}$$

where β_k are model relaxation coefficients. These coefficients allow a soft control of the boundary variables and can be conveniently tuned in order to minimize spurious perturbations. These nonreflecting-inflow boundary conditions have been used in a large-eddy simulation study of turbulent premixed combustion instability phenomena [73]. Note that, in equation (3.8), a choice of large values for the coefficients β_k corresponds to a formulation with nearly fixed values of the inlet flow velocity, temperature and species mass fractions, and provides similar results to those obtained with the hard-inflow boundary conditions. In contrast, a choice of small values for β_k corresponds to a non-reflecting formulation with good wave transmission

properties but poor control of the inlet flow variables. Yoo et al. [74] applied the analysis of Rudy and Strikwerda [66] and showed, under simplified conditions, how the choice of the coefficients β_k may be optimized *a priori* in order to provide the best trade-off between control of the leading order solution and control of the wave perturbations. This choice corresponds to moderate values of the coefficients β_k, and is parameterized by a non-dimensional relaxation coefficient η_k (see [74], appendix A).

Let us now consider a subsonic outflow $(0 \le u \le c)$ at the right boundary. All waves are outgoing at this boundary, except for one upstream-traveling acoustic wave corresponding to $L_1^{(x)}$ $(\lambda_1^{(x)} \le 0)$. Thus, in the NSCBC method, $L_1^{(x)}$ is determined from LODI relations, whereas $L_k^{(x)}$ $(2 \le k \le 5+N)$ are computed according to equation (3.4) and one-sided finite difference estimates of the spatial derivatives. The recommended LODI relation for $L_1^{(x)}$ corresponds to a simple relaxation condition for pressure [40, 66]:

$$L_1^{(x)} = \alpha_1 (p - p_\infty) = \sigma c \frac{\left(1 - Ma^2\right)}{2 l_x} (p - p_\infty), \tag{3.9}$$

where *Ma* is the maximum Mach number at the boundary, p_∞ the imposed pressure (typically the ambient pressure), and l_x the x-length of the computational domain. σ is the relaxation factor for pressure and is set to 0.25 in this study as in Poinsot and Lele [40]. This outflow condition serves to maintain pressure (albeit in a soft way) inside the computational domain around a prescribed ambient value.

In summary, the NSCBC/LODI method provides a valuable approach to formulate boundary conditions in a compressible flow framework. The approach is

based on solving balance equations at the boundaries (as opposed to prescribing directly values of the principal variables) and on using a locally one-dimensional assumption. This one-dimensional assumption works well in flows that are essentially unidirectional and quasi-parallel (shear layers, jets or boundary layer flows); however, it becomes problematic in flow geometries that are strongly multi-directional, as will be found in the next section.

3.3. Application to Laminar Counterflow

The nonreflecting inflow boundary conditions have been discussed in the context of a unidirectional flow configuration. However it is actually not so critical in unidirectional configurations; in fact, the use of hard inflow conditions, which specify the solution variables directly, can produce reasonably good results since the acoustic waves reflected at the hard inflow boundary are allowed to leave the computational domain through the downstream nonreflecting outflow boundary. A true challenge occurs in a counterflow configuration where velocity needs to be imposed at the two opposing inflow boundaries. Application of hard inflow conditions at the two boundaries results in repeated reflections of the initial acoustic waves at both boundaries, only to disappear due to viscous dissipation. In this section, we will show that a direct application of hard inflow conditions is inadequate and a solution will be sought using the nonreflecting inflow conditions.

Another important feature of counterflow configurations is that it has inherently large transverse terms so that the one-dimensional assumption used in LODI is no longer valid. We will show in the following that the NSCBC treatment of the incoming-waves $L_k^{(x)}$-variables must account for the transverse terms (the *y*- and

z-gradient terms in equation (3.1)) that characterize variations in planes parallel to the boundary surface.

The Original LODI Method

For an illustrative purpose, we consider a two-dimensional nonreacting counterflow in which the potential flow enters from the two boundaries in the x-direction and leaves the domain through both sides in the y-direction as shown in Figure 3-1. The initial field is prescribed by the hypothetical potential flow field:

$$u_p(x) = -\kappa(x - l_x/2) \text{ and } v_p(y) = \kappa(y - l_y/2), \tag{3.10}$$

where κ [1/s] is the strain rate of the flow, and l_x and l_y are respectively the x- and y-directional domain lengths. The goal is now to reproduce this steady potential flow field numerically using various characteristic boundary conditions.

We first consider applying the hard inflow conditions which specify the solution variables directly at the x-boundaries, along with the standard nonreflecting outflow conditions at the y-boundaries. The domain size for test simulations is 1.0 cm × 1.0 cm in which 100 × 100 grid points are used. The initial flow field is a potential flow with the imposed reference pressure equal to 1.0 atm and inlet velocity at x = 0 equal to 10.0 m/s ($\kappa = 2000$ s^{-1}).

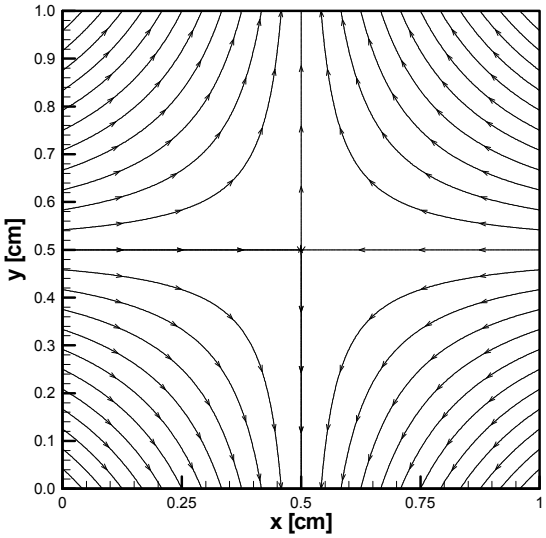

Figure 3-1. The configuration and initial condition for nonreacting counterflow tests. The solid lines represent streamlines and the arrows indicate the flow direction.

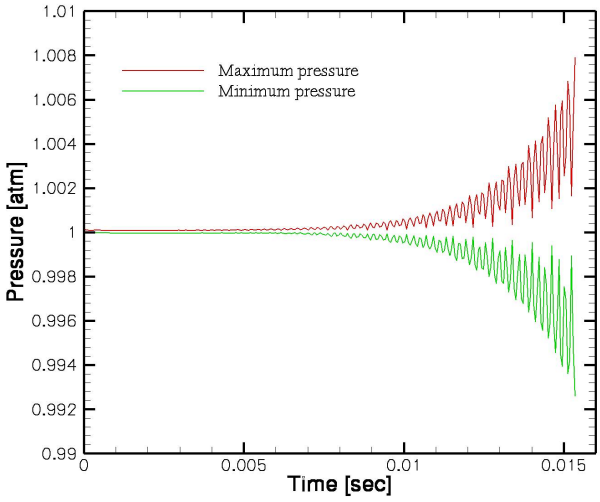

Figure 3-2. Temporal variations of the maximum and minimum pressure with the hard inflow boundary conditions.

Figure 3-2 shows the temporal variations of maximum and minimum pressure. It is clear that no steady solution can be obtained and an instability is amplified in the late phase of the simulation. The results confirm that the perfectly reflecting, hard

inflow condition imposed at two opposing boundaries is inadequate even for steady laminar counterflow.

Next, we consider applying the nonreflecting inflow conditions, as given by equation (3.8); the non-dimensional model relaxation coefficients are $\eta_k = 10$. Figure 3-3 shows the pressure and *x*-velocity isocontours for the steady solution obtained in this test case. The qualitative counterflow pattern is correctly reproduced by the numerical solution. However, there are two major flaws in the results: (a) the mean *u*-velocity at the *x*-boundaries is 8 m/s, instead of the intended value of 10 m/s; and (b) the mean background pressure increases from 1.0 atm to 1.36 atm. So, both strain rate and the thermodynamic pressure are changed in the simulation with direct application of the original LODI method.

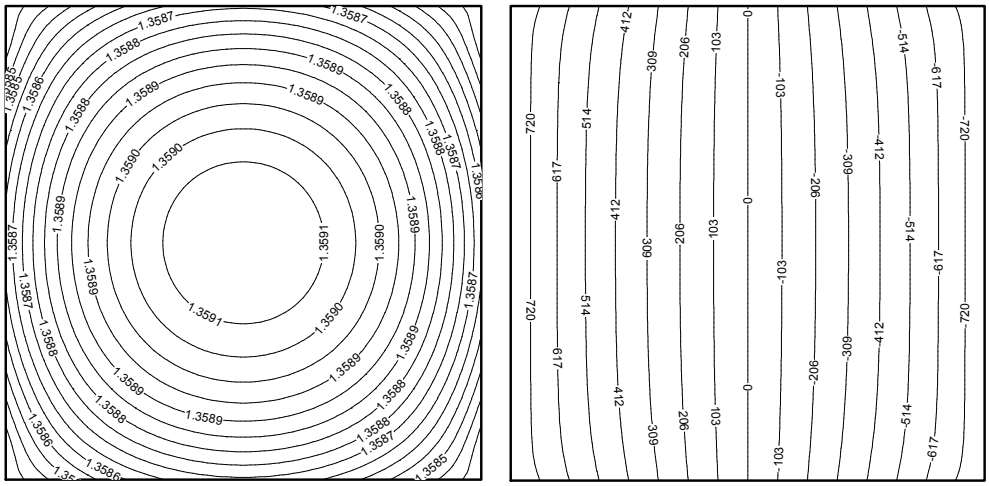

(a) Pressure [atm] (b) *x*- directional velocity

Figure 3-3. Pressure and the *x*-directional velocity fields with nonreflecting inflow conditions at t = 10 msec.

Recall that the nonreflecting boundary conditions in equation (3.8) have been successfully used in the past for unidirectional flow configurations without any drift of imposed velocity and pressure. The new feature in the present counterflow

problem is that there are strong transverse velocity gradients at the boundaries, namely $\partial v/\partial y$ at x-boundaries and $\partial u/\partial x$ at y-boundaries. These terms are believed to be responsible for the inaccuracies in the DNS solution presented in figure 3-3. In the next section, we evaluate the contribution of transverse terms and propose a modified formulation for nonreflecting inflow and outflow boundary conditions.

The LODI Method Enhanced by Multi-dimensional Effects

Recognizing that the transverse derivatives can no longer be neglected in the counterflow configuration, the LODI relations (equation (3.6)) should be modified to add transverse terms:

$$\frac{\partial}{\partial t}\begin{bmatrix} u \\ v \\ w \\ \rho \\ p \\ Y_i \end{bmatrix} + \begin{bmatrix} \left(L_5^{(x)} - L_1^{(x)}\right)/\rho c \\ L_3^{(x)} \\ L_4^{(x)} \\ L_2^{(x)} + \left(L_5^{(x)} + L_1^{(x)}\right)/c^2 \\ L_5^{(x)} + L_1^{(x)} \\ L_{5+i}^{(x)} \end{bmatrix} + \begin{bmatrix} \mathbf{v}_t \cdot \nabla_t u \\ \mathbf{v}_t \cdot \nabla_t v + (1/\rho)\partial p/\partial y \\ \mathbf{v}_t \cdot \nabla_t w + (1/\rho)\partial p/\partial z \\ \nabla_t \cdot (\rho \mathbf{v}_t) \\ \mathbf{v}_t \cdot \nabla_t p + \gamma p \nabla_t \cdot \mathbf{v}_t \\ \mathbf{v}_t \cdot \nabla_t Y_i \end{bmatrix} = \begin{bmatrix} 0 \\ 0 \\ 0 \\ 0 \\ 0 \\ 0 \end{bmatrix}. \qquad (3.11)$$

In NSCBC, it is often more convenient to define the incoming waves variations from the equations written in characteristic form [64, 70]. At the x-direction boundaries, we may rewrite equations (3.11) as follows:

$$\begin{bmatrix} \frac{1}{2}\left(\frac{\partial p}{\partial t}-\rho c\frac{\partial u}{\partial t}\right) \\ \frac{\partial \rho}{\partial t}-\frac{1}{c^2}\frac{\partial p}{\partial t} \\ \frac{\partial v}{\partial t} \\ \frac{\partial w}{\partial t} \\ \frac{1}{2}\left(\frac{\partial p}{\partial t}+\rho c\frac{\partial u}{\partial t}\right) \\ \frac{\partial Y_i}{\partial t} \end{bmatrix} + \begin{bmatrix} L_1^{(x)} \\ L_2^{(x)} \\ L_3^{(x)} \\ L_4^{(x)} \\ L_5^{(x)} \\ L_{5+i}^{(x)} \end{bmatrix} - \begin{bmatrix} \mathfrak{I}_1^{(x)} \\ \mathfrak{I}_2^{(x)} \\ \mathfrak{I}_3^{(x)} \\ \mathfrak{I}_4^{(x)} \\ \mathfrak{I}_5^{(x)} \\ \mathfrak{I}_{5+i}^{(x)} \end{bmatrix} = \begin{bmatrix} 0 \\ 0 \\ 0 \\ 0 \\ 0 \\ 0 \end{bmatrix}, \tag{3.12}$$

where $\mathfrak{I}_k^{(x)}$ designate the transverse terms in the *x*-direction characteristic equations. In a two-dimensional configuration, the transverse terms are given by:

$$\begin{cases} \mathfrak{I}_1^{(x)} = -\frac{1}{2}\left(v\frac{\partial p}{\partial y}+\gamma p\frac{\partial v}{\partial y}-\rho c v\frac{\partial u}{\partial y}\right), \\ \mathfrak{I}_2^{(x)} = -v\left(\frac{\partial \rho}{\partial y}-\frac{1}{c^2}\frac{\partial p}{\partial y}\right), \\ \mathfrak{I}_3^{(x)} = -\left(v\frac{\partial v}{\partial y}+\frac{1}{\rho}\frac{\partial p}{\partial y}\right), \\ \mathfrak{I}_5^{(x)} = -\frac{1}{2}\left(v\frac{\partial p}{\partial y}+\gamma p\frac{\partial v}{\partial y}+\rho c v\frac{\partial u}{\partial y}\right), \\ \mathfrak{I}_{5+i}^{(x)} = -v\frac{\partial Y_i}{\partial y}. \end{cases} \tag{3.13}$$

Including the transverse terms in the nonreflecting inflow conditions applied at $x = 0$, equation (3.8) becomes:

$$\begin{cases} L_2^{(x)} = \beta_2\left(T-T_0\right)+\mathfrak{I}_2^{(x)}, \\ L_3^{(x)} = \beta_3\left(v-v_0\right)+\mathfrak{I}_3^{(x)}, \\ L_5^{(x)} = \beta_5\left(u-u_0\right)+\mathfrak{I}_5^{(x)}, \\ L_{5+i}^{(x)} = \beta_{5+i}\left(Y_i-Y_{i,0}\right)+\mathfrak{I}_{5+i}^{(x)}. \end{cases} \tag{3.14}$$

Similar boundary conditions are applied at $x = l_x$, with $L_5^{(x)}$ now computed from equation (3.4) and $L_1^{(x)}$ calculated as:

$$L_1^{(x)} = \beta_1 \left(u - u_{l_x} \right) + \mathfrak{I}_1^{(x)}. \tag{3.15}$$

Similarly we also include transverse terms in the nonreflecting outflow boundary conditions at the *y*-direction:

$$\begin{cases} L_5^{(y)} = \alpha_5 \left(p - p_{\text{target}} \right) + \mathfrak{I}_5^{(y)} & \text{at} \quad y = 0, \\ L_1^{(y)} = \alpha_1 \left(p - p_{\text{target}} \right) + \mathfrak{I}_1^{(y)} & \text{at} \quad y = l_y, \end{cases} \tag{3.16}$$

where $\mathfrak{I}_5^{(y)}$ and $\mathfrak{I}_1^{(y)}$ are given by:

$$\begin{cases} \mathfrak{I}_5^{(y)} = -\dfrac{1}{2} \left(u \dfrac{\partial p}{\partial x} + \gamma p \dfrac{\partial u}{\partial x} + \rho c u \dfrac{\partial v}{\partial x} \right), \\ \mathfrak{I}_1^{(y)} = -\dfrac{1}{2} \left(u \dfrac{\partial p}{\partial x} + \gamma p \dfrac{\partial u}{\partial x} - \rho c u \dfrac{\partial v}{\partial x} \right). \end{cases} \tag{3.17}$$

Using equation (3.14), the actual equations that are effectively solved for at the inflow boundaries at $x = 0$ are:

$$\begin{cases} \dfrac{\partial \rho}{\partial t} - \dfrac{1}{c^2} \dfrac{\partial P}{\partial t} = -\beta_2 \left(T - T_0 \right), \\ \dfrac{\partial v}{\partial t} = -\beta_3 \left(v - v_0 \right), \\ \dfrac{1}{2} \left(\dfrac{\partial p}{\partial t} + \rho c \dfrac{\partial u}{\partial t} \right) = -\beta_5 \left(u - u_0 \right), \\ \dfrac{\partial Y_i}{\partial t} = -\beta_{5+i} \left(Y_i - Y_{i,0} \right). \end{cases} \tag{3.18}$$

Similarly, equation (3.16) leads to the following effective outflow boundary condition at $y = 0$:

$$\frac{1}{2} \left(\frac{\partial p}{\partial t} + \rho c \frac{\partial v}{\partial t} \right) = -\alpha_5 \left(p - p_{\text{target}} \right). \tag{3.19}$$

The reason for the inclusion of the transverse terms in the expressions for the wave amplitude variations $L_k^{(x)}$ and $L_k^{(y)}$ is now apparent from equations (3.18) and (3.19): it ensures that the solution variables at the boundaries approach the correct prescribed values. In the absence of these terms, the solution variables will drift and will not be properly controlled. To prove this statement, three test cases are compared:

- Case (a) is as shown in figure 3-3, using the conventional LODI approach without including any of the transverse terms in the L_k expressions,
- Case (b) includes the $\mathfrak{I}_k^{(x)}$ terms in the inflow conditions only,
- Case (c) includes both the $\mathfrak{I}_k^{(x)}$ and $\mathfrak{I}_k^{(y)}$ terms in the corresponding inflow and outflow conditions.

	Pressure	*x*- directional velocity
Case (a)	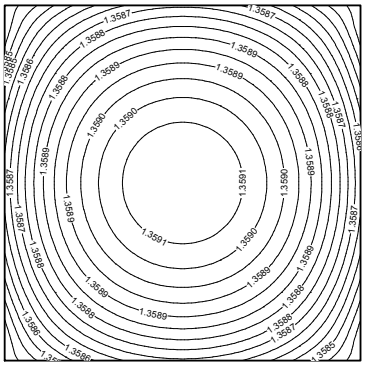	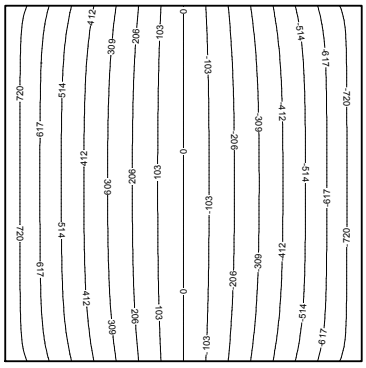

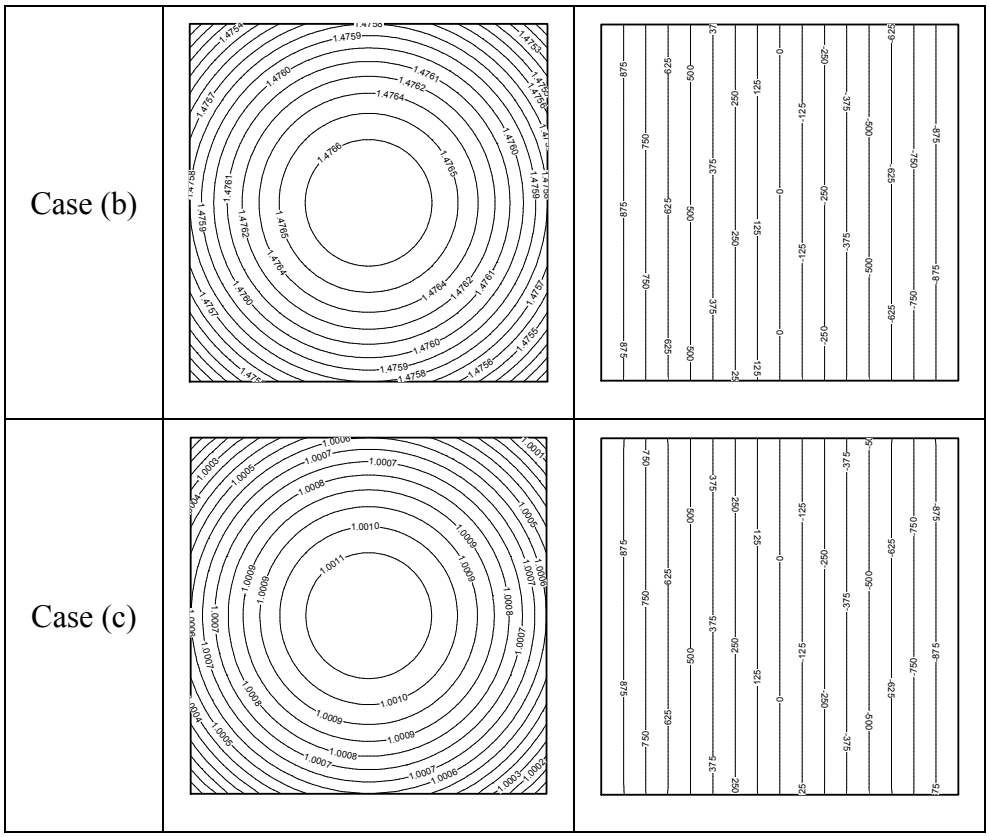

Figure 3-4. Pressure and *x*-directional velocity fields for the three test cases at t = 10 msec.

Figure 3-4 shows the pressure and *x*-directional velocity fields for the three test cases after the calculations were run for 10 msec. It is clearly seen that besides the two major flaws mentioned above, case (a) is affected by significant errors near the boundaries. Case (b) improves the velocity field, but the mean pressure field is still highly overpredicted. Only case (c) can reproduce the correct solution for both pressure and velocity.

To elaborate on these findings, figure 3-5 shows the temporal variations of the maximum pressure and the mean inlet velocity for the three test cases. For case (a), it is seen that the maximum pressure increases above the prescribed atmospheric value while the mean inlet velocity decreases from the prescribed 10 m/s to 8 m/s. The

reason may be explained as follows: if the conventional LODI method is used, the following equation is effectively solved at the left inflow boundary:

$$\frac{1}{2}\left(\frac{\partial p}{\partial t}+\rho c\frac{\partial u}{\partial t}\right)=-\beta_5\left(u-u_0\right)+\Im_5^{(x)} \quad \text{at } x=0. \tag{3.20}$$

where the $\Im_5^{(x)}$ term is large in the presence of a strong straining motion. A similar expression can be derived for the right inflow boundary at $x=l_x$. Therefore, at steady state, the boundary velocity takes an incorrect value equal to $u=u_0+\Im_5^{(x)}/\beta_5$. Case (b) corrects this problem of a velocity drift by effectively eliminating $\Im_5^{(x)}$ in equation (3.20). It does not address, however, the separate problem of a pressure drift. The reason for the pressure drift could be explained using similar arguments: in the conventional LODI method, the following equation is effectively solved at the bottom outflow boundary:

$$\frac{1}{2}\left(\frac{\partial p}{\partial t}+\rho c\frac{\partial v}{\partial t}\right)=-\alpha_5\left(p-p_{\text{target}}\right)+\Im_5^{(y)} \quad \text{at } y=0. \tag{3.21}$$

Therefore, at steady state, the boundary pressure takes an incorrect value equal to $p=p_{\text{target}}+\Im_5^{(y)}/\alpha_5$. Case (c) corrects this problem of a pressure drift by effectively eliminating $\Im_5^{(y)}$ in equation (3.21).

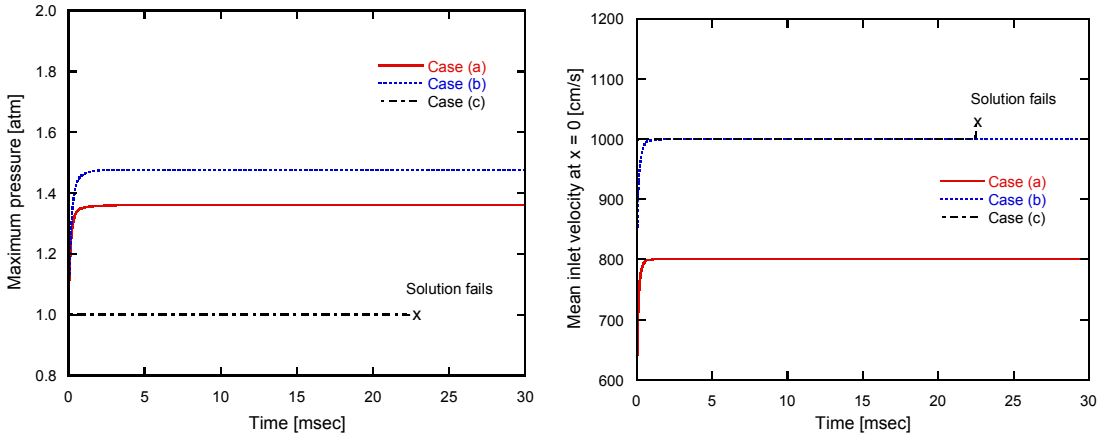

(a) Maximum pressure (b) Mean inlet velocity at $x = 0$

Figure 3-5. Temporal variations of the maximum pressure and the mean inlet velocity at $x = 0$ for Cases (a)–(c).

These results confirm that in counterflow configurations, a proper accounting of the transverse gradient terms in the expressions for the wave amplitude variations $L_k^{(x)}$ and $L_k^{(y)}$ at both inflow and outflow boundaries is critical in achieving the correct solution. One remaining problem with case (c), however, is that the solution suffers from a numerical instability and is observed to fail after a long calculation time (see figure 3-5). This problem is addressed in the next section.

A Modified Nonreflecting Outflow Boundary Condition

We now consider the numerical instability encountered in case (c). A comparison between cases (b) and (c) suggests that the instability arises from the outflow rather than the inflow boundaries. In other words, including transverse terms in the formulation of incoming waves at the outflow boundary can prevent the deviation of background pressure, however, simply doing this causes instability. Actually this

outflow boundary condition (equation (3.19)) has been discussed in the literature. Giles [67] showed, from the linearized Euler equations, that equation (3.19) would produce reflections for waves with a non-normal angle of incidence to the boundary. This boundary condition corresponds to the first order approximation to the ideal non-reflecting boundary conditions for multidimensional flows. Higher order approximations require some transverse terms. Nicoud [75] also suggested, from numerical tests, that some forms of transverse terms are necessary in multi-dimensional problems in order to reach the correct steady state solution.

It is very difficult, if not impossible, to propose general non-reflecting boundary conditions for multidimensional non-linear systems with a rigorous mathematical derivation. Nevertheless, to empirically solve the above-mentioned instability problem, we understand that we must retain some transverse terms in the final effective equations solved at the boundary, and in the mean time, make them small to avoid the drift of the background pressure. Thus, the outflow boundary condition is modified to accommodate both pressure and transverse term relaxation effects simultaneously by introducing a transverse damping parameter a $(0 \le a \le 1)$ and a reference value $\mathfrak{I}_{k,\text{exact}}^{(y)}$ for $\mathfrak{I}_k^{(y)}$ (to be determined below). Equation (3.19) becomes:

$$\begin{cases} \dfrac{1}{2}\left(\dfrac{\partial p}{\partial t} + \rho c \dfrac{\partial v}{\partial t}\right) = -\alpha_5 \left(p - p_{\text{target}}\right) + a\left(\mathfrak{I}_5^{(y)} - \mathfrak{I}_{5,\text{exact}}^{(y)}\right) \quad \text{at} \quad y = 0\,, \\ \dfrac{1}{2}\left(\dfrac{\partial p}{\partial t} - \rho c \dfrac{\partial v}{\partial t}\right) = -\alpha_1 \left(p - p_{\text{target}}\right) + a\left(\mathfrak{I}_1^{(y)} - \mathfrak{I}_{1,\text{exact}}^{(y)}\right) \quad \text{at} \quad y = l_y\,. \end{cases} \tag{3.22}$$

It implies that the modified expressions for $L_k^{(y)}$ are:

$$\begin{cases} L_5^{(y)} = \alpha_5\left(p - p_{\text{target}}\right) + a\mathfrak{I}_{5,\text{exact}}^{(y)} + (1-a)\mathfrak{I}_5^{(y)} & \text{at} \quad y = 0\,, \\ L_1^{(y)} = \alpha_1\left(p - p_{\text{target}}\right) + a\mathfrak{I}_{1,\text{exact}}^{(y)} + (1-a)\mathfrak{I}_1^{(y)} & \text{at} \quad y = l_y\,. \end{cases} \tag{3.23}$$

Equation (3.22) is now the new effective boundary condition, which includes additional transverse damping terms on the RHS. In contrast to the original LODI approach for non-reflecting outflow (equation (3.9)) where all the transverse terms are kept in the effective equation solved at the boundary, here we only retain spatial variations of the transverse terms. In the counterflow configuration, the reference values $\mathfrak{I}_{1,\text{exact}}^{(y)}$ and $\mathfrak{I}_{5,\text{exact}}^{(y)}$ at the outflow boundaries can be calculated based on the potential flow solution (or simply the averaged value of the transverse terms along the boundary) as:

$$\begin{cases} \mathfrak{I}_{5,\text{exact}}^{(y)} = -\dfrac{1}{2}\left(u\dfrac{\partial p}{\partial x} + \gamma p\dfrac{\partial u}{\partial x} + \rho c u\dfrac{\partial v}{\partial x}\right)_{\text{steady}} = \dfrac{c_0^2 - u_p^2}{l_x}\rho_0 u_0 & \text{at} \quad y = 0, \\ \mathfrak{I}_{1,\text{exact}}^{(y)} = -\dfrac{1}{2}\left(u\dfrac{\partial p}{\partial x} + \gamma p\dfrac{\partial u}{\partial x} - \rho c u\dfrac{\partial v}{\partial x}\right)_{\text{steady}} = \dfrac{c_0^2 - u_p^2}{l_x}\rho_0 u_0 & \text{at} \quad y = l_y. \end{cases} \tag{3.24}$$

The transverse damping parameter a in equation (3.22) is a free parameter that we can adjust in the boundary condition. It needs to be kept small in order to suppress any unphysical effects of the transverse terms on the pressure field, yet must be large enough to provide a sufficient damping effect. Our numerical tests shows that, with $a = 0.01$, we can obtain accurate and stable solutions for laminar counterflows with a wide range of stain rates and also for turbulent counterflow flames with different level of fluctuations (shown in the next section).

Figure 3-6 shows the converged pressure and x-velocity fields for a test simulation with an inlet velocity equal to 30 m/s (κ = 6000 s^{-1}) and using $a = 0.01$.

Both the pressure and *x*-velocity fields are correctly reproduced and the solution remains stable over time.

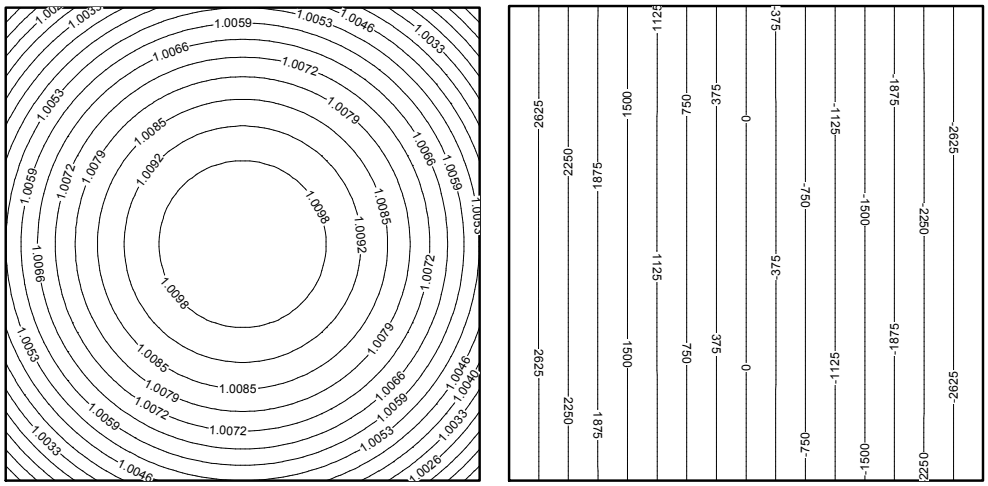

(a) Pressure [atm] (b) *x*- directional velocity

Figure 3-6. The steady pressure and *x*-directional velocity fields using modified non-reflecting outflow boundary conditions equation (3.23) with $a = 0.01$. The inflow velocity is 30 m/s.

Laminar Counterflow Flames

When applying the nonreflecting boundary conditions to a reacting flow configuration, we need to be cautious because of the presence of chemical reaction at the outflow boundaries. Sutherland and Kennedy [70] demonstrated that flames might generate large pressure perturbations into the computational domain while passing through a nonreflecting outflow boundary. They proposed a specific treatment of the reaction source terms in order to mitigate this problem. The pressure variation may be reduced by explicitly accounting for the reactions source terms in the expressions for L_k, in a way that is similar to that we treat the transverse terms for multidimensional flows.

To incorporate this modification, the wave amplitude expressions in equation (3.23) are now taking the following form:

$$L_1^{(y)} = \alpha_1\left(p - p_{\text{target}}\right) + a\mathfrak{I}_{1,\text{exact}}^{(y)} + (1-a)\mathfrak{I}_1^{(y)} + S_1^{(y)}, \tag{3.25}$$

where $S_1^{(y)} = \left(s_p - \rho c s_v\right)/2$, and s_p, s_v are defined in equation (3.3).

A test simulation was performed for a steady hydrogen-air nonpremixed flame in a two-dimensional counterflow field with a domain size of 0.5 cm × 1.0 cm for which a 500 × 500 grid resolution is used, as shown in figure 3-7. A detailed chemical reaction mechanism proposed by Mueller et al. [76] was used. The nonreflecting inflow conditions, equation (3.14), are imposed at the boundaries in the x-direction, and the nonreflecting outflow conditions, equation (3.25) with $a = 0.01$, are used at the boundaries in the y-direction. The inflow velocity is 10 m/s at x = 0, corresponding to a stain rate κ of about 4250 s^{-1}. The inlet temperature and the reference pressure are, respectively, 300 K and 1.0 atm. To locate the flame near the center of the domain, 50 % nitrogen by volume is added to the fuel side stream and the inlet velocities are chosen to achieve the same momentum flux at both inlets, $\left(\overline{\rho u}^2\right)_0 = \left(\overline{\rho u}^2\right)_{l_x}$. The initial solution field was obtained from a steady solution calculated by the OPPDIF code [58], which was mapped into the uniform grid used in the two-dimensional domain.

Figures 3-7a and 3-7b show the streamlines and the isocontours of temperature and pressure of the simulated steady-state hydrogen-air nonpremixed flame. Despite the relatively small domain size compared to the flame thickness, no numerical artifact is visible at any of the domain boundaries. Figure 3-8 further shows the temperature and velocity profiles along the centerline (y = 0.5), compared with

those of the initial conditions generated from the OPPDIF code. Even if the initial conditions are obtained with a plug flow which has zero *y*-directional velocity at inlets, the steady solution demonstrates that the velocity fields are maintained exactly as desired and the flow field converges to a potential flow.

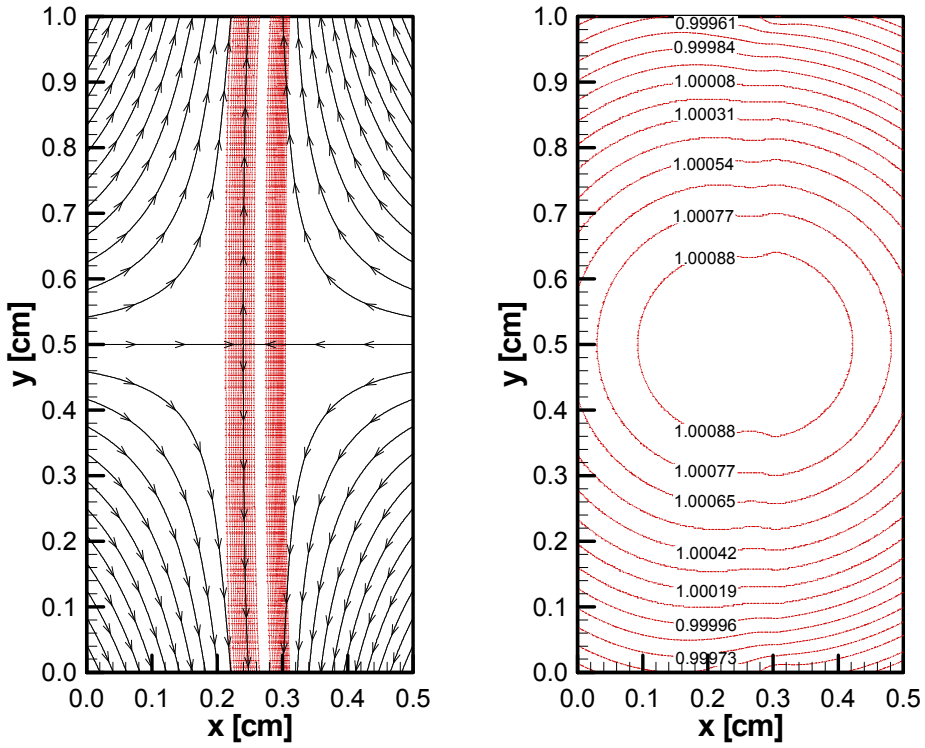

(a) Temperature field (b) Pressure field [atm]

Figure 3-7. The steady H_2-air nonpremixed counterflow: (a) streamlines (solid) and temperature (dotted) and (b) pressure isocontours.

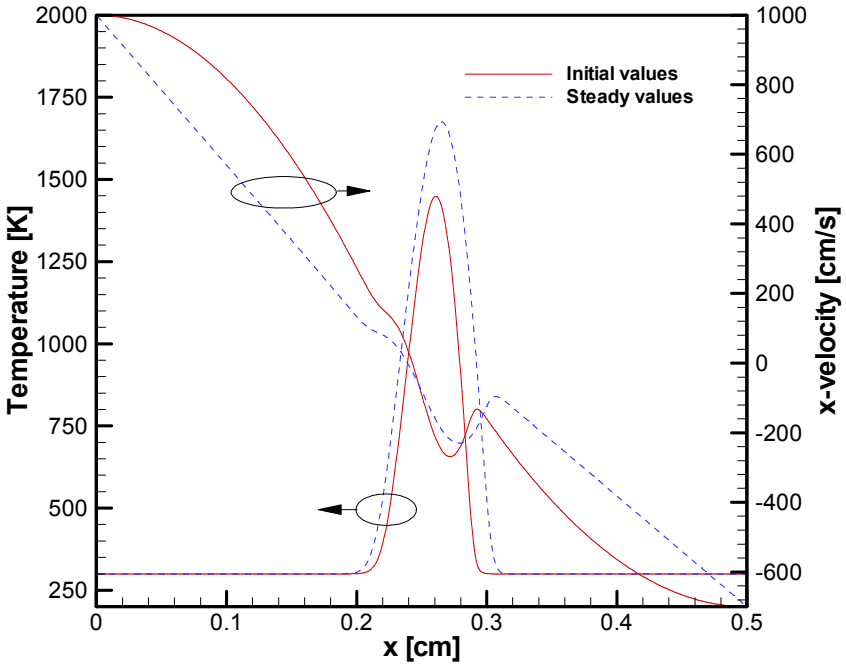

Figure 3-8. The temperature and *x*-directional velocity profiles of the initial and steady H_2-air nonpremixed counterflow flame.

3.4. Application to Turbulent Counterflow

Encouraged by the successful simulations of laminar counterflows, the nonreflecting boundary conditions are now applied to more challenging problems corresponding to turbulent flows. There are two additional difficulties in simulating a turbulent counterflow. One is the introduction of unsteady turbulent-like perturbations through the inlet boundaries. The other is the stability of the solution in highly turbulent situations. We will evaluate the performance of the enhanced boundary conditions related to these two issues in a non-reacting turbulent counterflow test and finally demonstrate the capability to simulate a turbulent counterflow flame using our fully compressible code.

Nonreacting Turbulent Counterflow

We evaluate here the overall S3D ability to simulate a statistically stationary turbulent counterflow configuration. The configuration and steady solution shown in figure 3-6 are used as initial conditions. The inflow conditions correspond to equation (3.14) with the relaxation coefficients, $-\eta_1 = -\eta_2 = \eta_3 = \eta_5 = 10$ (see appendix A in [74] to find the relationship between the non-dimensional coefficients η_k and the dimensional coefficients β_k used in equation (3.14)). The imposed inlet velocities at $x = 0$ are given by $u_0(y,t) = \bar{u}_0 + u_0'(y,t)$ and $v_0(y,t) = \bar{v}_0 + v_0'(y,t)$, where $u_0'(y,t)$ and $v_0'(y,t)$ are the turbulent fluctuation velocities. They are taken from an auxiliary homogenous isotropic turbulent flow field based on a prescribed energy spectrum [77]. $u_0'(y,t)$ and $v_0'(y,t)$ correspond to a one-dimensional slice of the two-dimensional auxiliary field [78]. The slice location is determined using Taylor's hypothesis and the mean inflow velocity $\bar{u}_0$. The turbulent perturbations are characterized by a RMS velocity u' and an integral length scale L_{11}. We use here: u' = 2 m/s and L_{11} = 0.34 mm. The turbulent Reynolds number is approximately equal to 43.

Figures 3-9a and 3-9b show the temporal variations of local *x*-velocity at $(x,y) = (0, l_y/2)$ and global minimum pressure (over the computational domain) for different values of the parameter *a*. For $a = 0.0$, the solution fails at *t* = 1.75 msec due to a numerical instability, similar to what was observed in the steady test (see case (c) in figure 3-5) although the calculated velocity follows the imposed value very closely. For $a = 1.0$, the temporal pressure variations become unacceptably large. These large pressure variations are attributed to an over-relaxation effect associated

with the treatment of the transverse term in equation (3.23). In contrast, for $a = 0.01$, the pressure variations are reasonably small, the calculation does not suffer from instability, and the temporal variations of inflow velocity follow the prescribed values. These results confirm that the weight factor a may be calibrated to ensure both stability and small pressure variations in DNS of turbulent counterflow configurations.

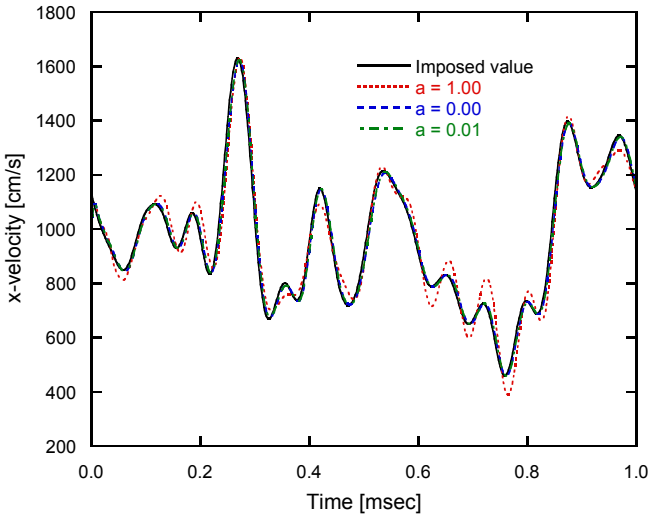

(a) x-directional velocity

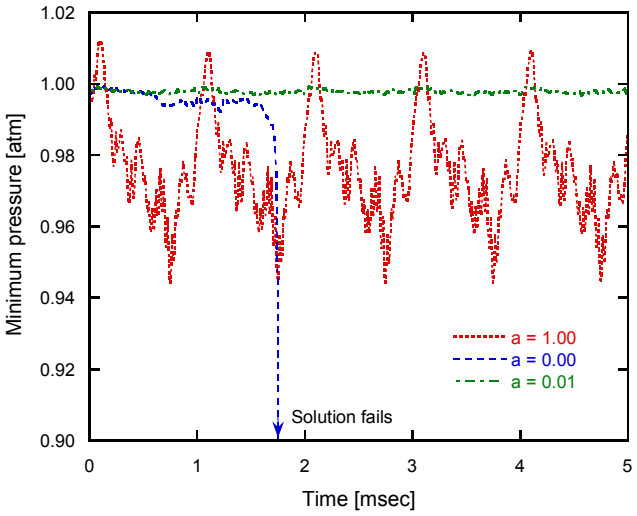

(b) Minimum pressure

Figure 3-9. The temporal variations of (a) the imposed and calculated velocities and (b) the minimum pressure at $x = 0$ and $y = l_y/2$ for a nonreacting counterflow for various choices of a.

Turbulent Counterflow Flames

The modified turbulent inflow/outflow boundary conditions are applied by Yoo et al. [74] to simulate a reacting counterflow system. The results are presented here to show the new capability allowed by current boundary conditions. The steady hydrogen-air strained laminar flame described in section 3.3 is used as initial condition and turbulent-like perturbations are injected at both inflow boundaries as described above.

Figure 3-10 shows the vorticity and temperature isocontours at various times during the simulation. The injected turbulent eddies are convected toward the interior of the domain, thereby interacting with the nonpremixed flame. The initial plane flame is distorted and wrinkled in response to the turbulent fluctuations in the velocity field. Throughout the entire period of intense interaction between the turbulence and the flame, the velocity at the inflow boundary are maintained as the prescribed value.

Figure 3-11 plots the temporal variations of the global maximum and minimum pressures during the simulation. Despite the strong flame-turbulence interaction, the pressure variations show that the initial spurious acoustic waves are damped out smoothly during the early period of the simulation and the solution remains stable during the entire simulation.

Finally, figure 3-12 presents a scatter plot of temperature versus the scalar dissipation rate, χ, both quantities being evaluated on the stoichiometric surface at t = 0, 0.1, 0,3, and 0.8 msec. As turbulent eddies are convected towards the flame, the flame undergoes variations in scalar dissipation rate. At t = 0.8 msec, the range of

scalar dissipation rate at the flame locations is very large, varying from 500 s^{-1} to 1700 s^{-1}. Overall, the nonreflecting boundary conditions developed in the present study are found to work effectively in the simulation of turbulent counterflow diffusion flames. Interesting physics related to turbulent combustion theory and modeling can be studied in the counterflow configuration with our DNS tool.

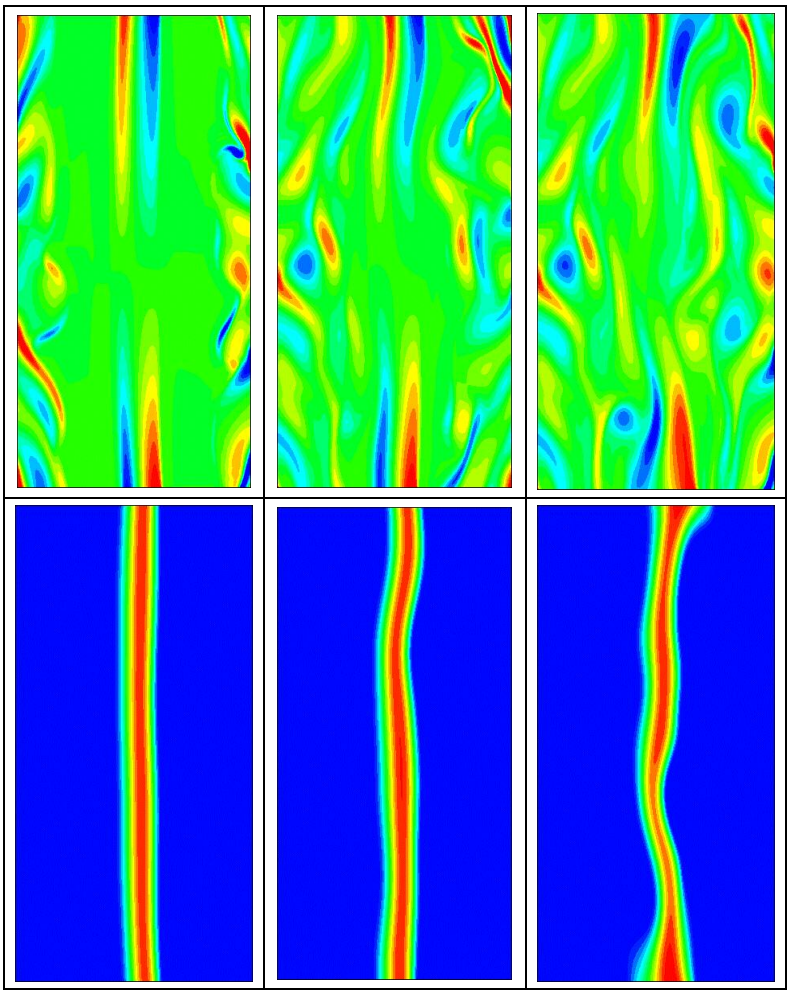

Figure 3-10. The temporal evolution of vorticity (top) and temperature (bottom) fields in hydrogen-air nonpremixed counterflow. From left to right, t = 0.1, 0.3, and 0.8 msec.

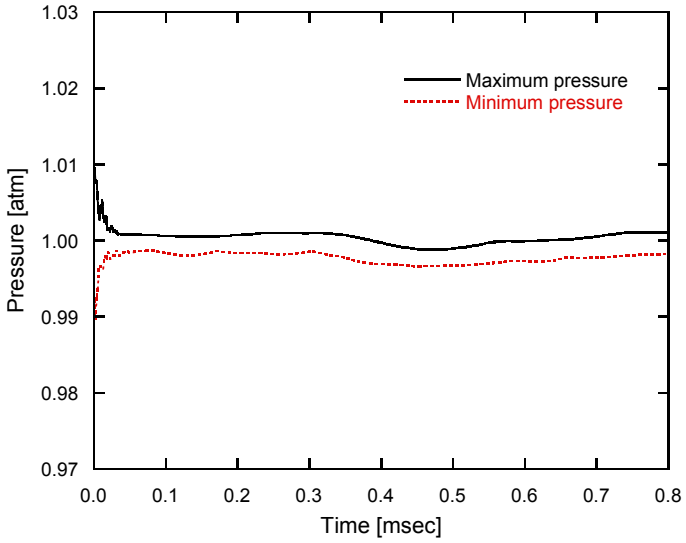

Figure 3-11. The temporal variations of the maximum and minimum pressures for turbulent nonpremixed counterflow flame.

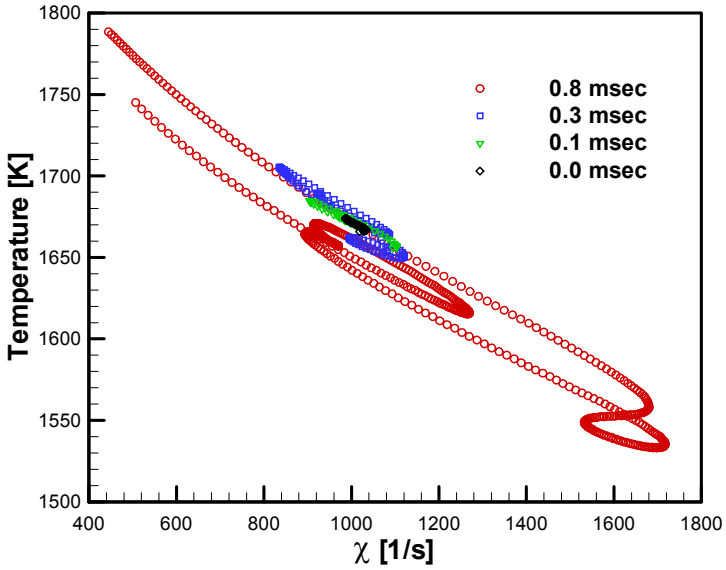

Figure 3-12. Scatter plot of temperature versus scalar dissipation rate χ along the stoichiometric line at t = 0, 0.1, 0.3, and 0.8 msec.

3.5. Concluding Remarks

Turbulent counterflow flame configurations have emerged as one of the basic flame-flow geometry used in studies of turbulent combustion. We adapt our high-fidelity direct numerical simulation (DNS) solver using a fully compressible flow formulation and characteristic-based boundary conditions to the simulation of turbulent counterflow flames. The boundary conditions formulation is improved to better balance the conflicting requirements of maintaining the mean flow field, while suppressing spurious acoustic wave reflections. The formulation is modified in order to properly account for multi-dimensional effects and solution variations in planes parallel to the computational domain boundaries. The enhanced boundary scheme is tested in a series of benchmark simulations corresponding to laminar or turbulent, nonreacting or reacting counterflow configurations. The results are encouraging and are viewed as a step towards an extension of the domain of application of DNS tools to laboratory-scale flame configurations.

Chapter 4: Soot Model

4.1. Introduction

Soot is one of the major pollutants from gas phase combustion. It corresponds to solid particles generated in flames of many industrial combustors and open fires. Soot is mainly composed of carbon atoms together with small amounts of hydrogen and oxygen. Soot particles are generally small ranging in size between 5nm to 80nm. For environmental reasons, we want to minimize the amount of soot yield from engines and furnaces because it causes severe diseases in the human respiratory system [79]. In terms of efficiency, carbon atoms contained in soot are an indication of incomplete combustion and reduced efficiency. In addition, soot is responsible for large fractions of radiative heat loss in a luminous flame, especially in large-scale fires. At the flame temperature, soot strongly radiates in a continuous spectrum and changes significantly the emissive and absorptive properties of the participating medium. Besides its influence on flame temperature, soot also changes the profile of other species, like NO_x and CO, through both thermal and chemical interactions [80]. In short, it is of great interest to accurately predict soot formation, because of its importance as a pollutant and also its influence on flame structure through thermal radiation and chemical kinetics.

The amount of soot yield from a flame is the result of a competition between soot formation and oxidation. Soot particles are produced on the fuel rich side of a flame. As sooty parent fuels pyrolyze, they produce smaller hydrocarbons, in particular C_2H_2, which leads to the formation of aromatic species (like benzene) and larger polyaromatic hydrocarbons (PAH). C_2H_2 and PAH are major gas phase

precursors of soot particles. The initial transformation from gaseous molecules to solid particles is called particle inception or nucleation. Once soot particles are formed, they can grow by two mechanisms: surface growth and coagulation. Surface growth is a heterogeneous process in which gas phase molecules react with soot molecules on the soot surface. Coagulation is a mostly physical process of the agglomeration of soot particles. Coagulation changes the number of soot particles, but not the soot mass. The three phases of soot formation, namely nucleation, surface growth and coagulation, are quite different chemical and physical processes, and are normally modeled separately. As the soot particles move towards the air side of the flame zones, soot oxidation starts to compete with soot growth processes. Soot mass is reduced through oxidation of particles primarily by OH and O_2. For more detailed descriptions of soot formation and modeling, see Kennedy's review paper [81].

Many attempts have been made over the last two decades to model the soot formation and burnout in combustion systems [81, 82]. There is a wide range of soot models with different level of complexity and accuracy available in the literature. The empirical models use experimental correlations to estimate the soot loading. At the other end of the spectrum, there are models, like the method-of-moments model [83] and the sectional method [84], that try to describe the detailed kinetics of soot formation through elementary chemical reactions. Currently, these detailed chemical reaction models still possess some uncertainty and the overwhelming computational requirement prevents their wide use in multidimensional numerical simulations. We consider in the following an intermediate approach that corresponds to a class of semi-empirical models and is a good compromise between accuracy and cost for

DNS. In contrast to empirical models, these models solve transport equations for soot quantities; in contrast to detailed soot models, the rates of soot formation and oxidation in the transport equations are modeled with experimental correlations. We focus our discussion below on semi-empirical soot models.

4.2. Semi-empirical Soot Models

Moss and coworkers [85-87] proposed a semi-empirical soot model for diffusion flames. Transport equations of soot number density (n) and volume fraction (f_v) are solved along with the Navier-Stokes equations. The equations are:

$$\begin{cases} \dfrac{\partial(n/N_0)}{\partial t} + \dfrac{\partial(n/N_0 u_i)}{\partial x_i} = -\dfrac{\partial(n/N_0 V_{t,i})}{\partial x_i} + \dot{\omega}_{(n/N_0)}, \\ \dfrac{\partial(\rho_s f_v)}{\partial t} + \dfrac{\partial(\rho_s f_v u_i)}{\partial x_i} = -\dfrac{\partial(\rho_s f_v V_{t,i})}{\partial x_i} + \dot{\omega}_{(\rho_s f_v)}, \end{cases} \tag{4.1}$$

where N_0 is the Avogadro number (6×10^{26} molecules/mole), ρ_s the density of soot, taken as that of solid carbons (1.8×10^3kg/m^3). The mass diffusion coefficient for the particulates is assumed to be negligibly small, but the thermophoresis effect is included via a thermophoresis velocity $V_{t,i}$ [88]:

$$V_{t,i} = -0.54\nu\frac{\partial}{\partial x_i}\ln T\,. \tag{4.2}$$

The source terms $\dot{\omega}$ in the equations for number density and volume fraction are modeled as:

$$\dot{\omega}_{(n/N_0)} = \alpha(\xi) - \beta(\xi)(n/N_0)^2\,, \tag{4.3}$$

$$\dot{\omega}_{(f_v\rho_s)} = \gamma(\xi)n + \delta(\xi)\,. \tag{4.4}$$

$\alpha(\xi)$ and $\delta(\xi)$ are the contributions of particle inception to the increase in soot number and mass respectively. The second term on the right hand side of equation (4.3)

accounts for the reduction in number of particles as a result of coagulation. The first term on the right hand side of equation (4.4) represents the increase in soot mass due to surface growth. The rates of the processes are functions of the local density ρ, temperature T, and fuel mole fraction X_c:

$$\begin{cases} \alpha(\xi) = c_\alpha \rho^2 T^{1/2} X_c \exp(-T_\alpha / T), \\ \beta(\xi) = c_\beta T^{1/2}, \\ \gamma(\xi) = c_\gamma \rho T^{1/2} X_c \exp(-T_\gamma / T), \\ \delta(\xi) = c_\delta \alpha(\xi). \end{cases} \tag{4.5}$$

The model parameters c_i and activation temperatures T_i have been calibrated against detailed measurements of several fuels, including ethylene [85], kerosene and methane [86]. Notice that in equation (4.4) the rate of surface growth is proportional to the number of soot particles. Moss et al. [87] argued that surface growth was only weakly dependent on the available soot surface. Moss and coworkers neglected the surface area dependence when describing surface growth in sooty ethylene flame[85, 87], but chose to incorporate a surface area dependence in weakly sooty methane flames [86]. Kaplan and coworkers [89-91] implemented Moss's soot model [86] in a series of studies on methane diffusion flames and demonstrated the robustness of the model. In a later work, Moss et al. [87] extended their original model [85] to include the oxidation of soot by OH radicals, recognizing that OH plays an important role in soot oxidation:

$$\dot{\omega}(f_v \rho_s) = \gamma(\xi) n + \delta(\xi) - S \dot{\omega}_{ox}, \tag{4.6}$$

$$S = \pi d^2 n = (36\pi n)^{1/3} f_v^{2/3}, \ \dot{\omega}_{ox} = 1.27 \times 10^3 \Gamma X_{OH} T^{-1/2}, \tag{4.7}$$

where S represents the total surface area of soot per unit volume and has the unit of [1/m]. Note that this model implicitly assumes a uniform spherical-shaped particle size distribution. S is related to n and f_v through the expression of the diameter of soot particles $d = \left(\frac{6}{\pi} \frac{f_v}{n} \right)^{1/3}$. Γ is an empirical collision efficiency coefficient, taken to be 0.1.

In addition to Moss's model, there is another family of semi-implicit soot models developed by Lindstedt and coworkers [92-94], which are also widely used. Similar to the approach of Moss, these authors added two conservation equations describing soot formation and burnout into the fluid flow equations, namely equations for soot number density and soot mass fraction. The major difference with the model developed by Moss is the adoption of acetylene as the indicative species for soot nucleation and surface growth instead of the parent fuel. Lindstedt pointed out that soot formation depends upon the breakdown path of the fuel and hence pyrolysis products, such as acetylene, are of primary importance to the soot formation process. Although the approach where formation of soot is linked directly to the fuel concentration had been found to work well for conditions close to those where the models were calibrated, the application of such models to appreciably different conditions might yield significant errors. Leung and Lindstedt [92] used their soot model combined with detailed chemistry of the gas phase reaction to simulate counter flow ethylene and propane flames. Fairweather et al. [93, 95] applied this soot model to turbulent non-premixed flames. Lindstedt [94] extended the model by adding benzene as an indicative species in soot nucleation. Computations showed that the extra nucleation step based on benzene improved the soot volume fraction predictions

in propane flames, while it did not have much of an effect for small molecular weight fuels like ethylene. He also compared different models for soot mass growth and found that the model assuming that the growth rate was proportional to the number density produced the best agreement with experiments, while the one assuming linear dependence on particle surface area was not satisfactory. Ezekoye and Zhang [96] applied Fairweather et al.'s [95] model to a microgravity counter-flow diffusion flame. The OH oxidation step from Moss [87] was modified and added to this model. By using the rate constant of Moss, the authors found that the effect of OH oxidation was over-predicted. To match the experimental results, a factor of 10 was introduced to reduce the oxidation rate. It is worth noting that recent developments by Moss and coworkers [87, 97] also considered the effect of acetylene in the soot formation rates.

In general, most semi-empirical soot models are based on solving additional conservation equations for soot number density and mass. The model chosen should be dependent on the fuel and chemical kinetics used for the simulation. The following features for the available soot formation models should be noted:

1. The adoption of acetylene as an indicative species of nucleation and surface growth is broadly accepted, at least for small molecular weight fuels, where benzene is not an important intermediate product of the reactions.
2. The oxidation of soot, especially that by OH radicals should be included in the model, since a lot of studies have shown that the effect of OH is larger than that of O_2.

3. Surface growth mechanisms are still under debate. Even in the same research group, different approaches have been used without clear justifications. The available choices are that surface growth is proportional to number density [85, 87, 94], proportional to surface area [86, 96, 97], or a non-linear function of surface area [92, 95].
4. The model coefficients vary considerably according to the choices of models, fuels and configurations. The coefficients are calibrated to match experimental data. Ad hoc adjustments are frequently made in computations of a new configuration.
5. The transport equations of soot quantities used by different authors are not the same. For example, Fairweather et al. [95] included diffusivity but did not incorporate the effect of thermophoresis; Moss and coworkers [85] included thermophoresis but neglected diffusivity; in Ezekoye and Zhang's study [96], both mass diffusivity and thermophoresis were used. Our own tests show that in the context of a high-order numerical solver, the diffusion term is necessary to maintain stability of the soot equations.

4.3. Implementation in S3D and Validation

In S3D, two additional transport equations for the soot model are added as follows:

$$\begin{cases} \dfrac{\partial}{\partial t}\left(\dfrac{n}{N_0}\right)+\dfrac{\partial}{\partial x_i}\left(\dfrac{n}{N_0}u_i\right)=\dfrac{\partial}{\partial x_i}\left[\dfrac{\nu}{Sc}\dfrac{\partial\left(n/N_0\right)}{\partial x_i}\right]-\dfrac{\partial}{\partial x_i}\left(\dfrac{n}{N_0}V_{t,i}\right)+\dot{\omega}_{(n/N_0)}, \\ \dfrac{\partial\left(\rho Y_s\right)}{\partial t}+\dfrac{\partial\left(\rho Y_s u_i\right)}{\partial x_i}=\dfrac{\partial}{\partial x_i}\left[\rho\dfrac{\nu}{Sc}\dfrac{\partial\left(Y_s\right)}{\partial x_i}\right]-\dfrac{\partial\left(\rho Y_s V_{t,i}\right)}{\partial x_i}+\dot{\omega}_{(\rho Y_s)}, \end{cases} \tag{4.8}$$

where *Sc* is a Schmidt number for soot, and is specified to be 1000 as suggested by Ezekoye [96]. Soot mass fraction and volume fraction are related by the following relation: $\rho Y_s = \rho_s f_v$.

We consider different models for the soot production rates, depending on the fuel type. For methane combustion, we adopt the model of Syed et al. [86], plus the oxidation sub-model used by Brookes et al. [97]. For ethylene combustion, the expression of the soot formation rates are the same as for methane except that the surface growth rate is taken to be proportional to number density, as suggested by Moss et al. [87].

The semi-empirical soot models have been successfully applied in both coflow [89-91, 98] and counterflow [80, 92] diffusion flames. To validate the model and implementation, we use S3D to simulate a two-dimensional ethylene-air counterflow diffusion flame and compare the results against experimental data [99]. The simulated flame corresponds to a steady counterflow laminar diffusion flame with a strain rate equal to 63 s^{-1}. The fuel stream is pure ethylene; the oxidizer stream is a mixture of 22% oxygen and 78% nitrogen. The soot quantities of this flame have been measured by Vandsburger et al. [99] using a Tsuji burner. Westbrook and Dryer's single step mechanism [100] is adopted in the current simulation to reduce the computational time. We use an OPPDIF solution [58] as initial conditions. Boundary conditions are those developed in the previous chapter. Radiative heat loss is included in the simulation using the optically thin model. We use a 400×24 grid for a 2.48×0.3 cm^2 computational domain. The flow field in counterflow diffusion flames is two-dimensional, but the flame structure is essentially one-dimensional. To

reduce computational cost, we use a small domain size and relatively coarse resolution in the cross-stream direction. Tests show that the domain size and resolution in this direction have little effect on the steady one-dimensional flame structure.

The expressions of the soot formation and oxidation rates are those proposed by Moss et al. [87]:

$$\dot{\omega}_{(n/N_0)} = c_\alpha \rho^2 T^{1/2} X_c \exp(-T_\alpha / T) - c_\beta T^{1/2} (n/N_0)^2, \tag{4.9}$$

$$\dot{\omega}_{(n/N_0)} = c_\alpha \rho^2 T^{1/2} X_c \exp(-T_\alpha / T) - c_\beta T^{1/2} (n/N_0)^2, \tag{4.10}$$

$$\dot{\omega}_{ox} = 1.085 \times 10^5 X_{O_2} T^{-1/2} \exp(-19778/T). \tag{4.11}$$

Model coefficients are listed in table 4-1. Note that, in [87], the total hydrocarbon concentration was employed as the fuel concentration in the computation of soot formation rate. Since we are using single step chemistry, only the concentration of the parent fuel (C2H4) is available, we use it in the current simulation. For the same reason we neglect the soot oxidation due to OH, and only incorporate the oxidation by O2.

	c_α	c_β	c_γ	c_δ	T_α	T_γ
Original	6.0×10^{6}	2.25×10^{15}	6.3×10^{-14}	144	4.61×10^{4}	1.26×10^{4}
Modified	6.0×10^{6}	2×10^{14}	0.8×10^{-14}	144	4.61×10^{4}	1.26×10^{4}

Table 4-1. Original [87] and modified rate coefficients for the ethylene soot formation model.

We first look at the locations of the reaction and soot formation zones in the diffusion flame. Figure 4-1 presents the one-dimensional structure of the computed steady state solution. From the streamwise velocity profile, we can see that the

stagnation plane is located at $x = -0.14$ cm. The peak temperature and reaction zone is on the oxidizer side of the stagnation plane ($x = 0.08$ cm). The profile of soot mass reaction rate shows that soot is generated on the fuel-rich side of the flame. After soot particles are generated, they are transported away from the flame (to the left) by convection. Finally soot gathers and forms a peak near the stagnation plane, as shown in the soot volume fraction profile. The same behavior is also found in the experimental work by Hwang and Chung [101]. Since the soot particles, after being formed, do not transport towards the reaction zone, the oxidation rate of soot is one order of magnitude smaller than the formation rate. This kind of flame is classified as soot formation (SF) flames in [101].

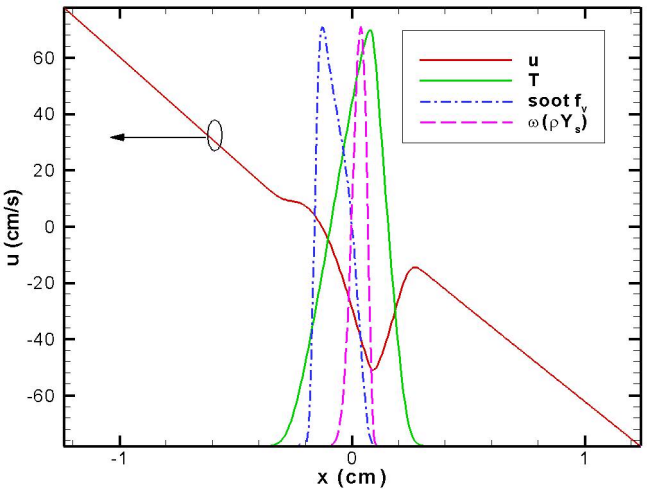

Figure 4-1. Steady solution of the laminar counterflow diffusion flame. Red solid line: streamwise velocity; Green solid line: temperature; Blue dash-dotted line: soot volume fraction; Purple dashed line: source term in soot mass fraction equation. Last three quantities are non-dimensionalized for a better illustration.

Next we compare the computed soot quantities against the experimental data by Vandsburger et al. [99] and computational results by Leung et al. [92]. The

computed peak flame temperature (2320K) is relatively high compared to the experiment data (1930K). One of the reasons is that we use a single step irreversible mechanism. The OPPDIF simulation with detailed C2H4 mechanism gives a peak temperature of 2171K (with only gas phase radiation). Another reason could be that in the experiment, heat losses to the Tsuji burner reduce the flame temperature. Figure 4-2 shows the profiles of soot number density and volume fraction. Compared with experimental measurements, the S3D simulation underpredicts the peak number density by about 60%, while it overpredicts the peak volume fraction by 170%. Reasons for the discrepancies could be the following: first, the soot model used has calibrated against co-flow diffusion flames [87], it may not work equally well for a counter-flow diffusion flame configuration; second, the single-step chemistry model we use to describe the combustion cannot provide all the information that the soot model requires, like the correct flame temperature, concentration of C2H2 and OH. To reduce the discrepancies, we propose to adjust the model coefficients.

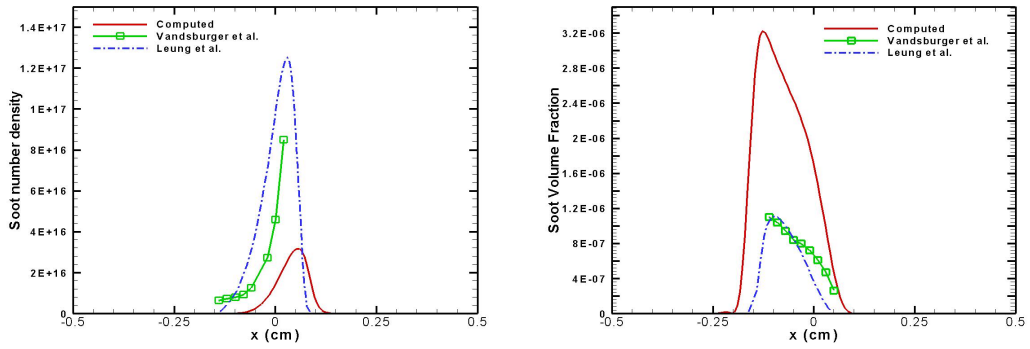

(a) (b)

Figure 4-2. Comparison of S3D soot quantities with experimental and reference computational data. The S3D predictions use the original model coefficients. (a): soot number density. (b): soot volume fraction.

As Moss et al. [87] pointed out, the particle number density typically saturates rapidly and a local balance is established between nucleation and coagulation such that (from equation (4.3)):

$$\left(n / N_0\right)^2 = \frac{c_\alpha}{c_\beta} \rho^2 X_c \exp(-T_\alpha / T) . \tag{4.13}$$

Since we under-predict the number density using the original parameters, we could reduce c_β to achieve the correct peak soot number density. According to the above relation, to increase the number density by a factor of 3, we should reduce c_β by a factor of 9. Now suppose we have the right number density prediction, we need to calibrate the soot mass fraction accordingly. The major contribution to the source term of soot mass fraction is the surface growth rate. In Moss's model the surface growth rate is proportional to number density. The number density has been increased, so we reduce the surface growth rate (c_γ) accordingly. Besides the coefficients for coagulation and surface growth, we keep other model parameter unchanged. The original and modified parameters are listed in table 4-1. The results from the modified soot model are presented in figure 4-3. The predicted peak soot number density is about 10% higher than the experimental data, while the peak volume fraction is about 40% higher. If we use a detailed mechanism, flame temperature will be reduced by about 200K, a better prediction of soot quantities would be expected. (Note that Leung et al. [92] introduced a heat loss factor in the temperature profile to match the experiment in their simulations of soot formation.)

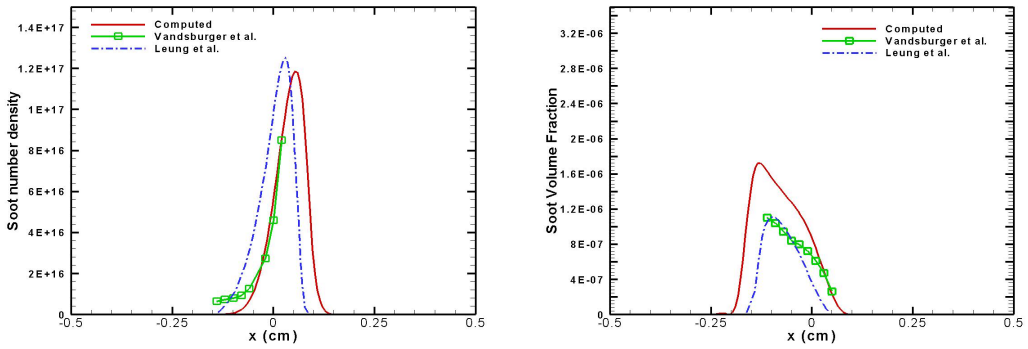

(a) (b)

Figure 4-3. Comparison of computed soot quantities with experimental and computational data. Modified model coefficients are used. (a): soot number density. (b): soot volume fraction.

In conclusion, a two-equation semi-empirical soot model has been implemented into S3D. This model is proposed as a good compromise between computational cost and accuracy, and therefore is suitable for the current DNS capability. The model coefficients are calibrated against experiments with specific fuel type and flow conditions. If the computational conditions are different, the coefficients might need further adjustments. The soot model has been tested in a C_2H_4 counterflow diffusion flame. The qualitative behavior is correctly captured, and using the modified model coefficients, we can obtain better agreement with experimental data.

Chapter 5: Thermal Radiation

5.1. Introduction

Thermal radiation is an important, sometimes dominant, mode of heat transfer in combustion systems. In large-scale sooty fires, about 25-35% of the combustion energy is transported out of the flame by thermal radiation [102]. In flame spread problems, the radiative heat flux combined with the convective heat flux determines the pyrolysis rate of the solid flammable material and therefore the rate of flame spread [103]. In compartment fires, the radiation from the hot smoke layer accumulated in the upper part of the room accounts for most of the energy transfer in the late stage of a fire development and is directly responsible for the transition to flashover [104]. Concerning the flame zone structure, thermal radiation results in modifications of the flame temperature, thickness [105], pollutant profiles [105, 106], and the extinction limit [107] as well. Therefore accurate prediction of radiative heat transfer is crucial in a high-fidelity direct numerical simulation of a combustion system. Most previous DNS studies simply neglected thermal radiation or used an optically thin model (OTM). However this emission-only model is usually inadequate in the sense that it over-predicts the radiative heat loss from the gas mixture due to the neglect of self-absorption, and also that it is not applicable in the cases with the presence of a solid surface, like in a combustion chamber, because OTM does not provide the heat flux incident on a surface. For RANS and LES applications where real laboratory-scale flames and engineering problems are solved, radiation calculations cannot be avoided. However, little is known about flame turbulence-

radiation interactions (TRI), therefore most RANS/LES simulations do not take TRI into account. A DNS capability enhanced with combustion and thermal radiation may provide the validation tool needed for RANS/LES modeling of this problem [108, 109].

The governing equation for thermal radiation transport with a participating medium is called the radiative transfer equation (RTE) (see equation (5.1)), which is an integro-differential equation with six independent variables: spatial coordinates (x, y, z), direction (polar angle θ, azimuthal angle φ) and wavelength (λ). The extra dependence on direction and wavelength makes RTE very difficult and expensive to solve. Many different solution methods have been developed, namely the zonal method, the spherical harmonics method, the discrete ordinate method, the discrete transfer method, the Monte Carlo method, and so on. Thorough discussions of these methods, including advantages and limitations, can be found in [110-112]. For coupled CFD-radiation simulations, the discrete ordinates method (DOM) [113] and discrete transfer method (DTM) [114] are more popular, due to their advantages in efficiency and simplicity. The discrete ordinates method discretizes the directional space into a finite number of ordinates, and each has a corresponding weight factor. The RTE is solved for each ordinate and the total contribution over the directional space is approximated by a quadrature summation from all the ordinates. This method is also referred to as an S_n approximation, where n represents the order related to the number of discrete ordinates. In contrast, the discrete transfer method is a ray tracing method where the RTE is integrated along a set of representative rays. It has a straightforward physical interpretation and is flexible in treating complex geometries.

The comparison between the two methods has been made in [112, 115], but not in the context of DNS.

Our objective is to develop a parallel thermal radiation solver that is economical, accurate and compatible with our code S3D. Here, we adopt the discrete transfer method (DTM), and will compare the parallel DTM solver with the DOM solver developed by our collaborators at the University of Michigan. Most previous applications of discrete transfer method calculations were performed with a single processor. To the best of our knowledge, reference [116] is the only study that couples DTM with a flow field simulation in a parallel computing mode. However the algorithm used in [116] does not have good scalability and is limited to only a small number of processors. In the following, we will first describe the discrete transfer method, followed by the parallelization strategy that we have adopted. Then we validate the code by several test cases. And finally the DTM is applied to a transient flame vortex interaction simulation and compared with a DOM solver.

5.2. Discrete Transfer Method

The Discrete Transfer Method (DTM) was proposed by Lookwood and Shah [114] to compute radiative heat transfer in combustors. The advantages of DTM are: conceptual simplicity, easy application to complex geometries, and easy control of precision by changing the solid angle discretization. The main idea of this method is briefly described below.

The radiative energy balance along any direction $\hat{\mathbf{s}}$ in an emitting-absorbing and scattering medium is described by the RTE [110]:

$$\frac{dI}{ds} = \hat{\mathbf{s}} \cdot \nabla I = \kappa I_b - \beta I + \frac{\sigma_s}{4\pi} \int_{4\pi} I(\hat{\mathbf{s}}_i) \Phi(\hat{\mathbf{s}}_i, \hat{\mathbf{s}}) d\Omega_i \,. \tag{5.1}$$

To simplify the problem, we assume that the medium is gray; hence the dependence on wavelength is dropped off and spectrally-averaged radiative properties are used. In equation (5.1), I represents the radiative intensity, I_b the black body radiative intensity, Ω the solid angle, κ the absorption coefficient, σ_s the scattering coefficient, and $\beta = \kappa + \sigma_s$ the extinction coefficient. Φ is the scattering phase function and satisfies the following property:

$$\frac{1}{4\pi} \int_{4\pi} \Phi(\hat{\mathbf{s}}_i, \hat{\mathbf{s}}) d\Omega \equiv 1 \,. \tag{5.2}$$

For usual combustion gas mixtures with all but very large soot particles, the scattering effect is negligible: $\sigma_s = 0$.

Considering radiative heat transfer, the fluid thermal energy equation takes the following form:

$$\frac{\partial}{\partial t}(\rho E) + \frac{\partial}{\partial x_j}(\rho E u_j) = -\frac{\partial}{\partial x_j}(p u_j) + \frac{\partial}{\partial x_j}(\tau_{ij} u_i) - \frac{\partial q_j}{\partial x_j} + \rho g_j u_j - \frac{\partial q_{r,i}}{\partial x_i} \,. \tag{5.3}$$

The last term on the right hand side of equation (5.3) is the divergence of the radiative heat flux and represents the net radiative energy loss from an infinitesimal control volume. The evaluation of this term is based on the solution of the RTE. The radiative heat flux at a surface with outward normal $\hat{\mathbf{n}}$ is:

$$\mathrm{q_r} \cdot \hat{\mathbf{n}} = \int_{4\pi} I(\hat{\mathbf{s}})\, \hat{\mathbf{n}} \cdot \hat{\mathbf{s}}\, d\Omega \,. \tag{5.4}$$

The divergence of the radiative heat flux can be expressed as follow:

$$\nabla \cdot \mathbf{q_r} = \nabla \cdot \left(\int_{4\pi} I(\hat{\mathbf{s}})\, \hat{\mathbf{s}}\, d\Omega \right) = \int_{4\pi} \hat{\mathbf{s}} \cdot \nabla I(\hat{\mathbf{s}})\, d\Omega = \int_{4\pi} \frac{dI}{ds}\, d\Omega \,. \tag{5.5}$$

Substituting equation (5.1) into the above equation and using equation (5.2), we get:

$$\nabla \cdot \mathbf{q_r} = \kappa(4\pi I_b - \int_{4\pi} I d\Omega) = \kappa(4\pi I_b - G) . \tag{5.6}$$

Equation (5.6) states that physically the net loss of radiative energy from a control volume is equal to the emitted energy minus the absorbed energy.

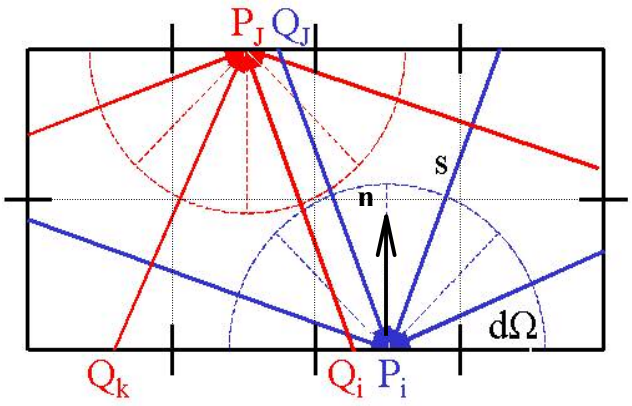

Figure 5-1. Illustration of the domain decomposition and the ray tracing technique in the Discrete Transfer Method.

In the Discrete Transfer Method [114], the computational domain is decomposed into small control volumes as showed in figure 5-1. The temperature and radiative properties of the medium are assumed to be uniform in a control volume. The central point of each boundary cell (*P*) is selected as the place to perform directional discretization. The hemisphere that the boundary surface faces is divided into a given number of solid angles. The radiative intensity is assumed to have no directional variance within each solid angle. The central line of the solid angle *PQ* represents a radiative ray, along which the RTE will be integrated. We will take the radiative intensity at *Q* as the boundary condition of the RTE and trace the ray back through the passing control volumes until the destination *P* is reached.

For example, we consider a gray non-scattering medium. In that cases, the RTE takes the following simple form:

$$\frac{dI}{ds} = \kappa I_b - \kappa I \ . \tag{5.7}$$

Inside a control volume, since the absorption coefficient (κ) and temperature are taken as constant, we can analytically integrate RTE along a radiative ray:

$$I_{n+1} = I_n e^{-\kappa \Delta s} + I_b (1 - e^{-\kappa \Delta s}) \ , \tag{5.8}$$

where I_n and I_{n+1} are respectively the intensity entering and leaving the control volume, Δs is the length of the beam that is intersected by the control volume. The first term on the right hand side describes the part of energy entering the control volume that is transmitted through; the second term is the radiative energy that is emited from the control volume. Using equation (5.8) recursively, the RTE can be easily integrated along a ray from Q to P.

The incident radiative heat flux (irradiation) at the boundary point P is calculated in DTM by a numerical quadrature:

$$G_j = \int_0^{2\pi} I(\hat{\mathbf{s}})\, \hat{\mathbf{n}} \cdot \hat{\mathbf{s}}\, d\Omega = \sum_i I_i D_{j,i} \ , \tag{5.9}$$

where the subscript j is the index of the boundary points P; the subscript i represents different rays that reach point P; I_i is the radiative intensity of the i^{th} ray reaching point P_j; $D_{j,i}$ is the integral of the cosine of the angle between the surface normal at point P_j and the direction of the i^{th} ray QP over a solid angle element $\Delta\Omega$:

$$D_{j,i} = \int_{\Delta\Omega_{j,i}} \hat{\mathbf{n}} \cdot \hat{\mathbf{s}}\, d\Omega = \int_{\Delta\Omega_{j,i}} \cos\theta_{j,i} d\Omega = \cos\theta_{j,i} \sin\theta_{j,i} \sin(\Delta\theta_{j,i}) \Delta\varphi_{j,i} \, . \tag{5.10}$$

Since the solid angles are defined from the discretization of a hemisphere centered at P_j, the following identity holds: $\sum_i D_{j,i} = \pi$.

The integration of the RTE along a ray requires specification of the boundary condition at the point *Q*. If the boundary is a solid wall, like the wall of a combustion chamber, the boundary condition for a gray diffuse surface may be written as:

$$I_j = J_j / \pi = \varepsilon_B \sigma T_B^4 / \pi + (1 - \varepsilon_B) G_j / \pi \,, \tag{5.11}$$

where the subscript *B* represents the values at the boundary. If the boundary is open, the boundary condition is:

$$I_j = I_{in} \,. \tag{5.12}$$

I_{in} is the radiation intensity that transmits from outside of the computational domain. The calculation procedure is iterative if the boundary is a gray wall, since in equation (5.11) the irradiation G_j is not known *a priori* and requires the solution of *I* (see equation (5.9)).

The radiative source term is the net radiative energy deposited in a given control volume, and in DTM it is evaluated by accumulating the contributions from all the rays that pass the control volume:

$$S = -\int_{cv} \nabla \cdot \mathrm{q_r} dv = \sum_k S_k = \sum (I_n - I_{n+1}) D_{j,i} A_j \,, \tag{5.13}$$

where A_j is the surface area of the boundary cell that the radiation beam impinges. The summation acts on all the solid angles (subscript *k*) whose central line pass the control volume. Equation (5.13) actually assumes that all the radiative energy is concentrated on the central line of the solid angle instead of uniformly spreading over it. If the solid angle is completely overlapped by the control volume (as in figure 5-

2a), the source term S_k is accurate according to the definition of radiative intensity. However if the angular discretization is not fine enough, it is very likely that the control volume only partially overlaps the solid angle (as in figure 5-2b). In this case, errors will be introduced in the computed source term. This problem is caused by inadequate number of representative rays, and is called the "ray effect". Note that the ray effect also exists in DOM, where directional space is approximated by a finite number of ordinates [117].

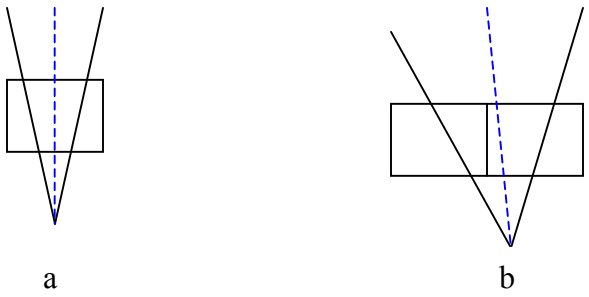

Figure 5-2. Illustration of computation of the radiative source term in the Discrete Transfer Method.

Since the initial development of DTM, many improvements have been proposed over the years. Coelho and Carvalho [118] pointed out that the formulation of DTM is not conservative, that is, the net rate of radiative heat transfer leaving the enclosure through its boundaries is not equal to the difference between the radiative energy emitted and absorbed within the enclosure. This is a consequence of the fact that the angular discretization is performed only for the irradiation rays. The summation of elementary solid angles for all the irradiation rays at each boundary cell equals 2π by construction. However the number of radiative rays leaving one boundary cell is determined by ray tracing. As a result the total solid angle is not

equal to 2π and the relation $I = (J/\pi)$ does not hold. The authors propose a conservative formulation using a global correction factor. However the new formulation does not show much advantage in terms of accuracy. Cumber [119] examined the effect of the quadrature formula on the accuracy of the radiative heat flux. The original ray distribution used by Lookwood and Shah [114] is based on equally spaced angle intervals in both polar and azimuthal coordinates. Cumber proposed a Newton Cotes type of quadrature and showed the added benefits in terms of higher accuracy. He also shows that, instead of using uniform temperature assumption as in equation (5.7), a linear distribution of temperature along the radiation beam could be used to integrate RTE. Versteeg et al. [120-122] studied the truncation errors in the heat flux integral of DTM, both for transparent medium [120] and participating medium [121, 122]. The errors in heat flux due to the boundary surface discretization and hemisphere discretization were discussed based on Taylor series expansions. As pointed out by the authors, this error analysis would not be instructive unless a very large number of rays was used, typically more than 500, since otherwise the small solid angle approximation used in the analysis was invalid. Recently Cumber [123] and Versteeg [124] presented an adaptive angular quadrature strategy to mitigate ray effects on radiative heat flux. Although the number of rays necessary to achieve a given numerical error is decreased, the computational overheads and complexity associated with error estimation and adaptation treatment make the method a formidable task for a CFD simulation coupled with radiation. So far, most error analysis and improvement studies have focused on the calculation of the radiative heat flux. For a coupled CFD-radiation simulation, a more important

issue is the spatial distribution of the radiative power density. However, no error analysis is available for the DTM treatment of the source term distribution.

5.3. Parallelization of DTM

Novo et al. [125] have studied the parallelization of DTM in the context of a stand-alone radiation simulation. The parallelization of DTM can be achieved by a wavelength decomposition, a ray decomposition or a spatial domain decomposition. In the case of a gray medium, as considered in the present work, only the last two options are available.

Ray Decomposition Parallelization (RDP): The RDP splits up all the radiation rays into a number of subsets equal to the number of processors. Each processor only deals with one subset of rays. This approach may be implemented in different ways depending on how the subsets of radiation rays are selected. A better division of the rays can reduce the load imbalance, and achieve a better efficiency. Although the strategy of RDP fits well with the ray-tracing characteristic of DTM, it is not the best choice for a coupled CFD-radiation simulation because most parallel CFD codes use a spatial domain decomposition so that the information pertinent to the global domain is not available at the level of individual processors and significant data transfer is required in a distributed memory system. Yan [116] adopted the RDP strategy in a coupled CFD-DTM simulation. However in his study the code can only scale up to 8 processors.

Domain Decomposition Parallelization (DDP): In DDP, the spatial computational domain is decomposed into subdomains, and each of them is assigned

to one processor. The boundaries of a subdomain may be part of the original boundaries of the computational domain, or the interfaces between neighboring processors, which we call virtual boundaries. Radiative rays are fired inside the subdomain, both on actual boundaries and virtual boundaries, and they are traced locally by the assigned processor. The radiative intensities at the virtual boundaries are exchanged between adjacent subdomains and provide the boundary conditions for the ray-tracing algorithm. At the beginning of the simulation, the intensity at the virtual boundary is guessed, and as a result the whole simulation has to be iterative for a DDP-based parallel calculation.

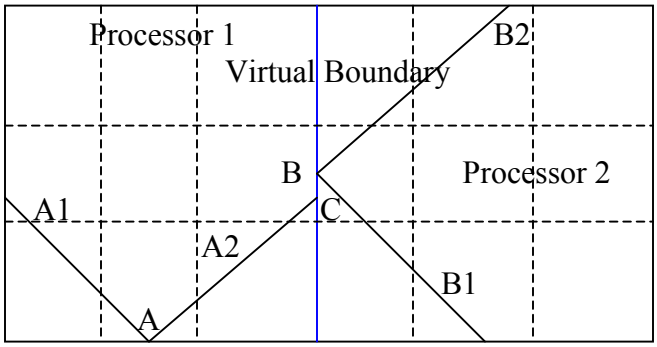

Figure 5-3. Illustration of a domain decomposition parallelization scheme.

Let us now use an example to illustrate the strategy of DDP. As shown in figure 5-4, the domain is divided into two subdomains. At each boundary point, two rays are fired ($N_\varphi = 2$, $N_\theta = 1$). In subdomain 1, A1 and A2 are two rays fired from point A; the other end of ray A2 is point C, which is located on a virtual boundary. In subdomain 2, B1 and B2 are two rays fired from point B, which is the center of one virtual boundary cell. C and B belong to the same boundary cell, but C is not at the center of the boundary cell. At the (n-1)th iteration, processor 2 integrates the RTE

along rays B1 and B2 to the virtual boundary point B. The radiation intensities at virtual boundary are saved in an array, hereafter referred to as the RIVB array. This array is transferred to processor 1 at the end of this iteration. At the n^{th} iteration, processor 1 integrates the RTE along ray A2 from point C to A. The boundary condition at C is retrieved from the RIVB array. An algorithm is needed to retrieve from the RIVB array the intensity corresponding to the same direction as ray A2.

Although it seems that DDP does not fit the ray-tracing characteristics of DTM as well as the RDP, it is nevertheless a natural choice for massive parallel CFD-radiation coupled simulations, since it involves much less data transfer between subdomains. The main drawback of DDP is the extra cost due to extra iteration operations. However, this extra computational request can be mitigated in a coupled CFD-radiation simulation, since a relatively good guess of initial radiative intensity on the virtual boundary is always available from the solution at the previous time step and therefore a smaller number of iterations is needed. In addition, in DDP, the directional discretization is actually finer than that in sequential DTM, because extra rays are fired at the subdomain interfaces (the virtual boundaries) besides the original rays from the computational domain boundaries. Therefore the previously mentioned "ray effect" can be reduced in DDP.

5.4. Implementation of Parallel DTM

A DDP-based parallel DTM radiation solver has been developed and implemented into S3D. The new subroutine is called DTM.f90 and is organized as follows:

1. Initialization: define the grid mesh, number of rays, parallelization topology, and convergence criterion etc.
2. Construct rays geometry information: loop over all the boundary cells in the subdomain, for each boundary cell perform the following operations:
    a. Define the incident rays according to the number of discretization for polar angles N_θ and azimuthal angles N_φ
    b. Loop over all the rays fired from this boundary point, for each ray perform the following operations:
        i. Compute $D_{j,i}$ using equation (5.10)
        ii. Find the location of the other end of the ray Q, calculate the number of control volumes the radiation ray passes, and allocate array for the geometry information accordingly
        iii. Trace the path of this ray, record the index of control volumes that the ray passes and beam length intersected by each control volume
3. Exchange the radiative intensity at virtual boundary (RIVB) between adjacent subdomains
4. Solve the RTE and compute the radiative source term and surface heat flux: Loop over all the boundary cells, for each boundary cell perform the following operations:
    a. Loop over all the rays fired from this boundary point, for each ray perform the following operations:
        i. Prepare the boundary condition at point Q using equation (5.11) or (5.12)

ii. Starting from Q, in each control volume integrate the RTE using equation (5.8) and compute the contribution to radiation source from this ray using equation (5.13), until the boundary point P is reached

b. Compute the incident surface radiative heat flux G using equation (5.9)

5. Check whether the convergence criterion is satisfied. If not, return to step 3. Otherwise stop the iteration, finish the radiation computation.

If the DTM is coupled with a flow field simulation, steps 1 and 2 should be done in the initialization phase of the CFD code while steps 3 to 5 are called every time the radiative power density distribution needs to be updated.

We treat here the participating medium as gray gas and use the concept of a Plank mean absorption coefficient. The emission and absorption of gas species CO_2, H_2O, CO and CH_4, as well as solid soot particles are considered in the radiation solver. The Planck mean absorption coefficient is written as:

$$\kappa = P_{CO2}K_{CO2} + P_{H2O}K_{H2O} + P_{CO}K_{CO} + P_{CH4}K_{CH4} + \kappa_{soot}, \tag{5.14}$$

where P_i is the partial pressure of species i. The species Plank mean absorption coefficients (K_i) are expressed as polynomial functions of temperature [107]:

$$K_i = \sum_{j=0}^{5} A_{ij} T^j, \; i = 1,4. \tag{5.15}$$

The coefficients A_{ij} are tabulated in table 5-1. The contribution of soot is modeled by:

$$\kappa_{soot} = 3.72 \frac{C_0}{C_2} f_v T = 700.0 f_v T, \tag{5.16}$$

$$C_0 = \frac{36\pi nk}{(n^2 - k^2 + 2)^2 + 4n^2k^2}, \tag{5.17}$$

where C_0 is a constant depending only on the soot refractive index n and absorptive index k; and $C_2 = 1.4388$ cmK is the second Plank function constant [110].

Emitting Species	A_{i0}	A_{i1}	A_{i2}
CH_4	10.17015	-7.947312e-3	4.342446e-7
CO	1.565360	1.483914e-2	-2.656035e-5
CO_2	32.44420	7.537513e-2	-1.535140e-4
H_2O	68.69480	-1.523490e-1	1.417848e-4
Emitting Species	A_{i3}	A_{i4}	A_{i5}
CH_4	1.048611e-9	-2.287861e-13	0
CO	1.687980e-8	-4.674473e-12	4.767887e-16
CO_2	9.487940e-8	-2.509259e-11	2.447995e-15
H_2O	-6.620996e-8	1.524150e-11	1.373456e-15

Table 5-1. Model coefficients for the temperature variations of Plank mean absorption coefficients of the emitting species in the temperature range 300-3000K [107].

5.5. Validation Tests for Parallel DTM Code

Test case 1. Radiative heat transfer in a duct with a Participating Medium:

We first consider radiative heat transfer in an infinitely long duct with a square cross-section (see figure 5-5). All four walls are cold and black. The duct contains a medium of constant absorption coefficient (κ) and constant temperature (T_g). We want to determine the radiative heat transfer flux received at the wall boundaries. The same problem has been used as a validation case in references [112, 114, 119].

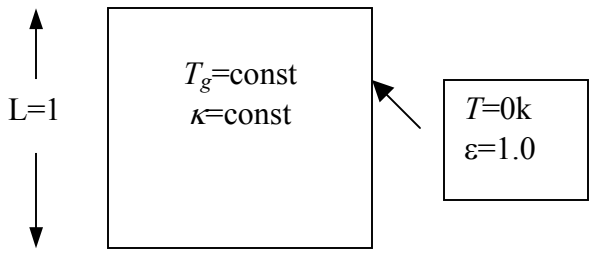

Figure 5-4. Illustration of the geometry of test case 1.

We use a two-dimensional mesh of 10×10. The angular discretization is N_φ=20 and N_θ=8. The nondimensional surface heat flux for three different optical thickness cases are plotted in figure 5-6. The results agree with the solution reported in [114]. And according to [112], the accuracy of DTM for this problem is better than that of DOM.

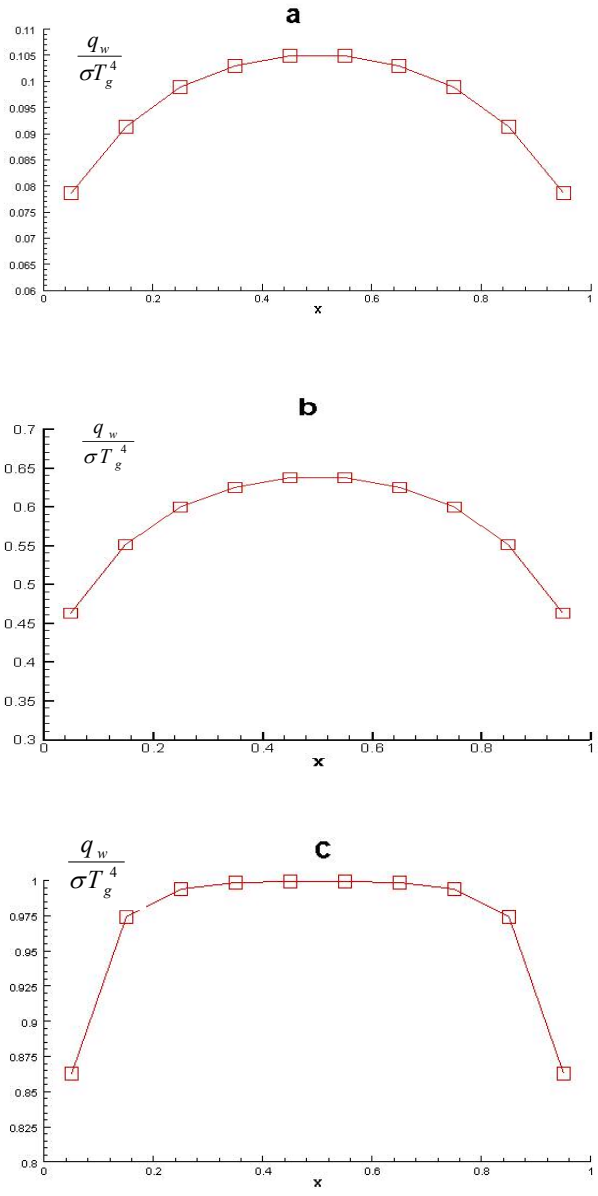

Figure 5-5. Test case 1: nondimensional wall radiative heat flux for three different optical thickness cases. (a) κL=0.1 (b) κL=1.0 (c) κL=10.0.

The results for multiple processors are presented below: Figure 5-7 shows the nondimensional heat flux received by the wall computed by DTM and using 1,2,4,9 processors. The grid mesh is 30×30, and N_φ=20, N_θ=8. The corresponding spatial distribution of radiation power density computed using single processor and four processors is showed in figure 5-8. Both plots in figure 5-8 show that our DTM solver provides almost identical result in sequential or parallel mode. In figure 5-8b, the slightly distort of the isocontour near the interfaces between two subdomains is due to the fact that the boundary condition retrieved from the RIVB array is not exact since the starting point of a ray might not locate at the boundary cell center. (See figure 5-4, the point C is not at the exact same location as the point B.) This error will be reduced if we use a finer computational mesh.

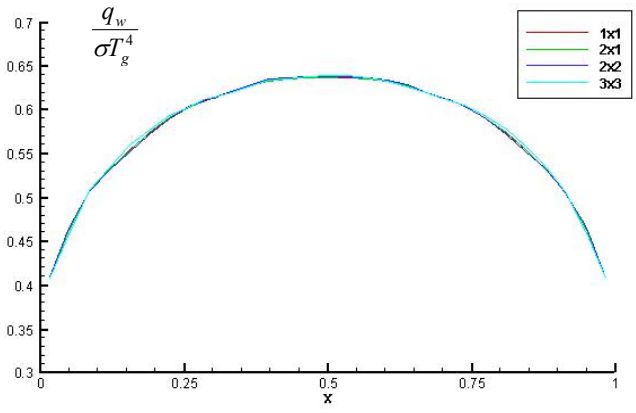

Figure 5-6. Test case 1: Nondimensional wall radiative heat flux calculated using different number of processors (1,2,4,9): κL=1.0.

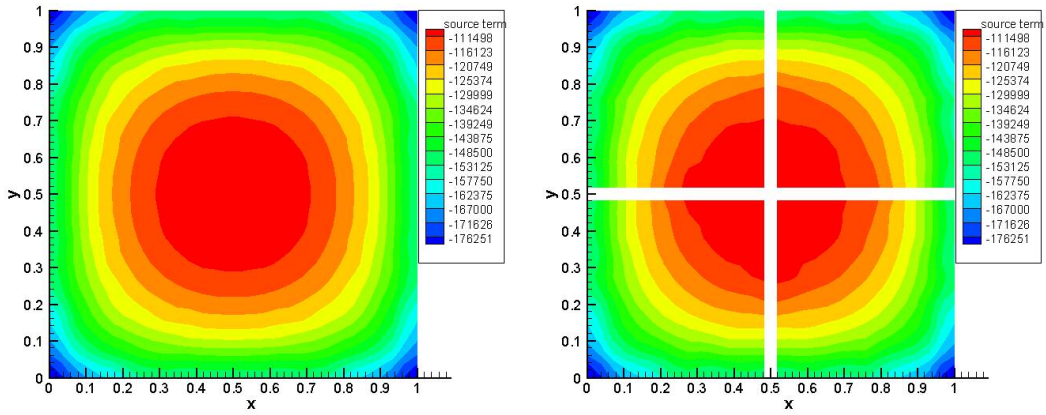

(a) (b)

Figure 5-7. Test case 1: Distribution of the radiative power density (w/m^3) calculated using different number of processors: T_g=1000k, κL=1.0. a) single processor b) four processors.

Test case 2. Two-dimensional laminar counterflow diffusion flame with radiative heat transfer:

The objective of this test is to integrate the new parallel DTM radiation solver into S3D, and evaluate the performance of the code. We consider a steady C_2H_4-O_2/N_2 counterflow diffusion flame. The configuration is similar to the test case in section 4.3. We use the same boundary conditions, chemical mechanism, soot model and strain rate. The only difference is that a larger computational domain (2.48 cm × 2.48 cm) and finer grid resolution (400 × 400) in the *y*-direction are adopted. We first compute a two-dimensional steady laminar flame without thermal radiation. Then we use the same code with the radiation solver turned on to describe radiative heat loss from the flame. In this test we take the DNS fields of temperature and species mass fraction, and use the radiation solver as a post-processor.

We first examine some numerical issues associated with the parallel DTM solver. As discussed in section 5.3, the parallel DTM solution needs an iterative

procedure. It is important to look at the convergence rate and determine a convergence criterion. Both the radiative heat flux measured at a boundary and the radiative power density distribution inside the computational domain can be used as indicators of convergence. Since the latter has a more direct influence on the CFD solution (through the energy equation), we consider the radiative power density in our convergence criterion. We measure the relative difference of the L2 norm of radiative power density between two consecutive iterations:

$$\varepsilon = \frac{\sum_{\text{CPUs}} \| \mathbf{S}^n - \mathbf{S}^{n-1} \|}{\sum_{\text{CPUs}} \| \mathbf{S}^n \|}, \tag{5.18}$$

where **S** represents the array of radiative power density, superscript n the iteration number, and L2 norm is defined by $\| \mathbf{S} \| = \sqrt{\sum s_{ij}^2}$. When ε is smaller than a tolerance value, we consider that the radiation iterative algorithm has converged. In figure 5-9, we present the evolution of ε as a function of the number of iterations. The results for both the first and second time step in the CFD simulation are presented. At the first time step, we use zero as the initial radiative intensity at the interfaces of the computational sub-domains; while at the subsequent time steps, we use the value from the previous time step and therefore the number of iterations required is reduced. From figure 5-9 we can read that, if we use 10^{-10} as the threshold of convergence, 23 and 18 iterations are required for the first and second time steps respectively. The question of what is the appropriate value for the threshold is still an open question, since ε is not a true measure of the error and a small value of ε might not be an indication of a converged solution. (For example, it might only indicate a slow convergence in some cases.) Figure 5-10 presents a similar ε-evolution curve as

shown in figure 5-9, however also plotted is an evolution of the total radiative power with the iteration number, which can be viewed as a better measure of the convergence rate. We can see that in this particular case the solution does not change and can be considered as converged after $\varepsilon < 10^{-6}$, or after about 17 iterations.

We now look at the scalability of the parallel DTM solver. The scalability of a parallel code is usually determined by the amount of communication between adjacent processors required in the algorithm. However for the domain decomposition parallelization (DDP) of DTM, the scalability also depends on the total number of iterations needed. The number of iterations increases with the increase in the number of processors, as shown in figure 5-11. Figure 5-12 presents the speed-up when changing the number of processors. The speed-up for 64 processors is about 16, four times lower than the ideal value. Note that the scalability results are compared for the first time step. Since the number of iterations decreases in the following time step, the real scalability for a fully coupled CFD simulation is supposed to be improved.

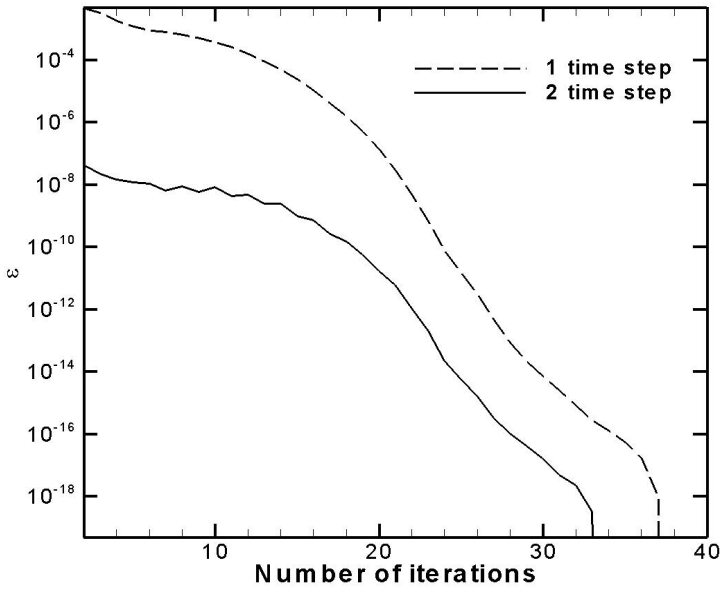

Figure 5-8. Convergence test. Results are obtained using 256 rays for DTM and 64 processors for parallel computations. The dashed curve is for the DTM computation at the first time step of the CFD simulation, and the solid curve is for the second time step.

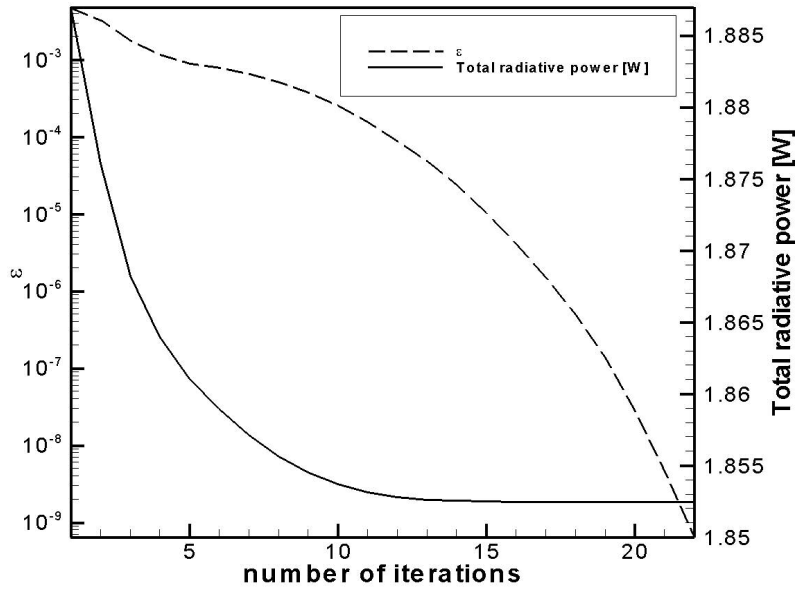

Figure 5-9. Convergence test. Results are obtained using 256 rays for DTM and 64 processors for parallel computations. The dashed curve: convergence criterion. The solid curve: total radiative heat loss.

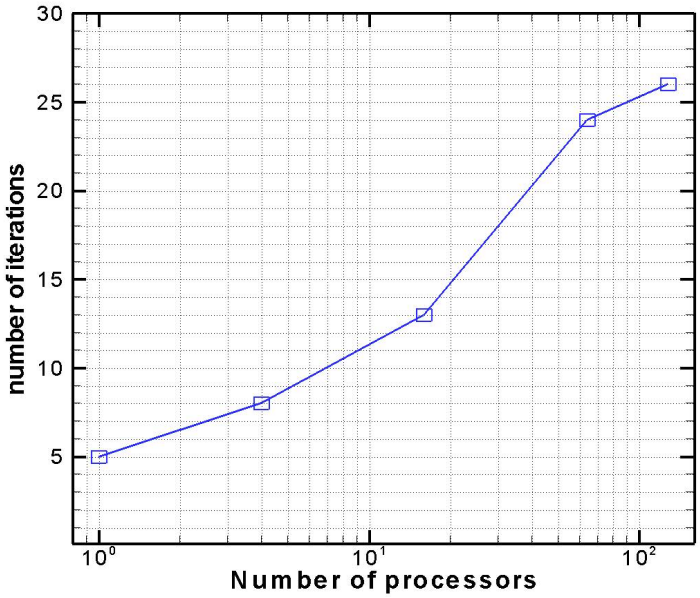

Figure 5-10. Number of iterations needed for DTM using different number of processors. Results shown are for the first time step. Number of rays per boundary cell: 256.

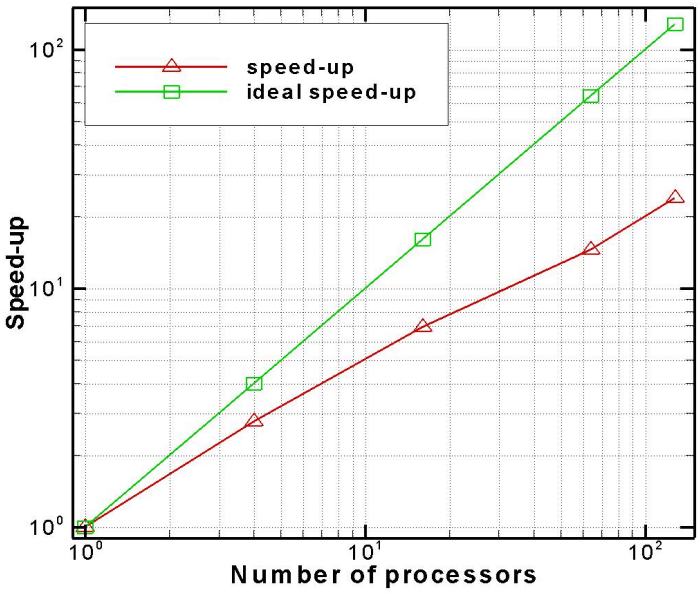

Figure 5-11. Scalability test for the DTM solver. Wall-clock time recorded is the time used for DTM solver for the first time step in a DTM-CFD coupled simulation.

We now turn to a study of the accuracy of DTM by comparing DTM with the discrete ordinates method (DOM) and the optically thin model (OTM). (The DOM solver is provided by our collaborators from the University of Michigan: Chunsang Yoo and Hong Im.) In OTM, the self-absorption is simply neglected and the radiative source term is computed as follows:

$$-\nabla \cdot \mathbf{q}_{\mathbf{r}} = -4\sigma\kappa(T^4 - T_\infty^4)\,. \tag{5.19}$$

The counterflow diffusion flame under the study is in the optically thin regime. To assess the DTM performance for different optical thickness cases, we arbitrarily manipulate the absorption coefficient and compare the results. Figure 5-13 presents the radiative power density along the flame normal direction, computed from OTM, DTM using 256 rays, and DOM using the S8 approximation. The results by DTM and DOM are almost identical to the prediction of OTM and show that the flame is indeed optically thin. Plotted in figure 5-14 are the results obtained with an arbitrarily modified optically thickness. In figure 5-14a, the plank mean absorption coefficient κ is arbitrarily multiplied by a factor of 10, whereas in figure 5-14b a factor of 100 is used. It is shown that for large optically thicknesses, the results from DTM and DOM are still comparable. Both methods predict a reduced radiative heat loss in the high temperature zone compared to the predictions by the emission-only model (OTM) and capture the preheating effect at both edges of the flame due to the radiation absorption. Figures 5-13 and 5-14 also indicate that DTM with 256 rays per boundary cell give similar results as DOM with a S8 approximation.

Figure 5-15 presents the results of a ray refinement test for DTM. The DTM results are again compared with DOM and OTM for three different optical

thicknesses. We use the volume integrated radiative power as a representative output of the radiation solver. From figures 5-15(a) (c) and (e), we can see that the results show a trend of convergence when the number of rays is increased for all three optical thickness cases. For the optically thin case (figure 5-15a) using a small number of rays (36 and 64), the DTM prediction of the total radiative loss is larger than that of OTM. It indicates that when absorption is not important, the error introduced by under-resolved DTM might overwhelm the absorption effect, and therefore using OTM for this case might be a better choice. In general DTM with 256 rays provides comparable results with DOM-S8 approximation for different values f the optical thickness. The total radiative heat loss only provides a volume-integrated global measurement of the radiative power density. In figures 5-15(b) (d) and (f), we take an alternative approach to look at the local error of each computation. To evaluate the error, we need an "exact" value. Here we suppose that DTM with 900 rays (per boundary cell) is accurate enough to serve as the reference "exact" value. The error is measured as follows:

$$\varepsilon = \frac{\| \mathbf{S} - \mathbf{S}_{exact} \|}{\| \mathbf{S}_{exact} \|}, \tag{5.20}$$

and is presented in Figures 5-15(b) (d) and (f). The figures show that with the increase in the optical thickness, the errors of OTM are dramatically increased as we expect. The error of DOM is sensitive to the optical thickness, especially for the S2 approximation. The convergence rate for DTM with various rays is relatively insensitive to the optically thickness. It appears that for the optically thin case, DTM with 256 rays provide a similar level of accuracy as DOM with the S8 approximation, while for the optically thick case, DTM with 100 rays is comparable with the DOM-

S8 method. It is worth noting that the accuracy of the DTM or DOM predictions also depends on the spatial resolution. Therefore the comparison presented for DTM and DOM are specific to this test problem and cannot be extended directly to a general configuration. However the above ray refinement tests are valuable for us to make a more informed decision on the number of rays we should use for a specific problem.

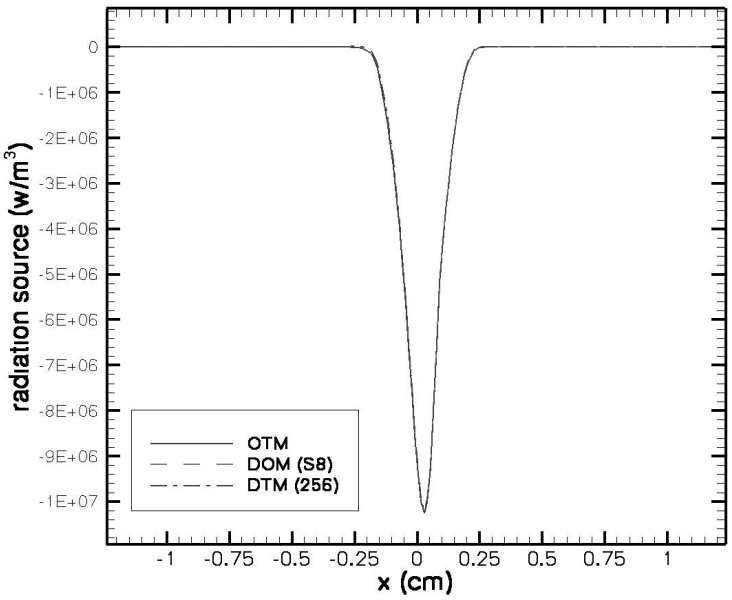

Figure 5-12. Test case 2: Spatial variations of the radiative power density normal to the flame. Comparison between DTM, DOM, and the optically thin model.

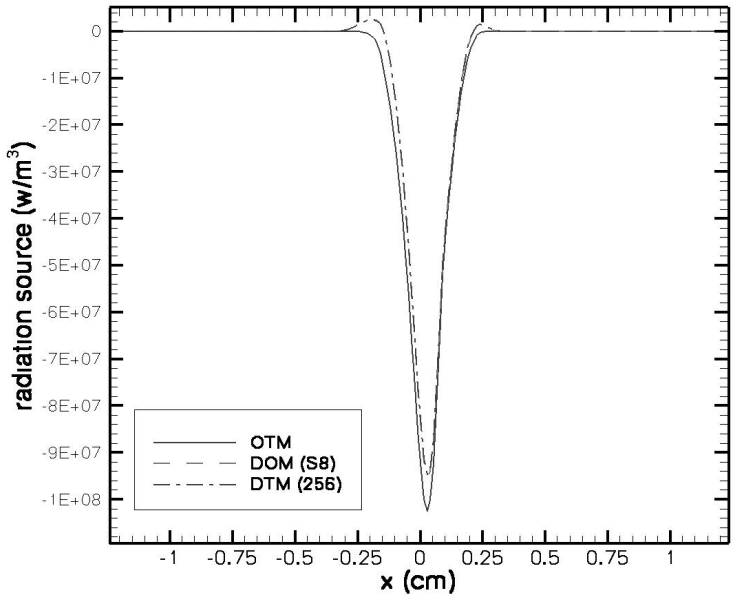

(a)

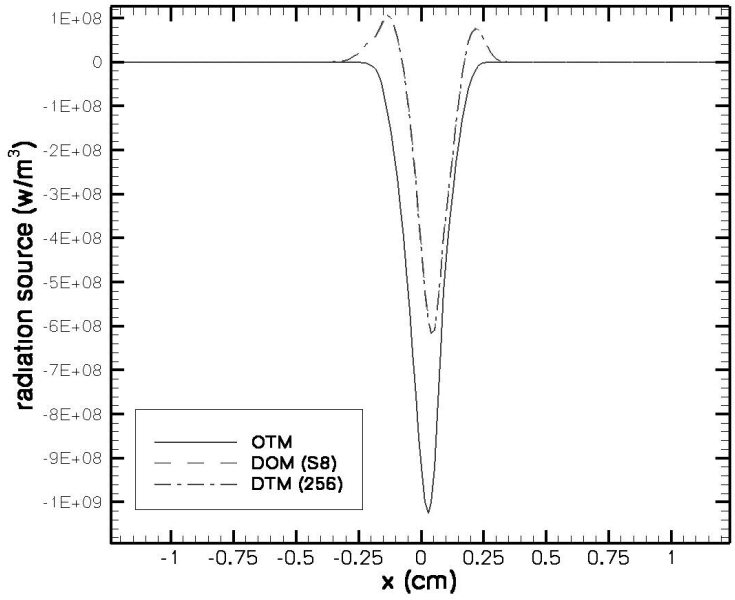

(b)

Figure 5-13. See the caption of figure 5-9. The plank mean absorption coefficient κ is modified to achieve a different optical thickness. (a): κ is increased to 10 times the original value. (b): κ is increased to 100 times the original value.

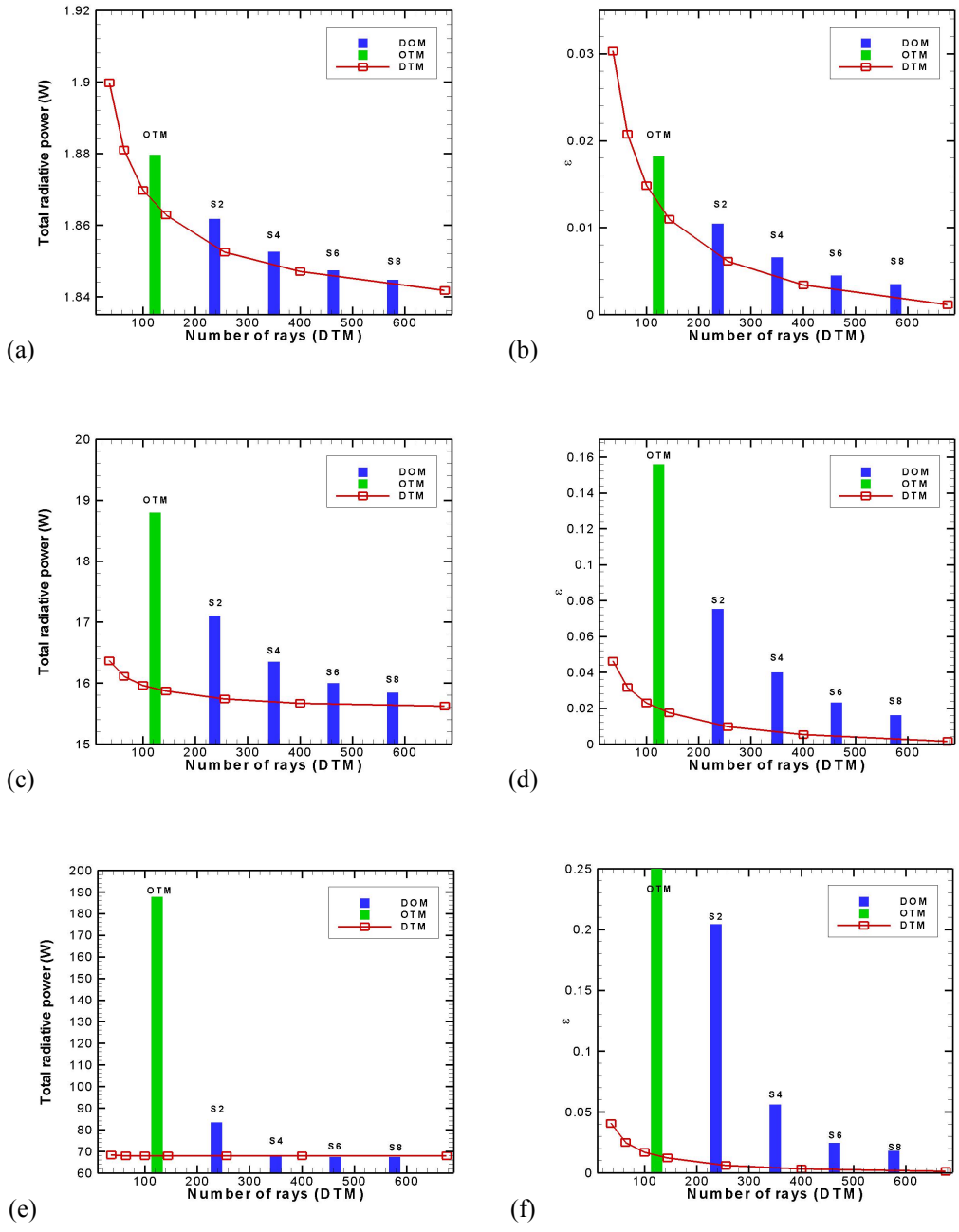

Figure 5-14. Ray refinement test for DTM. Data are also compared with OTM and DOM (S2-S8 approximation). Numbers of rays used for DTM are 6×6, 8×8, 10×10, 12×12, 16×16, 20×20 and 26×26. First row ((a) and (b)): using the true value of κ. Second row ((c) and (d)): κ is increased 10 times. Third row ((e) and (f)): κ is increased 100 times. Figures in the left column ((a), (c) and (e)): volume integrated radiative power. Figures in the right column ((b), (d) and (f)): relative error compared with the results computed by DTM with 900 rays.

5.6. Coupled Radiation-CFD Simulations

We now turn to a coupled radiation-CFD simulation. We consider an unsteady process corresponding to an initially steady C_2H_4-O_2/N_2 diffusion flame interacting with two pairs of vortices. The initial steady laminar flame has been described in the previous section. Two pairs of counter-rotating vortices are superimposed in the velocity field, one on the fuel side and the other on the oxidizer side. The vortex pairs are subsequently convected to the flame by the mean flow and their self-induced velocity, thereby penetrating through the flame with vigorous interaction until the vortices are convected away. We compare DTM with OTM in this unsteady optically thin flame. The simulations are performed with 64 processors on an IBM Power 3 system operated by the National Energy Research Scientific Computing Center (NERSC). For the DTM simulation, we use 256 rays (per boundary cell) and the convergence threshold is 10^{-6}. The time step is controlled by the CFL condition and set constant at $\Delta t = 10^{-7}$ sec. Since the time step is controlled now by acoustic motion, we need not update the thermal radiation field every time step. In this simulation, we choose to call the DTM solver once every 10 flow time steps. In the OTM simulation, since the CPU time used for thermal radiation is negligible, we call the radiation solver at every time step.

Figure 5-16 shows the snapshots of temperature and vorticity iso-contour at t = 0, 3, 5, and 15 msec. The flame is initially a steady plane diffusion flame. The interactions with the vortices make the flame at the center highly stained. As vortices are convected away, the highly stretched flame relaxes to its original shape. Figures 5-17a and 5-17b present the temporal variations of the total heat release rate and

radiative fraction respectively. The high stretch induced by the vortices increases heat release and reduces the radiative heat loss. In figure 5-18, we compare the total radiative heat loss computed by DTM and OTM. Both DTM and DOM produce similar results: the radiative heat loss decreases when the flame is stretched and increase when the steady diffusion flame is restored. The prediction of the total radiative heat loss by DTM is about 1.5% lower than that by DOM. Since the flame is optically thin and the radiative fraction is so small, this difference in the thermal radiation fields does not have a significant impact on the flame structure and dynamics.

Both simulations are run for 150,000 time steps. The wall-clock time for OTM is approximately 24 hours, while DTM takes 37 hours. The overhead introduced by DTM is therefore about 54%.

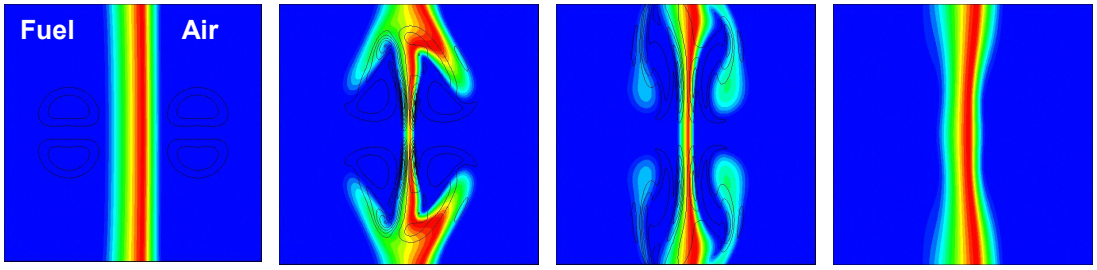

Figure 5-15. Snapshots of temperature (flood) and vorticity (black lines) isocontour for four consequent time instants. From left to right, t = 0, 3, 5, and 15 msec.

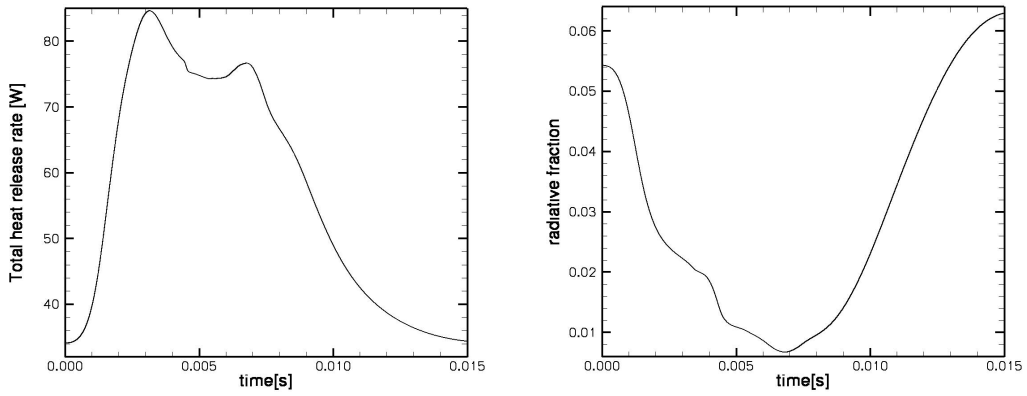

(a) (b)

Figure 5-16. Temporal variations of (a) the total heat release rate, and (b) radiative fraction.

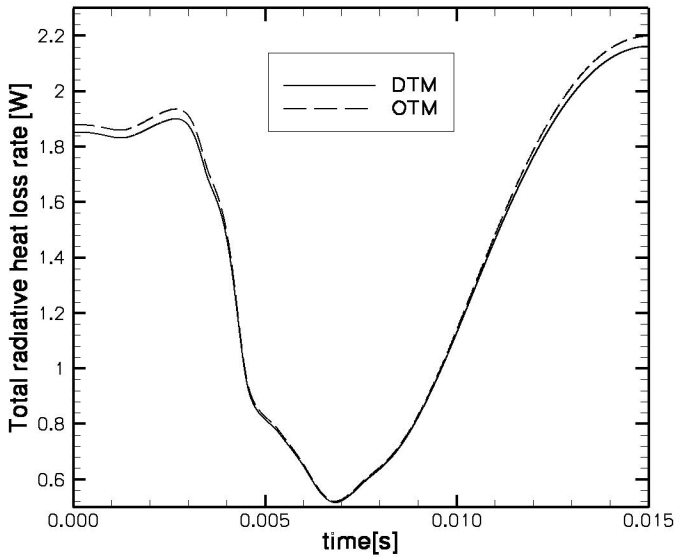

Figure 5-17. Comparison of the time variation of the total heat release rate between DTM and OTM.

5.7. Concluding remarks

We have developed a parallel thermal radiation model based on the discrete transfer method (DTM). The parallel strategy is chosen to be consistent with our CFD code S3D. The thermal radiation model has been validated using simple test cases as a stand-alone solver. Finally a fully coupled radiation-CFD simulation is performed

for a transient problem corresponding to a diffusion flame-vortex interaction. Compared with the optically thin model (OTM), the current thermal radiation model takes the gas absorption into account, and therefore is more accurate for optically thick cases. The penalty associated with the increased accuracy is the significant overhead in computational cost. It is also worth noting that the current model treats the combustion mixture as gray gases. It is possible to extend the current solver to a spectrally-resolved model, but the computational cost and complexity will be increased considerably.

Chapter 6: DNS of Non-Premixed Flame-Wall Interactions

6.1. Introduction

Flame-wall interactions (FWI) play an important role in many combustion systems. For instance in Internal Combustion (IC) engines, cooled walls combined with occurrences of short flame-wall distances result in flame quenching and FWI has a negative impact on engine performance, both in terms of thermal efficiency and pollution propensity. While the magnitude of the FWI impact on thermal efficiency remains small in IC engines, FWI has a more notable effect on pollutants emissions and provides one of the dominant mechanisms for unburnt hydrocarbon emissions. Similar effects are observed in aeronautical propulsion and power-generation applications, especially given the recent trends towards the design of more compact, smaller (meso- or micro-scale) combustion chambers; the associated higher surface-to-volume ratios and shorter flame-wall distances result in a larger impact of flame-wall interactions and heat transfer on the combustion system performance. Enclosure fires are another combustion topic in which FWI plays an important (albeit different) role. For instance, the burning of a vertical flammable wall is a generic configuration where the fuel is released and consumed within the buoyancy-driven wall boundary layer, and the entire combustion process may be considered as FWI.

The subject of flame-wall interactions in IC engines has received significant interest in the past fifteen years. Previous studies have focused primarily on the quenching problem of laminar or turbulent premixed flames near cold wall boundaries[16, 126-135]. Results from laminar flame experiments [126, 127] indicate

that: (1) quenching events occur near cold wall surfaces; (2) these quenching events also correspond to maximum values of the gas-solid heat flux; (3) depending on wall temperature and fuel type, premixed flames may loose a significant fraction of their reference power when driven to quenching. The maximum heat flux may be as high as 0.5-1 MW/m^2 for atmospheric hydrocarbon flames, or approximately 30% of the flame reference power; the reference power is defined as the heat release rate per unit flame surface area and is typically of the order of 1-3 MW/m^2 for stoichiometric flames at atmospheric pressure.

Detailed numerical modeling has been used in recent years both to reproduce the early experimental findings of [126, 127], and to bring further insights into the controlling factors that determine flame-wall heat transfer in IC engines. Numerical modeling has been used in particular to study the effects of turbulent flow conditions [16, 128, 132, 133], detailed gas-phase chemical kinetics [130, 131, 134-136] and heterogeneous gas-solid surface chemistry [130, 134, 135]. Note that in the treatment of this problem, the flames are always assumed to be optically-thin and thermal radiation is neglected. Consistent with the laminar flamelet viewpoint, the dynamics of quenching events in turbulent flames were found to be similar to those observed in laminar flame studies: for instance, the magnitude of the peak gas-solid heat flux was approximately the same in laminar or turbulent flame simulations [16, 128]. Furthermore, while numerical modeling based on simplified (single-step) chemistry was found to correctly describe FWI when the wall temperature is low, detailed descriptions of homogeneous/heterogeneous chemical reactions were required for accurate predictions of the gas-solid heat flux when the wall temperature is above 400

K [130, 131]. These results combine to draw a complex picture of FWI in which flame quenching is both thermally- and kinetically-driven.

References [136, 137] also consider the case of a laminar diffusion flame impinging on a cold wall in a stagnation point flow configuration. Reference [137] considers the general case of hydrocarbon-air flames whereas reference [136] focuses on the more specific case of hydrogen-oxygen flames. In the impinging flow/diffusion flame configuration, FWI is a transient process that must result in flame quenching at the wall; however, details of the flame quenching process depend strongly on the flow strain rate, which is specified as a free parameter. It is found that at high strain rates, the diffusion flame comes remarkably close to the wall surface (prior to quenching) and the gas-solid heat flux takes very large values (for the hydrocarbon-air flames studied in [137], the peak value of the gas-solid heat flux may be higher than that obtained in the corresponding premixed stoichiometric configuration). In [137], the results are provided in non-dimensional units with laminar premixed flame parameters selected as reference values. In these units, the minimum flame-wall distance is of the order of (D_{th}/s_L) where D_{th} is a reference thermal diffusivity and s_L the stoichiometric laminar flame speed; the applied strain rate takes values up to (s_L^2/ D_{th}). It is worth noting that these flame conditions may appear somewhat unrealistic: using representative values of $D_{th} = 2.2\times10^{-5}$ m^2/s and s_L = 0.5 m/s, one finds that flames are strained up to more than 10,000 s^{-1}, and the flame-wall distance is decreased to less than 50 μm. The large values of the gas-solid heat flux that are obtained under those conditions may be an artifact of using excessive values of strain rate and of the specifics of the transient stagnation point

flow configuration. The question of whether these flame-flow conditions are representative of practical turbulent combustion configurations remains entirely open.

We now turn to enclosure fire applications and consider three different configurations featuring substantial flame-wall interactions [138, 139]: a first configuration corresponding to a flammable vertical wall, in which the flame is fueled by the thermal decomposition of the wall material; a second configuration in which the flame is fueled by a separate burner and where it develops adjacent to an inert vertical wall; and a third configuration in which the flame is again fueled by a separate burner and impinges on an inert horizontal (ceiling) wall. These configurations are representative of the large variety of flame spread and heat transfer mechanisms found in fire problems and correspond to different flame-wall arrangements. In the first configuration, the flame size is determined by the details of the gas-solid heat transfer and in-wall fuel gasification processes, whereas in the second and third configurations, the flame size is arbitrary and simply prescribed by the power output of the pilot burner. Typical values for the wall heat flux are: up to 50 kW/m^2 in the case of vertical wall fires [138-141]; up to 120 kW/m^2 in the case of vertical walls exposed to a separate adjacent flame [138, 139, 142, 143]; and up to 150 kW/m^2 in the case of horizontal (ceiling) walls exposed to an impinging, buoyancy-driven flame [138, 139, 144, 145]. It is worth emphasizing that those estimates correspond to time-averaged values and cannot be compared directly to the time-resolved, instantaneous peak values discussed above in the context of IC engine applications. The statistical variations of flame-wall distances and gas-solid heat fluxes remain unknown in fire problems; these statistical variations will depend on

the strength of the buoyancy-driven turbulent motions. The magnitude of the wall heat flux will also depend on the optical thickness of the flame gases: previous studies indicate for instance that while the gas-solid heat flux in small non-sooty flames is controlled by convective heat transfer, the contribution of radiation heat transfer becomes dominant in large flames with significant smoke production [138, 139].

The present study is a continuation of the laminar non-premixed FWI study in [137] and an extension to the case of turbulent flame-wall interactions. The questions of turbulent fuel-air-temperature mixing, flame extinction and wall surface heat transfer are studied using direct numerical simulation (DNS) in a configuration corresponding to an ethylene-air diffusion flame stabilized in the near-wall region of a chemically-inert solid surface. While viewed as a questionable simplification, thermal radiation is neglected in the present simulations (it will be considered in a follow-up study). Our objective here is to focus on turbulent flow effects, and to evaluate in particular the wall-induced modifications of the flame structure, the probability of flame extinction events and the statistical distribution of the wall surface heat flux. The numerical configurations are presented in the next section; results from simulations are discussed afterward.

6.2. Numerical Configuration

The selected flame configuration corresponds to ethylene burning in ambient air. While S3D features a detailed chemical kinetics capability as well as new soot formation and thermal radiation capabilities, the present study takes an intermediate step and focuses on flame-wall interactions without soot and radiation. In addition, combustion is here described using a single-step model proposed in reference [100]:

$$\left.\begin{aligned} & C_2H_4 + 3O_2 \rightarrow 2CO_2 + 2H_2O, \\ & \dot{\omega}_{C_2H_4} = -\frac{A}{(10^6)^{p+q}} \times M_{C_2H_4} \left(\frac{\rho Y_{C_2H_4}}{M_{C_2H_4}}\right)^p \left(\frac{\rho Y_{O_2}}{M_{O_2}}\right)^q \exp(-T_a / T), \end{aligned}\right\} \tag{6.1}$$

where $\dot{\omega}_{C_2H_4}$ is the fuel mass reaction rate (in units of kg/m^3/s); A a model coefficient, $A = 2.0\times10^{+12}$ (mol/m^3) $^{(1\text{-}p\text{-}q)}$s^{-1}; p and q the model fuel and oxygen concentration exponents, $p = 0.1$, $q = 1.65$; ρ the mixture mass density (kg/m^3); Y_k the species k mass fraction; M_k the species k molecular weight (kg/mol); T_a a model activation temperature, $T_a = 15107$ K; and T the fluid temperature (K). The corresponding heat release rate is:

$$\dot{q}_c = (-\dot{\omega}_{C_2H_4})\Delta H_c, \tag{6.2}$$

where $\dot{q}_c$ is the flame power density (in units of W/ m^3); and ΔH_c the heat of combustion (J per kg of fuel consumed). Note that the present single-step chemistry version of S3D also assumes a constant heat capacity, $c_p \approx 1006$ J/kg-K, and that the value of ΔH_c has been accordingly adjusted so that the simulated adiabatic flame temperature is 2370 K: we use $\Delta H_c = 32.7$ MJ/kg.

Additional flame modeling choices include a temperature-dependent dynamic viscosity (μ varies with T to the power 0.7), a constant Prandtl number, $Pr = 0.708$, and unity Lewis numbers.

We now turn to a brief discussion of the anticipated impact of our flame modeling choices. The accuracy of the simplified chemical kinetics and molecular transport sub-models adopted in S3D has been evaluated in a separate numerical study of strained laminar diffusion flames. This separate study considers the generic case of steady, one-dimensional, plane, counter-flow flames. To evaluate accuracy,

the S3D-based simulations are compared to more elaborate calculations performed with the OPPDIF software [58], using detailed descriptions of chemistry and molecular transport [146]. In a simple laminar counter-flow flame configuration, discrepancies between S3D and OPPDIF predictions are essentially due to differences in the mathematical formulation of the flame problem, and may therefore be used to evaluate the penalty associated with using simplified chemical and molecular transport models.

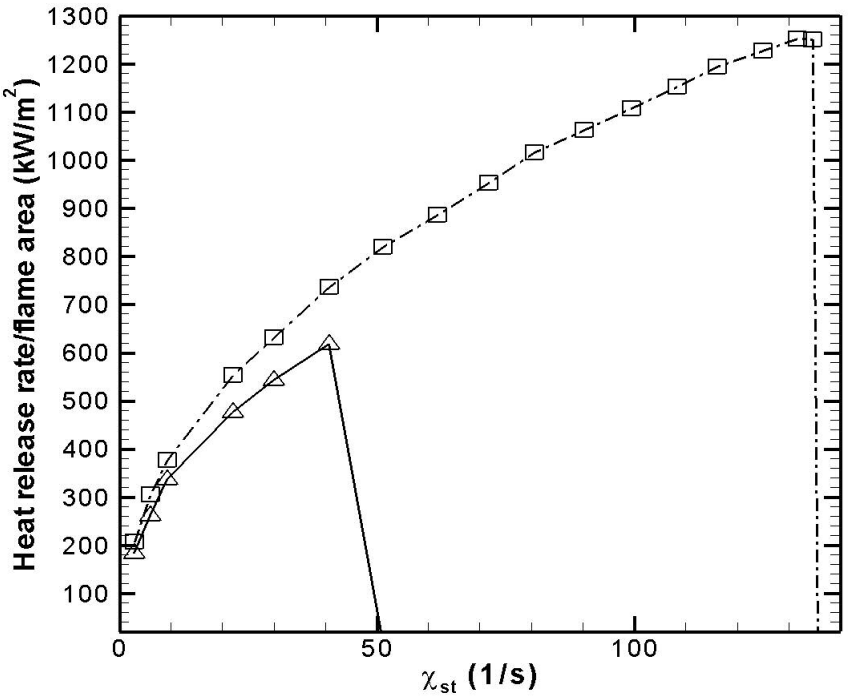

Figure 6-1. Flame response to changes in the fuel-air mixing rate in a steady, one-dimensional, plane, laminar, diffusion counter-flow flame configuration. The top curve (squares) corresponds to numerical data obtained with OPPDIF using detailed chemistry [146] and molecular transport; the bottom curve (triangles) corresponds to numerical data obtained with S3D and using single-step chemistry (equations (6-1)-(6-2)) and unity Lewis numbers.

Figure 6-1 presents typical results obtained from the S3D/OPPDIF comparative study. Each data point in figure 6-1 corresponds to a converged steady

flame solution. The plot corresponds to variations of centerline combustion intensity with fuel-air mixing rate; the combustion intensity is measured as the heat release rate per unit surface area; the fuel-air mixing rate is measured as the stoichiometric value χ_{st} of the scalar dissipation rate χ, $\chi = 2D|\nabla Z|^2$, with D the heat diffusivity and Z the fuel-air-based mixture fraction. The inverse of χ_{st} provides an estimate of the mixing time scale in the vicinity of the reaction zone [22, 54, 147]. The S3D and OPPDIF curves in figure 6-1 display the classical flame response to increasing mixing rates, including the intensification of combustion, observed for low-to-moderate values of χ_{st}, and the abrupt fall off, observed at high values of χ_{st}. This fall off corresponds to transition to the super-critical, flame extinction regime. Compared to OPPDIF results, it is seen that the S3D calculations underestimate the combustion intensity in the sub-critical regime, and predict extinction for a critical value of the scalar dissipation rate that is about three times smaller than that obtained with OPPDIF, $\chi_{st,ext}^{ad} \approx 45\,\mathrm{s}^{-1}$ where $\chi_{st,ext}^{ad}$ denotes the critical value of χ_{st} obtained at (adiabatic) extinction conditions.

While the errors documented in figure 6-1 are clearly a concern, we choose to accept these errors in the present study and to work with the simplified flame model described in equations (6-1)-(6-2). It is worth emphasizing, however, that the present DNS results are to be interpreted in a qualitative, rather than a quantitative manner. The pre-computed database of strained laminar diffusion flames is used in the following to help specify inflow boundary conditions, as well as to provide a point of reference in the analysis of the more complex flame structures observed under turbulent flow and non-adiabatic combustion conditions.

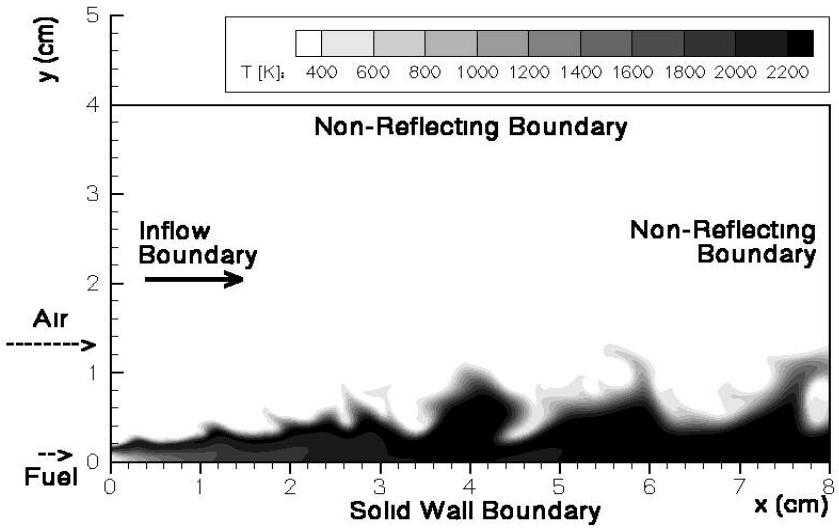

Figure 6-2. Numerical configuration corresponding to a turbulent ethylene-air diffusion flame stabilized near a solid wall. The computational domain is two-dimensional and features a turbulent inflow boundary at $x = 0$ (flow is from left to right); a solid wall boundary at $y = 0$; and non-reflecting boundaries at $x = 8$ cm and $y = 4$ cm. The turbulent inflow boundary is used both for air and fuel injection. The plot shows a typical snapshot of temperature iso-contours and is taken from a simulation in which the wall is assumed adiabatic.

Next, we turn to a presentation of the FWI numerical configuration. The FWI configuration corresponds to a two-dimensional, momentum-driven, chemically reacting, ethylene-air, mixing layer developing parallel to an inert solid wall surface (figure 6-2). The combustion region is well-ventilated with plenty of air supplied from the free stream while ethylene flow is confined to the near-wall region. As shown in figure 6-1, the computational domain features an inflow boundary at $x = 0$, a wall boundary at $y = 0$, and two non-reflecting boundaries, at $x = 8$ cm and $y = 4$ cm. The wall boundary conditions correspond to zero velocity, zero mass flux, and either zero heat flux (adiabatic wall case) or prescribed temperature (non-adiabatic wall case). The inflow boundary conditions at $x = 0$ correspond to prescribed velocity,

mixture composition and temperature. We now discuss those inflow conditions in more detail.

The free stream region of the inflow boundary corresponds to a uniform flow of air at normal temperature and pressure conditions, and seeded with turbulent-like perturbations. The mean velocity is u_∞ = 5 m/s; the perturbations use a variant of the random fluctuation method of reference [78], in which the velocity fluctuations are specified using an auxiliary synthetic field corresponding to homogeneous isotropic turbulence and a prescribed model kinetic energy spectrum. In the present study, the turbulent inflow perturbations are characterized by a moderate-to-high forcing intensity, $1 \leq u' \leq 2.5$ m/s, and a small integral length scale, l_t = 0.17 cm; the corresponding turbulent flow Reynolds number, ($\mathrm{Re}_t = (u' \times l_t / \nu)$, where ν is the free stream kinematic viscosity,) ranges from 108 to 270.

The near-wall region of the inflow boundary corresponds to a prescribed velocity profile that satisfies the no-slip wall condition and has a certain thickness δ: we choose δ = 0.15 cm. δ is also the selected inlet flame-to-wall distance, with fuel being injected at y-locations below δ, *i.e.* within the velocity boundary layer. Flow temperature and species mass fractions are specified at x = 0 using a separate calculation corresponding to a low-strain laminar counter-flow flame solution (see the discussion of figure 6-1 above).

The initial fields correspond to a one-dimensional laminar flame solution and are constructed from the inflow boundary profiles. The computational grid size is 1216 × 244. The grid spacing is uniform in the x-direction, $\Delta x \approx 66$ μm, while variable in the y-direction: the y-grid is uniform in the near wall/flame region, $\Delta y \approx 50$

μm for $0 \le y \le 0.8$ cm, and is stretched in the free-stream region. The grid resolution is chosen based on the above-mentioned laminar counterflow diffusion flame simulations, and in order to resolve the thin flame front of the highly strained laminar flame up to the extinction strain rate. Time integration is performed at a pace determined by the acoustic-based Courant-Friedrichs-Lewy stability condition, $\Delta t \approx$ 0.05 μs. The time step determined by the viscous Fourier condition is about one order of magnitude larger. However, the results obtained in the present study were produced without any special treatment for acoustic stiffness. Preliminary tests to use the newly developed ASR method in this flame configuration are in progress. Computations are performed for a total duration corresponding typically to 3 or 4 free stream transit times τ_∞, where $\tau_\infty = (L_x / u_\infty) = 16$ ms, with L_x the x-size of the computational domain, $L_x = 8$ cm. If we ignore the initial transient phase of duration equal to 1 or 2 free stream transit times, the useful part of the simulations lasts for approximately $t_s \approx 2 \times \tau_\infty = 32$ ms. This duration is sufficient to make observations of flame topology and structure near the wall boundary, however it is not long enough to obtain converged statistical information. Therefore we do not present time-averaged flow field information in the present study.

S3D is run in a parallel mode, using MPI and one of the following two super-computers: 256 processors on an IBM Power 3 system operated by the National Energy Research Scientific Computing Center (NERSC) at Lawrence Berkeley Laboratory; or 32 processors on an IBM Power 4 system operated by the National Center for Computational Sciences (CCS) at Oak Ridge National Laboratory. On

these platforms, the cost of performing a single simulation of total duration 64 ms is approximately 32,000 processor hours at NERSC and 7,100 processor hours at CCS.

6.3. DNS Results

Wall-Flame Structure

We consider in the following a series of four simulations: the simulations differ by the choice of inflow turbulence intensity and/or thermal boundary condition applied at the solid wall surface (see table 6-1). The flame geometries observed in cases 1-4 are found to correspond to different topologies and belong to one the following three categories: a continuous flame sheet without extinction; multiple flame sheets without extinction; or multiple flame sheets with extinction. Figures 6-3, 6-4, 6-5 provide examples of these three different categories.

Case	**1**	**2**	**3**	**4**
Turbulence intensity	u' = 1 m/s	u' = 2.5 m/s	u' = 1 m/s	u' = 2.5 m/s
Wall thermal boundary condition	adiabatic	adiabatic	Isothermal (T_w = 300 K)[(a)]	Isothermal (T_w = 300 K)[(a)]

[(a)] T_w is the gas-solid wall temperature

Table 6-1. Inflow turbulence intensity and wall thermal boundary condition used in cases 1-4 of the DNS database.

Figures 6-3(a)-(b) present instantaneous snapshots of temperature and fuel mass reaction rate, as obtained in case 1 (adiabatic wall, lower turbulence intensity). The figures illustrate the flame response to incoming flow perturbations and confirm that significant turbulent mixing and flame wrinkling take place in the vicinity of the

wall. They also show that the x-domain size is smaller than the wall-flame length and burning is observed to continue beyond the outflow boundary at x = 8 cm. Figure 6-3(c) presents the location of the stoichiometric fuel-air interface and a comparison between figures 6-3(b) and 6-3(c) indicates that the flame is active along the entire stoichiometric interface: the flame displays the classical downstream weakening of combustion intensity as the reactants get depleted and replaced by combustion products, but it remains free of any aerodynamic flame extinction event. In the absence of extinction, the temperature levels are particularly high in the near-wall region (see figure 6-3(a)): the wall boundary is almost everywhere in contact with hot gases at temperatures in excess of 2000 K.

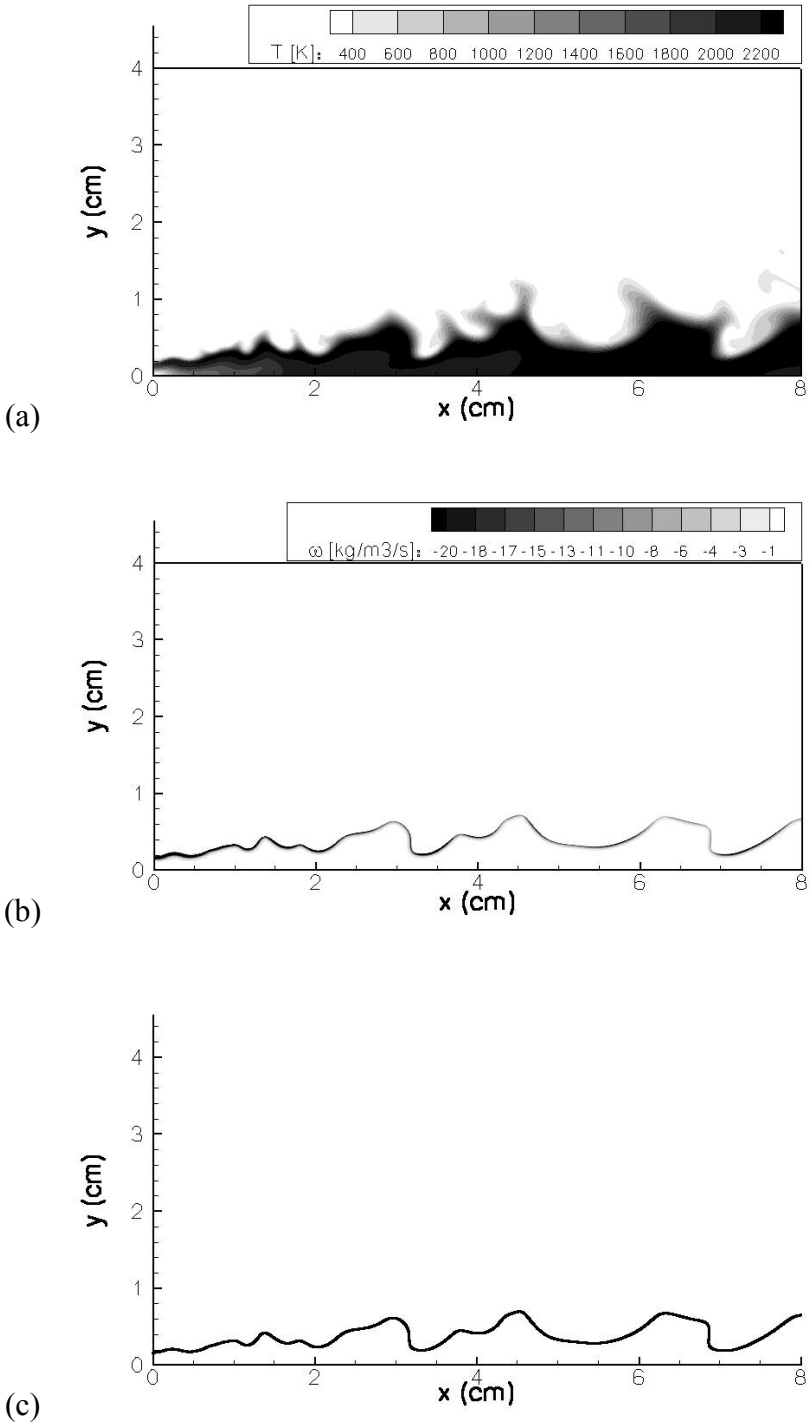

Figure 6-3. Instantaneous spatial variations of: (a) fluid temperature (in units of *K*); (b) fuel mass reaction rate (in units of kg/m^3/s). Figure (c) presents the location of the corresponding stoichiometric iso-contour of the fuel-air-based mixture fraction *Z*. Case 1 solution.

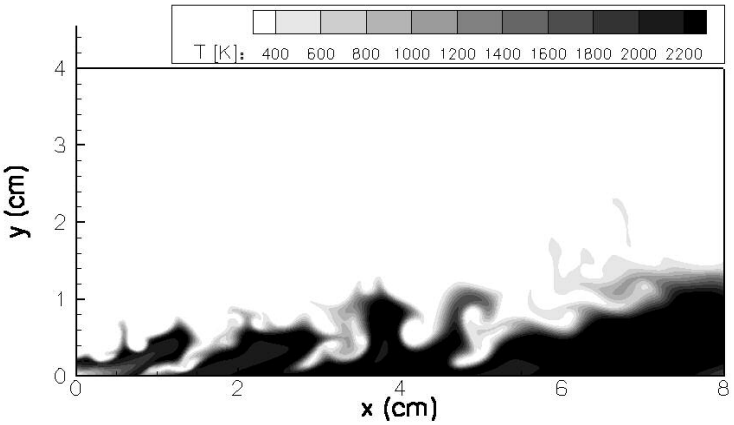

(a)

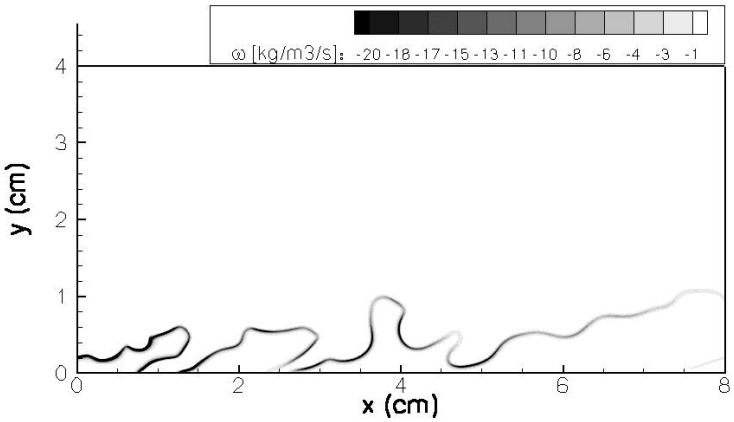

(b)

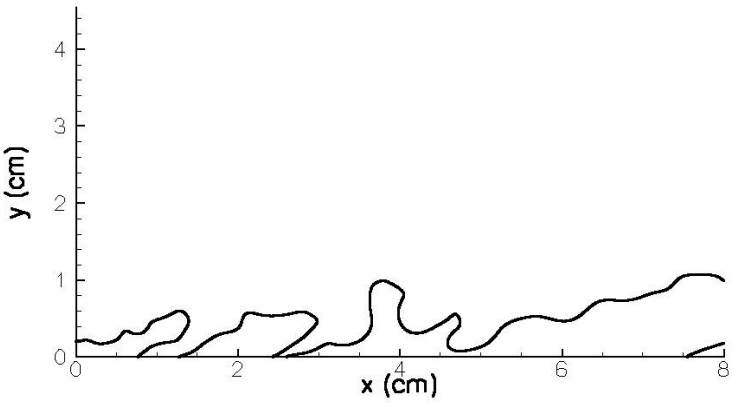

(c)

Figure 6-4. see caption of figure 6-3. Case 2 solution.

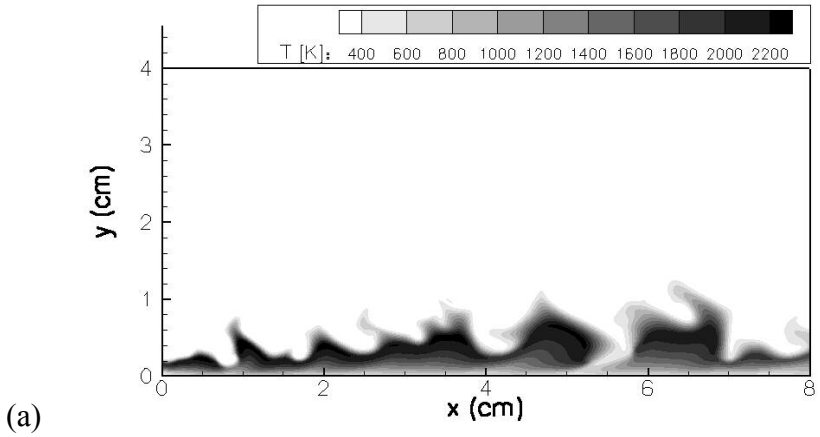

(a)

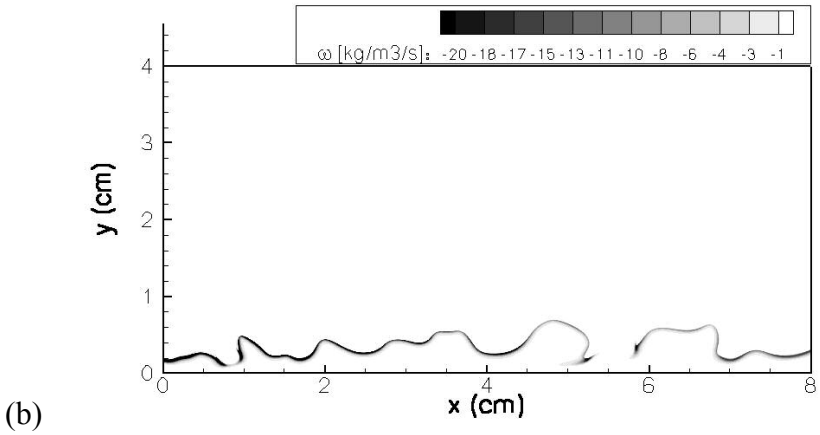

(b)

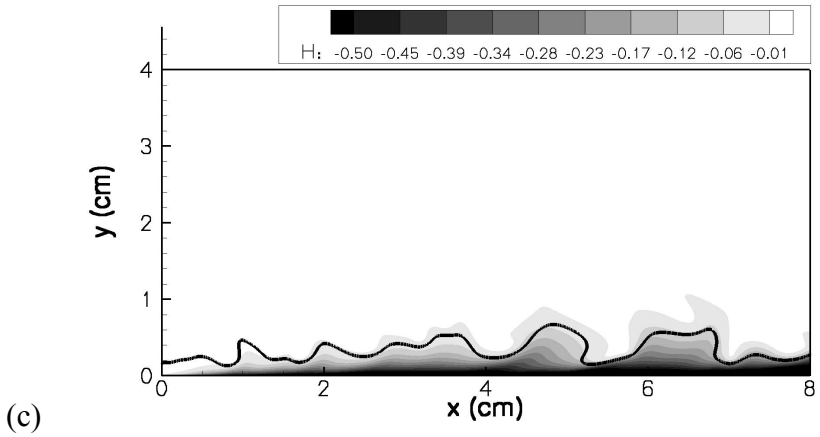

(c)

Figure 6-5. see caption of figure 6-3. Case 3 solution. Two wall-induced flame extinction events are observed in figure (b), near (x = 0.8 cm; y = 0.2 cm) and (x = 5.5 cm; y = 0.2 cm). Figure (c) also presents the spatial variations of the excess enthalpy variable H.

Figure 6-4 presents similar results, as obtained in case 2 (adiabatic wall, higher turbulence intensity). In this case, the turbulence levels are high enough to break the flame sheet into several segments; these levels remain sub-critical, however, and a comparison between figures 6-4(b) and 6-4(c) indicates that the flame remains extinction free. The temperature levels in the near-wall region (see figure 6-4(a)) exhibit larger fluctuations than that found in case 1 due to the intermittent penetration of cold free stream gases down to the wall surface.

Figure 6-5 presents the results obtained in case 3 (cold wall temperature, lower turbulence intensity). A comparison between figures 6-5(b) and 6-5(c) indicates that case 3 features several flame extinction events (similar observations are made in case 4). As seen in figure 6-5(a), the structure of the thermal boundary layer is quite different from that observed in figures 6-3(a) and 6-4(a): a thin cold sub-region develops near the wall and the flame is now exposed to wall-induced heat losses. These heat losses occasionally become super-critical and lead to the extinction events seen in figure 6-5(b).

We continue below our discussion of the flame structure, but choose to adopt hereafter a more theoretical perspective. We start from the classical Burke-Schumann description of non-premixed combustion, in which equilibrium chemistry (*i.e.* fast chemistry) is assumed and the flame is controlled by the fuel-air mixing process [22, 54, 147]. In the Burke-Schumann solution, the full reactive mixture composition is uniquely mapped as a function of the fuel-air-based mixture fraction *Z*. (We present in Appendix C a detailed description of Burke-Schumann solution, as well as an extension of the theory to the case with the presence of a adiabatic or non-adiabatic

wall.) While useful as a starting point and a valuable reference, the Burke-Schumann theory is also often too simple and deviations from chemical equilibrium are frequently observed in practical applications; these deviations are particularly large in the presence of flame extinction. In the classical flamelet theory of turbulent non-premixed combustion, deviations from fast chemistry behavior are monitored by the introduction of a second mixing variable χ_{st}: the deviations are insignificant for χ_{st} much smaller than $\chi_{st,ext}^{ad}$, and large otherwise. This point of view is similar to that adopted in figure 6-1. Thus, in the flamelet theory, the flame chemical structure is described in terms of the two variables Z and χ_{st} [22, 54, 147].

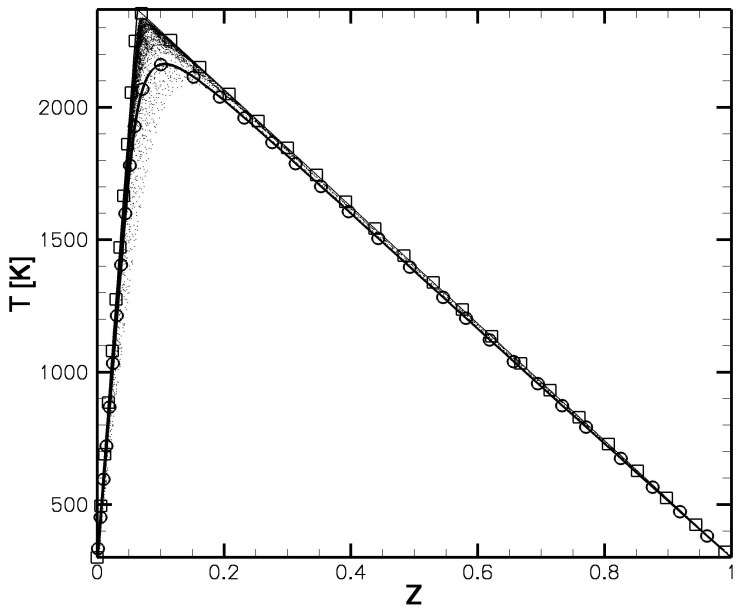

Figure 6-6. Scatter plot of temperature versus fuel-air-based mixture fraction. Case 2 solution. The DNS data correspond to an arbitrarily chosen time in the simulation, and are compared to two reference curves: the adiabatic Burke-Schumann solution (squares, equation (C4)), and one laminar flame profile (circles). The laminar profile corresponds to a steady, one-dimensional, plane, laminar counter-flow flame, with $\chi_{st} = 36.3\ s^{-1}$.

We now extend the previous discussion to the Burke-Schumann and flamelet descriptions of fluid temperature variations. We consider the adiabatic case first (cases 1-2 in table 6-1). The extension is in that case trivial. For instance, in the Burke-Schumann theory, T is simply described in terms of Z (Appendix C), while in the flamelet theory, T is a function of both Z and χ_{st}. Figure 6-6 presents a scatter plot of fluid temperature versus mixture fraction, as obtained in case 2. The adiabatic Burke-Schumann solution (equation (C4) in Appendix C) and one laminar flame profile are also plotted for reference; the flame profile is taken from the laminar diffusion flame database described in the previous section, and corresponds to a high (albeit sub-critical) value of the mixing rate χ_{st}. Figure 6-6 shows that the temperature variations in the present flame-wall configuration are laminar-like, well-correlated with Z, and essentially similar to those observed in traditional wall-free configurations [22, 54, 147].

A slightly different perspective is adopted in figure 6-7 where the variations of the flame temperature T_{st} are plotted as a function of the mixing rate χ_{st}. Flame temperatures are defined as the values of T conditioned on being on the stoichiometric iso-contour of mixture fraction, $Z = Z_{st}$. Data points from our pre-computed database of strained laminar diffusion flames are also plotted for reference. Figure 6-7 reveals that in case 2, the flame-wall configuration features occasional trans-critical flame-flow conditions, as characterized by large values of χ_{st}, up to $\chi_{st,ext}^{ad} \approx 45\,\mathrm{s}^{-1}$, and by significant reductions in flame temperature, down to less than 1200 K. However, as illustrated in figure 6-4, the trans-critical events are not strong enough and the turbulent flame remains extinction-free. These results are

consistent with observations made in previous studies of unsteady (oscillating) strained laminar diffusion flames, in which it is shown that the instantaneous occurrence of super-critical conditions is a necessary but not a sufficient condition to lead to flame extinction (see for instance reference [148]). It is shown in reference [148] that super-critical conditions have to be sustained over a sufficiently long period of time for extinction to occur.

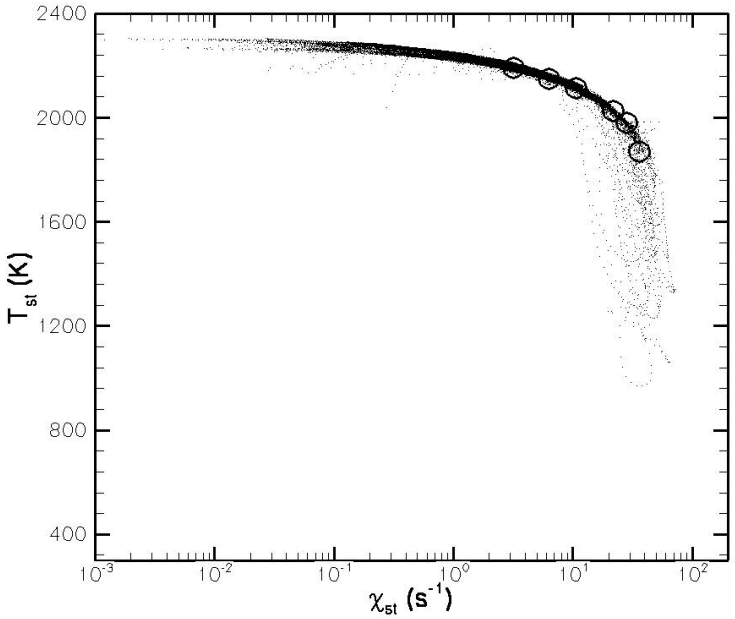

Figure 6-7. Scatter plot of flame temperature versus fuel-air mixing rate. Case 2 solution. The DNS data correspond to an arbitrarily chosen time period of 10 ms in the simulation, and are compared to reference data points (circles). The reference data points correspond to steady, one-dimensional, plane, laminar counter-flow flames.

We now turn to the isothermal cold wall case (cases 3-4 in table 1). Cases 3 and 4 exhibit two new features: flame extinction and non-adiabatic combustion conditions (figure 6-5). Both features contribute to make the description of fluid temperature variations significantly more complex: the occurrence of flame extinction results in large deviations from chemical equilibrium; and the basic analogy between

mass and heat mixing is lost under non-adiabatic conditions. As explained in Appendix C, the Burke-Schumann coupling relations between reactive species mass and thermal energy are no longer valid in non-adiabatic flames, and the several definitions of mixture fraction, as a fuel-air, fuel-temperature or oxygen-temperature mixing variable, are all different. The developments presented in Appendix C suggest that even in the framework of fast chemistry, more than one variable is now needed to describe the thermal flame structure.

Figure 6-8 presents a scatter plot of fluid temperature versus the fuel-air-based mixture fraction. In contrast to figure 6-6 where T and Z exhibit a high-level of correlation, the same variables in figure 6-8 now appear uncorrelated. Low temperature levels on the fuel-side of the flame, $Z \geq 0.15$, result from (direct) wall cooling effects, while low temperature levels in the vicinity of the flame zone, $Z \approx Z_{st}$, or on the air-side of the flame, $Z \leq Z_{st}$, are associated with flame extinction events. The increased complexity in the description of temperature variations is also apparent in figure 6-9 where the flame temperatures are plotted versus the stoichiometric fuel-air mixing rate. Figure 6-9 confirms that in case 4, the flame-wall configuration features a significant probability of flame extinction, as characterized by large reductions in flame temperature, down to less than 500 K. In figure 6-9, intermediate temperature levels, 600 K $\leq T \leq$ 1600 K, may be interpreted as transient extinction or re-ignition events.

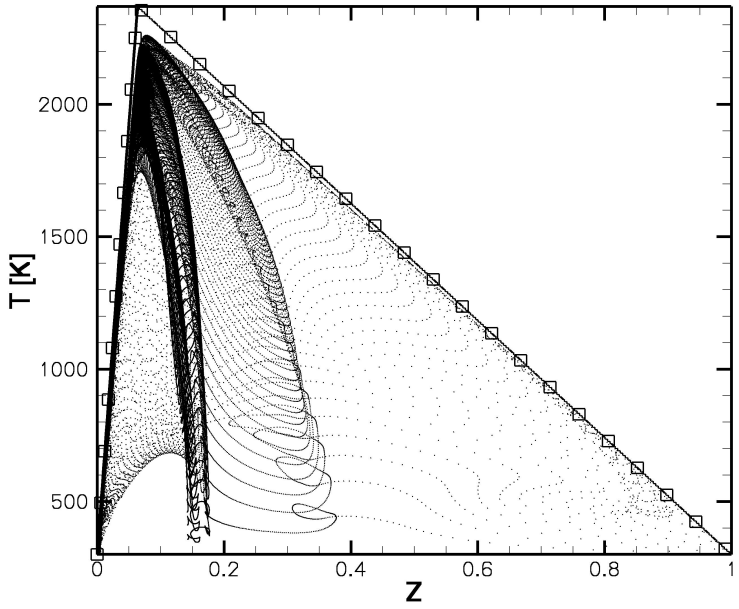

Figure 6-8. Scatter plot of temperature versus fuel-air-based mixture fraction. Case 4 solution. The DNS data correspond to an arbitrarily chosen time in the simulation, and are compared to the adiabatic Burke-Schumann solution (squares, equation (C4)).

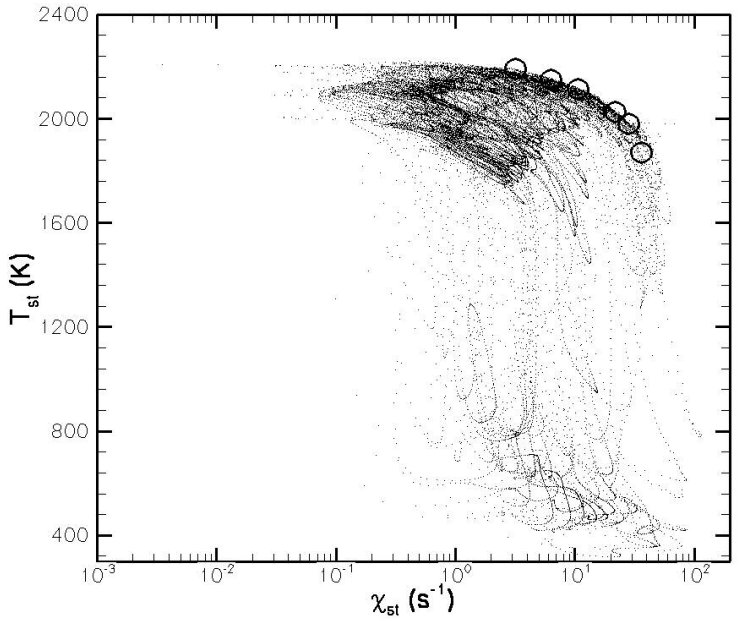

Figure 6-9. Scatter plot of flame temperature versus fuel-air mixing rate. Case 4 solution. The DNS data correspond to an arbitrarily chosen time period of 10 ms in the simulation, and are compared to reference data points (circles). The reference data points correspond to (adiabatic) steady, one-dimensional, plane, laminar counter-flow flames.

To gain further insight into the wall-flame temperature variations, we now consider case 3, in which flame extinction is observed (figure 6-5) but is less frequent than in case 4. We also limit our discussion to an instantaneous snapshot from the case 3 solution, and select a time in the simulation that is extinction-free, $t = t_{ef}$. Under flame-extinction-free conditions, we expect the temperature variations to be fairly well approximated by the extended Burke-Schumann solution discussed in Appendix C. In Appendix C, the flame response to wall cooling is described in terms of the mixture fraction Z and a normalized heat loss variable H called the excess enthalpy variable [149, 150]:

$$H = \frac{c_p (T - T^{\infty})}{\Delta H_c} \left(\frac{1}{Y^{\infty}_{C_2H_4}} + \frac{1}{(Y^{\infty}_{O_2} / r_s)} \right) + \frac{Y_{C_2H_4}}{Y^{\infty}_{C_2H_4}} + \frac{Y_{O_2}}{Y^{\infty}_{O_2}} - 1 , \tag{6-3}$$

where Y^{∞}_k designates the fuel or oxygen mass fraction in the supply stream; r_s the stoichiometric oxygen-to-fuel mass ratio; and T^{∞} the free-stream temperature. H is a non-dimensional quantity that varies between (-1) and 0. Under adiabatic conditions, $H = 0$; under non-adiabatic conditions, $H \neq 0$ and the deviations of H from 0 give a local measure of the amount of heat loss resulting from the wall cooling process. In Appendix C, the temperature variations are expressed as a function of Z and H (equations (C4) and (C12)):

$$\begin{cases} T(Z,H) = T^{\infty} + \left(\dfrac{Y^{\infty}_{C_2H_4} \Delta H_c}{c_p} \right) (Z + H \times Z_{st}) , & 0 \le Z \le Z_{st} , \\ T(Z,H) = T^{\infty} + \left(\dfrac{Y^{\infty}_{O_2} \Delta H_c}{r_s c_p} \right) ((1 - Z) + H \times (1 - Z_{st})) , & Z_{st} \le Z \le 1. \end{cases} \tag{6-4}$$

The validity of the extended Burke-Schumann solution given in equation (6-4) is tested in figure 6-10. Figure 6-10 presents three scatter plots of temperature versus

mixture fraction; the plots correspond to the pre-selected time $t = t_{ef}$ and to three different x-locations. The adiabatic Burke-Schumann solution is also plotted for reference. Figure 6-10 shows the expected downstream decrease in values of Z as gases from the fuel supply stream mix with, and get diluted by the surrounding gases from the air stream. Figure 6-10 also shows the downstream increase in values of H as the near-wall cold sub-layer grows in size and interacts with the flame more deeply.

These results are consistent with the plot shown in figure 6-5(c) (with the difference that figure 6-5 features two flame-extinction events). Figure 6-5(c) compares the location of the wall-cooled region (*i.e*. the region that exhibits negative values of H) to that of the flame (*i.e*. the stoichiometric fuel-air interface) and thereby provides a helpful graphic representation of occurrences of thermal flame-wall interactions: flame elements that lie in the white or light gray regions in figure 6-5(c) are quasi-adiabatic, whereas flame elements that lie in the dark gray region are strongly non-adiabatic and susceptible to wall-induced extinction events.

We now return to figure 6-10. Each plot in figure 6-10 also compares DNS raw data with processed data. Processed data correspond to estimates of fluid temperature using equation (6-4) and the local values of Z and H. Figures 6-10 reveals some discrepancies between raw and processed data; these discrepancies may be explained by finite rate chemistry effects (*i.e*. effects of χ_{st} in a flamelet description), which are unaccounted for in equation (6-4). Despite these discrepancies, the overall agreement between raw and processed data is good, and the comparison lends support to the theoretical developments presented in Appendix A.

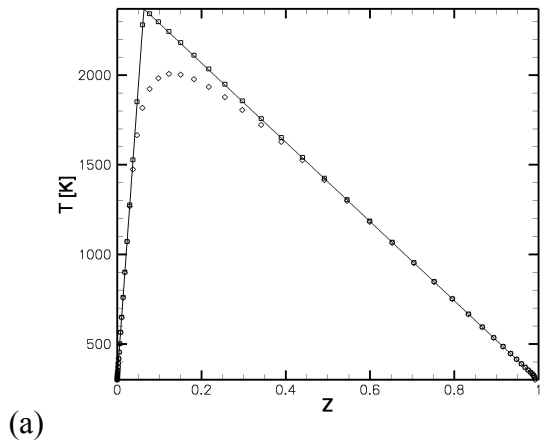

(a)

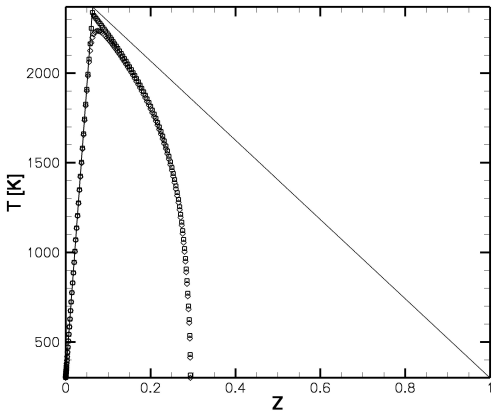

(b)

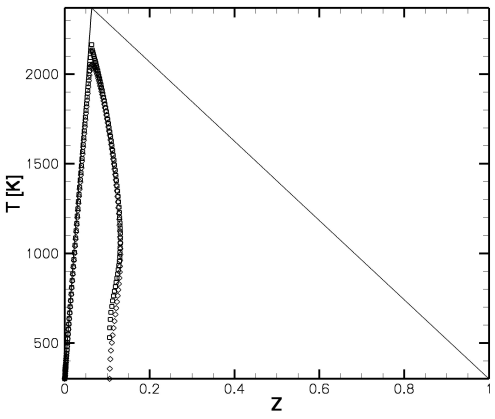

(c)

Figure 6-10. Scatter plots of flame temperature versus fuel-air-based mixture fraction. Case 3 solution. The DNS data correspond to a time in the simulation that is flame-extinction-free, and to three different x-locations: (a) $x = 0$; (b) $x = 1.97$ cm; (c) $x = 7.9$ cm. The DNS raw data (diamonds) are also compared to the adiabatic Burke-Schumann solution (solid line, equation (A4)), and to reference data (squares) processed according to the extended Burke-Schumann solution in equation (6-4).

Thus, we may conclude that in the absence of flame extinction, non-adiabatic temperature variations may be described as a function of mixture fraction Z and excess enthalpy H. In the next sub-section, we extend this discussion to cases with flame extinction. We suggest that the classical flamelet description may be readily adapted to treat this case, using Z, H and χ_{st} as controlling variables, with the difference that flame extinction is then predicted with a modified criterion.

Wall-Flame Extinction

As discussed above, the adiabatic cases 1-2 remain extinction free (figures 6-3, 6-4). Case 2 does feature occasional occurrences of trans-critical flame-flow conditions (figure 6-7) but these occurrences lack adequate strength and fail to fully overpower the flame. In contrast, the non-adiabatic cases 3-4 feature a number of local flame extinction events (figure 6-5, 6-9). Thus, a simple comparison between cases 1-2 and 3-4 indicates that in our particular DNS configuration, flame extinction is the direct consequence of wall cooling effects.

We focus our attention in this section on the conditions that lead to flame extinction. We start from the classical theory of (adiabatic) laminar diffusion flames in which flame extinction is described as a consequence of excessive values of the fuel-air mixing rate: $\chi_{st} \geq \chi_{st,ext}^{ad}$ [22, 54, 147]. The critical value $\chi_{st,ext}^{ad}$ may be evaluated from theoretical expressions [24], from detailed numerical calculations of one-dimensional strained laminar diffusion flames (figure 6-1), or from experiments. A useful prediction from large-activation-energy asymptotic theory is that the critical value $\chi_{st,ext}^{ad}$ is an exponentially increasing function of the flame temperature,

$\chi_{st,ext}^{ad} \sim \exp(-T_a / T_{st}^{ad})$, where T_a is a characteristic activation temperature and T_{st}^{ad} the adiabatic flame temperature [24]. We now use this prediction to establish a correspondence between the different flame responses to stretch, under adiabatic and non-adiabatic conditions.

In the presence of wall-induced heat losses, the flame temperature T_{st} is decreased, $T_{st} \le T_{st}^{ad}$, and following the previous discussion, we expect the extinction value of the fuel-air mixing rate to be lowered accordingly: $\chi_{st,ext} \le \chi_{st,ext}^{ad}$. Assuming an exponential relationship between $\chi_{st,ext}$ and T_{st}, we have the following relations:

$$\chi_{st,ext} = \chi_{st,ext}^{ad} \frac{\exp(-T_a / T_{st})}{\exp(-T_a / T_{st}^{ad})} = \chi_{st,ext}^{ad} \exp\left(\frac{\beta H_{st}}{1 + H_{st}(T_{st}^{ad} - T^{\infty})/T_{st}^{ad}}\right) \qquad (6\text{-}5)$$

or:

$$\chi_{st,ext} \approx \chi_{st,ext}^{ad} \exp(\beta H_{st}), \qquad (6\text{-}6)$$

where β is a characteristic Zeldovich number, $\beta = T_a(T_{st}^{ad} - T^{\infty})/(T_{st}^{ad})^2$ ($\beta \approx 5.57$ in the present S3D flame model, as described in equations (6-1)-(6-2)), and H_{st} is the value of excess enthalpy at the flame location, $H_{st} = H(Z_{st})$ (keep in mind that wall cooling results in negative values of H). Using equation (6-6), flame extinction is predicted when:

$$\chi_{st} \ge \chi_{st,ext} \approx \chi_{st,ext}^{ad} \exp(\beta H_{st}). \qquad (6\text{-}7)$$

Equations (6-6)-(6-7) provide a simple correction to the adiabatic flame extinction criterion established in the classical diffusion flame theory. The correction takes the form of a multiplicative factor $\exp(\beta H_{st})$; this factor depends on the magnitude of the flame heat losses, through H_{st}, as well as on the sensitivity of the flame chemistry

to temperature variations, through β. Equation (6-7) implies that flame extinction conditions are more readily achieved as the flame moves closer to the wall and experiences larger negative values of H_{st}.

We now turn to a DNS-based evaluation of the wall-modified flame extinction criterion proposed in equation (6-7). We consider case 4, in which frequent flame extinction events are observed, and case 2, in which occasional trans-critical events are observed, but without flame extinction. The evaluation of flame extinction conditions in case 4 is not straightforward since, as seen in figure 6-9, the simulated flame exhibits a range of combustion conditions that correspond to different states: a burning state; a non-burning state; and two transitional states, from burning to non-burning (extinction) and from non-burning to burning (re-ignition). Therefore, in order to differentiate between all possible states and to achieve our objective of focusing on extinction conditions, we need first to develop a detection scheme that can extract the incipient flame extinction events from the DNS raw data.

Figure 6-11 presents our flame extinction detection scheme. The scheme may be applied to any instantaneous snapshot of the DNS solutions; it is based on: (A) the identification of the instantaneous flame surface as the stoichiometric iso-contour of the fuel-air-based mixture fraction, $Z = Z_{st}$; (B) the evaluation of the local fuel-air mixing rate χ_{st} and excess enthalpy H_{st} along the entire flame surface; (C) the subsequent evaluation of a flame weakness factor, defined as $R = (\chi_{st} / \chi_{st,ext}) \approx (\chi_{st} / \chi^{ad}_{st,ext}) \times \exp(-\beta H_{st})$; (D) and finally the identification of the flame weakest spots as local peak values of R.

Once potential flame extinction events are identified as *R*-maxima, we can proceed to track their time evolution by simply repeating the detection scheme at different closely-spaced time intervals. Note that the proposed diagnostic remains Eulerian-based and is different from, and much simpler than a Lagrangian tracking technique that would accurately follow a particular flame element; the Eulerian treatment presents the advantage of tracking the flame locations that feature the most critical conditions, as measured by the weakness factor *R*, and it remains unclear whether a Lagrangian treatment would provide more valuable insight. The flame weakest spots are tracked as they are convected downstream and out of the computational domain; the data processing activated during tracking consists in recording the local value of temperature at the different marked flame locations.

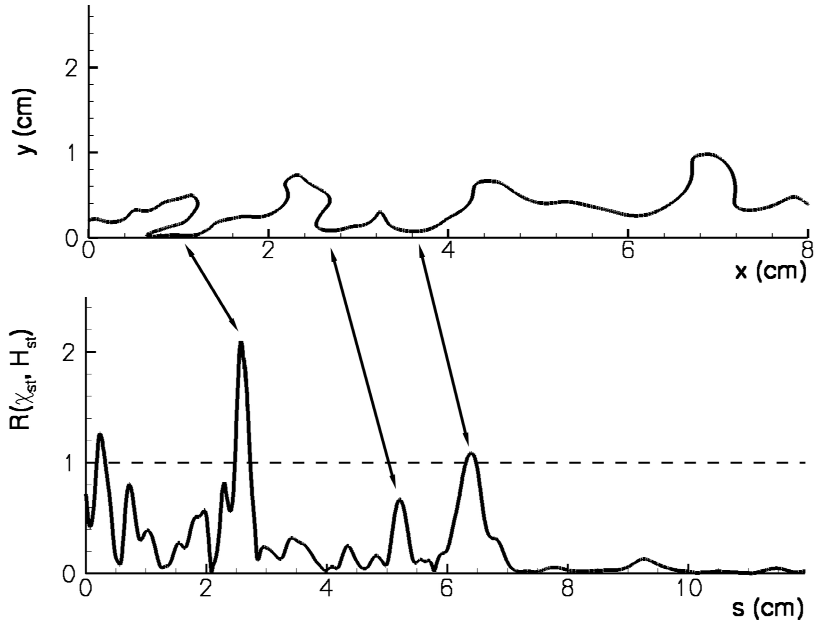

Figure 6-11. Flame extinction detection scheme. The scheme consists in monitoring the variations of the flame weakness factor, $R = (\chi_{st} / \chi_{st,ext}) \approx (\chi_{st} / \chi_{st,ext}^{ad}) \times \exp(-\beta H_{st})$. The upper plot shows the flame location in physical space while the lower plot shows the corresponding variations of *R* as a function of arc length along the flame contour. The flame weakest spots are readily identified as peak values of *R* in the lower plot, and flame extinction is predicted to occur for *R* above a critical value (*i.e.* $R \geq 1$ in equation (6-7)).

Consistent with the criterion proposed in equation (6-7), we find that in case 4, observations of flame extinction events are well-correlated with occurrences of large peak values of the flame weakness factor R (similar observations are made in case 3). In equation (6-7), extinction is predicted to occur for a critical value of R equal to 1. This prediction is now tested in figure 6-12. Figure 6-12 presents the time variations of temperature, as recorded at several flame weak spot locations, and using the detection algorithm of figure 6-11. To facilitate the comparison with equation (6-7), the time variations of T_{st} are plotted as a function of R, instead of time. Figure 6-12 includes one trans-critical event from case 2 and three super-critical events from case 4; data points from our pre-computed database of strained laminar diffusion flames are also plotted for reference. The plot displays the classical evolution of temperature as the flame experiences a change from sub- to super-critical conditions: the flame temperature exhibits a gradual decrease at first, for low-to-moderate values of R, followed by an abrupt fall off (down to ambient temperatures), as R is further increased beyond a critical value noted R_c and the flame undergoes sudden extinction.

In agreement with equation (6-7), figure 6-12 shows that the trans- and super-critical flame events from cases 2 and 4 are characterized by large values of R close to unity. In contrast to equation (6-7), however, flame extinction is observed for a range of values of R_c, rather than a unique distinct value: we find that $0.3 \leq R_c \leq 1.2$. Also, there is some level of disagreement between results from case 2 and case 4: while in figure 6-12, the flame event from case 2 features large values of R, up to more than 1, and yet remains chemically active, one of the flame event in case 4 undergoes

complete extinction at a significantly lower value of the flame weakness factor, $R_c \approx$ 0.3-0.5.

Despite these discrepancies, we find that the DNS results lend support to the modified flame extinction criterion proposed in equation (6-7). In our view, this criterion provides a useful quantification of the magnitude of the flame weakening resulting from the wall cooling process.

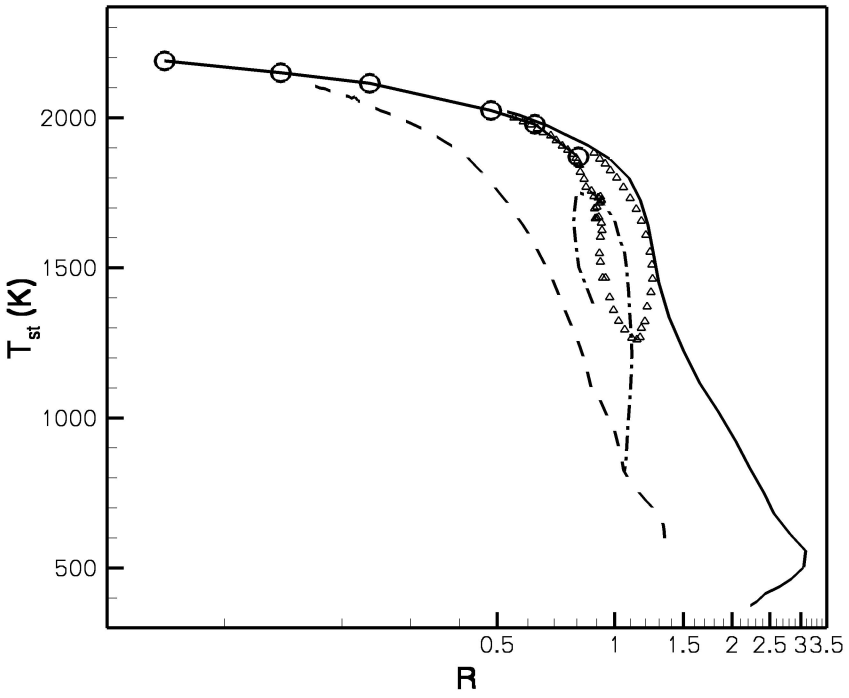

Figure 6-12. Variations of the flame temperature T_{st} with the flame weakness factor R, at selected flame locations. Case 2 (triangles) and case 4 (lines) solutions. The DNS data correspond to several flame weak spots, as identified using the detection algorithm presented in figure 6-11. The DNS data are compared to reference data points (circles). The reference data points correspond to (adiabatic) steady, one-dimensional, plane, laminar counter-flow flames.

Wall Surface Heat Flux

We now turn to an evaluation of the wall surface heat flux, as obtained in cases 3-4 of the DNS database. As discussed in previous sections, thermal radiation transport is neglected in the present study and gas-to-solid heat exchanges are limited to convective heat transfer. Also, the DNS simulations are well-resolved and the wall heat flux is simply obtained from its classical Fourier-law expression and direct differentiation of the temperature field.

Figure 6-13 presents the statistical distribution of the gas-solid heat flux, as obtained in cases 3 and 4. The probability density functions in figure 6-13 correspond to data collected on the entire wall surface, and over a time period of 20 ms. In both cases 3 and 4, the averaged and peak values of the wall heat flux are approximately 40 kW/m^2 and 90 kW/m^2, respectively. These values are much smaller than those reported in reference [137]; the peak heat flux in reference [137] is as high as the flame reference power, *i.e.* up to 1-3 MW/m^2 for typical hydrocarbon flames at atmospheric pressure.

Discrepancies between the present results and those reported in reference [137] may be due to differences in the respective flame-flow configurations, as well as differences in the adopted combustion models. For instance, our present choice of a simplified flame model results in an underestimate of the flame resistance to stretch (figure 6-1) that may lead in turn to over-predictions in minimum flame-wall distances and under-predictions in the associated wall heat fluxes. We plan to address this issue in future work by performing DNS simulations with a more realistic flame chemistry model.

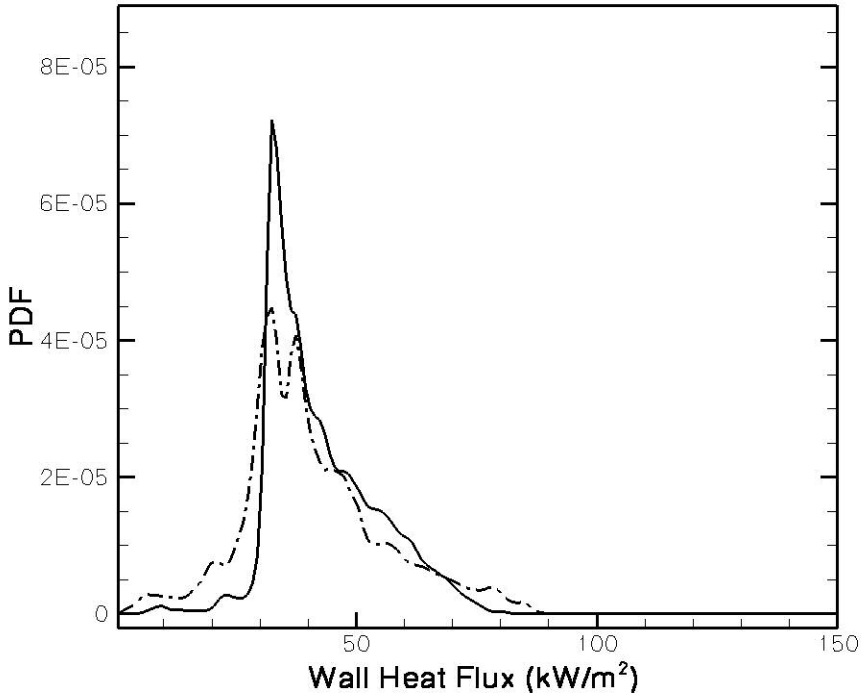

Figure 6-13. Probability density function (PDF) of the wall surface heat flux. Case 3 (solid line) and case 4 (dashed line) solutions. The PDF data are accumulated both in space, along the entire wall surface at $y = 0$, and in time, over a time period of 20 ms.

6.4. Conclusion

Direct numerical simulation is used in this study to bring basic information on the interactions of non-premixed flames with adiabatic or cold wall surfaces. The simulations correspond to momentum-driven, ethylene-air, turbulent wall-flames, and feature sub-critical flame dynamics, in the case of an adiabatic wall, and super-critical flame dynamics, in the case of a cold wall.

The different simulated wall-flames are analyzed in the present study with a flamelet view point. In the adiabatic wall case, the flame chemical and thermal structure is described in terms of classical variables, *i.e.* mixture fraction and scalar

dissipation rate. In the cold wall case, the description of the flame thermal structure requires the introduction of an additional variable, called excess enthalpy. The excess enthalpy concept was apparently first applied to the description of non-adiabatic diffusion flames in references [149, 150]. In agreement with references [149, 150], we find that in our flame-wall configuration, the excess enthalpy variable provides a convenient description of the amount of heat loss resulting from the wall cooling process. Using mixture fraction and excess enthalpy as principal variables, an extended Burke-Schumann description of the flame structure, valid in the limit of equilibrium chemistry, is presented in Appendix C.

A modified flame extinction criterion is then proposed that provides a correction factor to the classical scalar dissipation rate criterion obtained in adiabatic flame theory. This correction factor depends on the magnitude of the wall-induced flame heat losses, through the excess enthalpy, as well as on the sensitivity of the flame chemistry to temperature variations, through a Zeldovich number. The modified flame extinction criterion is tested against the DNS data using an innovative detection algorithm designed to identify the locations of the flame weakest spots. We find that the results are encouraging and lend support to an extended flamelet framework enhanced by the concept of excess enthalpy.

Additional results include a quantification of the mean and peak values of the convective wall heat flux resulting from the short flame-wall distances. These values are in the range of a few tens of kW/m^2 and are much smaller than the maximum heat flux reported in a similar study, but for a highly-strained laminar diffusion counter-flow flame [137]. Discrepancies between our results and those of reference [137]

remain unexplained and will be the focus of follow-up studies. It is worth emphasizing again that the present numerical formulation includes a number of simplifications/limitations: a two-dimensional computational domain; a single-step flame chemistry model; no heterogeneous gas-solid surface chemistry; no soot formation; and no thermal radiation transport. Future work will be aimed at removing those limitations with the goal of achieving more quantitative simulations.

Chapter 7: Conclusion and Future Directions

Direct numerical simulation is a mature research tool for studying turbulent reacting flows. In the present work, we are motivated by the fast development of the tera-scale computing facilities, and participate in developing a state-of-the-art DNS software with new numerical and physical modeling capabilities for tera-scale computing platforms.

The new numerical developments include a new pseudo-compressibility method, the Acoustic Speed Reduction (ASR) method, designed to enhance computational efficiency for low speed compressible flow simulations, and an improved boundary condition scheme to solve known difficulties found in counterflow simulations, allowing for successful simulations of turbulent counterflow flames. The new physical developments include a semi-empirical soot model and a parallel thermal radiation model based on a ray-tracing method. With the new developments, we extend the domain of application of DNS to new problems with more complex physics, or increase the computational efficiency in the treatment of current problems.

While the new DNS code has been equipped with the new capabilities of soot formation and thermal radiation, it still has limitations for general applications. The current semi-empirical soot model requires a calibration of model coefficient before application to new flame configurations. More detailed soot models using the method of moments or the sectional method are supposed to be more accurate and readily applicable to more general situations. The current radiation solver assumes that the

combustion gas mixture is a gray gas. It is a reasonable assumption for optically thin gases or when soot radiation is dominant. However gas phase absorption is strongly spectral dependent. Therefore a spectrally-resolved thermal radiation capability is desirable. On the other hand, it is still worth emphasizing that the computational cost for more sophisticated soot and radiation models is still prohibitive. In our view, the current flame modeling capability corresponds to a reasonable and solid step towards a better understanding and modeling of complicated physics in reacting flows.

In addition to the new developments, the present work also applied the DNS solver to study the interaction of non-premixed flames with cold wall surfaces. The simulations addressed some new problems associated with the effects of the cold wall on the turbulent flame and brought basic information on turbulent fuel-air-temperature mixing, flame extinction and wall surface heat transfer. New information on the wall-modified flame structure and wall-induced flame extinction events was obtained and new theoretical developments were made using the concept of excess enthalpy variable. Note that the current simulations did not make use of the new capabilities developed in this PhD work. However, the new developments are indeed applicable to the current DNS study. We choose to neglect soot and thermal radiation to avoid excessive complications for the initial study of turbulent flame-wall interactions. The ASR method together with non-reflecting inflow boundary conditions are currently under test in this flame-wall interactions configuration. We hope to achieve more computational efficiency for three-dimensional simulations of flame-wall interactions problems in the future.

The new observations made in the DNS of non-premixed flame-wall interactions are very encouraging. The interpretation of the observations in terms of the excess enthalpy variable has implications for turbulent combustion modeling. An extension of the DNS work should be to develop a boundary layer model that accounts for the presence of a flame and wall cooling effects. It is also highly desirable to perform three-dimensional DNS of the flame-wall interaction problem, where the wall induced modifications of turbulent mixing in diffusion flames can be studied with realistic turbulence. In addition it is also of interest to include detailed chemical kinetics, soot and thermal radiation in the simulation to achieve more quantitative predictions. There is also a need to validate the DNS simulations against experiments. With current computer resource, direct comparison between DNS and experiments is still a daunting task, but it is definitely desirable if we can overcome the prohibitive computational requirement in the future.

This work has mad several contributions in computational physics and combustion science. The new pseudo-compressibility method presented in chapter 2 has been published in Combustion Theory and Modelling [151]; the enhanced formulation for boundary conditions presented in chapter 3 has been accepted for publication in Combustion Theory and Modelling [74]; the study of flame-wall interaction presented in chapter 6 has been submitted for publication to Combustion and Flame [152]. The performance study of coupled flame-flow-radiation calculation presented in chapter 5 is still in progress and a journal article is in preparation.

Appendices

A: Alternative Forms of the Energy Equation

We start from the equation for total energy (internal energy plus kinetic energy) given in equation (1.4):

$$\frac{\partial}{\partial t}(\rho E)+\frac{\partial}{\partial x_j}(\rho E u_j)=-\frac{\partial}{\partial x_j}(p u_j)+\frac{\partial}{\partial x_j}(\tau_{ij}u_i)-\frac{\partial q_j}{\partial x_j}+\rho g_j u_j .$$

This equation may be recast as an enthalpy equation:

$$\left[\frac{\partial}{\partial t}(\rho H)+\frac{\partial}{\partial x_j}(\rho H u_j)\right]-\left[\frac{\partial p}{\partial t}+u_j\frac{\partial p}{\partial x_j}\right]=\tau_{ij}\frac{\partial u_i}{\partial x_j}-\frac{\partial q_j}{\partial x_j}, \qquad \text{(A1)}$$

where H is the enthalpy per unit mass and is defined as:

$$H=E+\frac{p}{\rho}-\left(\frac{u_j u_j}{2}\right)=\sum_{k=1}^{N_s}h_k Y_k=\sum_{k=1}^{N_s}\left(h_k^0+\int_{T_0}^{T}c_{p,k}\,dT\right)Y_k .$$

Two alternative forms for the energy equation are given below. First, using the definition of H as a mass-weighted sum of the chemical species enthalpies h_k, and considering the variations of h_k with temperature, a new expression for the material derivative of H is obtained:

$$\left[\frac{\partial H}{\partial t}+u_j\frac{\partial H}{\partial x_j}\right]=\sum_{k=1}^{N_s}h_k\left[\frac{\partial Y_k}{\partial t}+u_j\frac{\partial Y_k}{\partial x_j}\right]+c_p\left[\frac{\partial T}{\partial t}+u_j\frac{\partial T}{\partial x_j}\right],$$

where c_p is the specific heat of the gaseous mixture at constant pressure:

$$c_p=\sum_{k=1}^{N_s}c_{p,k}Y_k .$$

Using the mass conservation statements in equations (1.1)-(1.2), an equivalent expression is as follows:

$$\left[\frac{\partial}{\partial t}(\rho H)+\frac{\partial}{\partial x_j}(\rho H u_j)\right]=-\sum_{k=1}^{N_S}h_k\frac{\partial}{\partial x_j}(\rho Y_k V_{k,j})+\sum_{k=1}^{N_S}h_k\dot{\omega}_k+\rho c_p\left[\frac{\partial T}{\partial t}+u_j\frac{\partial T}{\partial x_j}\right],$$

and equation (A1) may now be re-formulated as a temperature equation:

$$\rho c_p\left[\frac{\partial T}{\partial t}+u_j\frac{\partial T}{\partial x_j}\right]-\left[\frac{\partial p}{\partial t}+u_j\frac{\partial p}{\partial x_j}\right]=\tau_{ij}\frac{\partial u_i}{\partial x_j}-\frac{\partial q_j}{\partial x_j}+\sum_{k=1}^{N_S}h_k\frac{\partial}{\partial x_j}(\rho Y_k V_{k,j})-\sum_{k=1}^{N_S}h_k\dot{\omega}_k\ ,\text{(A2)}$$

or, after using the definition of the heat flux vector q_j:

$$\rho c_p\left[\frac{\partial T}{\partial t}+u_j\frac{\partial T}{\partial x_j}\right]-\left[\frac{\partial p}{\partial t}+u_j\frac{\partial p}{\partial x_j}\right]=\tau_{ij}\frac{\partial u_i}{\partial x_j}+\frac{\partial}{\partial x_j}\left(\lambda\frac{\partial T}{\partial x_j}\right)-\rho\left(\sum_{k=1}^{N_s}Y_k V_{k,j}c_{p,k}\right)\frac{\partial T}{\partial x_j}-\sum_{k=1}^{N_S}h_k\dot{\omega}_k.$$

The first term on the right-hand side of equation (A2) is the rate of viscous dissipation; the second term represents transport of heat due to conduction; the third term represents transport of heat due to multi-component mass diffusion effects; and the last term represents the rate of heat release associated with the chemical reaction process.

We now proceed to yet another form of the energy equation. Using the ideal gas law in equation (1.5), we can express temperature variations in terms of variations of pressure, mass density and species mass fractions:

$$\frac{1}{T}\left(\frac{\partial T}{\partial t}+u_j\frac{\partial T}{\partial x_j}\right)=\frac{1}{p}\left(\frac{\partial p}{\partial t}+u_j\frac{\partial p}{\partial x_j}\right)-\frac{1}{\rho}\left(\frac{\partial \rho}{\partial t}+u_j\frac{\partial \rho}{\partial x_j}\right)-\sum_{k=1}^{N_S}\frac{M}{M_k}\left(\frac{\partial Y_k}{\partial t}+u_j\frac{\partial Y_k}{\partial x_j}\right).\text{(A3)}$$

Combining this expression with equations (1.1)-(1.2), equation (A2) may then be recast as a pressure equation:

$$\frac{\partial p}{\partial t}+u_j\frac{\partial p}{\partial x_j}+\gamma p\frac{\partial u_j}{\partial x_j}=(\gamma-1)\left[\tau_{ij}\frac{\partial u_i}{\partial x_j}-\frac{\partial q_j}{\partial x_j}-\sum_{k=1}^{N_S}\left(h_k-\frac{Mc_pT}{M_k}\right)\left(-\frac{\partial}{\partial x_j}(\rho Y_k V_{k,j})+\dot{\omega}_k\right)\right],\text{(A4)}$$

where γ is the ratio of specific heats of the gaseous mixture.

Note that equations (A3)-(A4) may be simplified if one assumes that the molecular weights and specific heats of individual chemical species are all identical: $M_k = M$ and $c_{p,k} = c_p$. We get under those conditions:

$$\rho c_p \left[\frac{\partial T}{\partial t} + u_j \frac{\partial T}{\partial x_j} \right] - \left[\frac{\partial p}{\partial t} + u_j \frac{\partial p}{\partial x_j} \right] = \tau_{ij} \frac{\partial u_i}{\partial x_j} + \frac{\partial}{\partial x_j} \left(\lambda \frac{\partial T}{\partial x_j} \right) + \dot{q} , \tag{A5}$$

$$\frac{\partial p}{\partial t} + u_j \frac{\partial p}{\partial x_j} + \gamma p \frac{\partial u_j}{\partial x_j} = (\gamma - 1) \left[\tau_{ij} \frac{\partial u_i}{\partial x_j} + \frac{\partial}{\partial x_j} \left(\lambda \frac{\partial T}{\partial x_j} \right) + \dot{q} \right], \tag{A6}$$

where $\dot{q}$ is the heat release rate per unit volume:

$$\dot{q} = -\sum_{k=1}^{N_s} h_k \dot{\omega}_k .$$

B: A Mathematical Derivation of the ASR Transformation

As described in section 2.2, the ASR method uses a modified pressure-dilatation term in the energy equation. This modification is introduced in section 2.2 based on physical insights into the respective scaling of the acoustic and convective motions and a detailed analysis of the simplified problems TP1 and TP2. A more rigorous mathematical derivation of ASR is here presented based on asymptotic expansions of the governing equations. The analysis follows the developments made in references [153-155]. While as will become clear below, the scope of the analysis is somewhat limited, it serves to strengthen the foundations of the ASR method and establishes a framework for future investigations.

We start from the fully compressible, reactive flow system of equations:

$$\begin{cases} \dfrac{\partial \rho}{\partial t} + \dfrac{\partial}{\partial x_j}(\rho u_j) = 0, & \text{(B1)} \\ \dfrac{\partial}{\partial t}(\rho u_i) + \dfrac{\partial}{\partial x_j}(\rho u_i u_j) = -\dfrac{\partial p}{\partial x_i} + \dfrac{\partial \tau_{ij}}{\partial x_j}, & \text{(B2)} \\ \rho c_p \left[\dfrac{\partial T}{\partial t} + u_j \dfrac{\partial T}{\partial x_j} \right] - \left[\dfrac{\partial p}{\partial t} + u_j \dfrac{\partial p}{\partial x_j} \right] = \tau_{ij} \dfrac{\partial u_i}{\partial x_j} + \dfrac{\partial}{\partial x_j} \left(\lambda \dfrac{\partial T}{\partial x_j} \right) + \dot{q}, & \text{(B3)} \end{cases}$$

where the energy equation is recast as equation (A5). A number of simplifications have been made in this system of equations: individual chemical species mass equations are ignored; gravity is neglected in equation (B2); multi-component mass diffusion effects are neglected in equation (B3). We also assume below that the specific heat c_p and the ratio of specific heats γ are constant.

Equations (B1-B3) are made non-dimensional using the following reduced variables:

$$\begin{cases} x^+ = \dfrac{x}{(\nu_0 / u_0)} \; ; \; t^+ = \dfrac{t}{(\nu_0 / u_0^2)} \; ; \; u^+ = \dfrac{u}{u_0} \; ; \; \rho^+ = \dfrac{\rho}{\rho_0} \; ; \; p^+ = \dfrac{p}{p_0} \\ T^+ = \dfrac{T}{(p_0 / \rho_0 c_p)} \; ; \; \lambda^+ = \dfrac{\lambda}{(\rho_0 \nu_0 c_p / \mathrm{Pr})} \; ; \; \dot{q}^+ = \dfrac{\dot{q}}{(\rho_0 c_p \Delta T_0 / (\nu_0 / u_0^2))} \end{cases}$$

where the subscript 0 refers to reference state quantities; and where Pr is the Prandtl number (assumed constant) and ΔT_0 a reference temperature variation. We have the following expressions for the reference pressure and temperature:

$$p_0 = \frac{\rho_0 c_0^2}{\gamma} \; ; \; \frac{p_0}{\rho_0 c_p} = \frac{\gamma - 1}{\gamma} T_0$$

where c_0 is the speed of sound in the reference state.

For convenience, we drop the superscript + in the following with the implicit understanding that quantities are non-dimensional. Equations (B1-B3) are now written as:

$$\begin{cases} \dfrac{\partial \rho}{\partial t} + \dfrac{\partial}{\partial x_j}(\rho u_j) = 0, & \text{(B4)} \\ \dfrac{\partial}{\partial t}(\rho u_i) + \dfrac{\partial}{\partial x_j}(\rho u_i u_j) = -\dfrac{1}{\varepsilon^2}\dfrac{\partial p}{\partial x_i} + \dfrac{\partial \tau_{ij}}{\partial x_j}, & \text{(B5)} \\ \rho\left[\dfrac{\partial T}{\partial t} + u_j \dfrac{\partial T}{\partial x_j}\right] - \left[\dfrac{\partial p}{\partial t} + u_j \dfrac{\partial p}{\partial x_j}\right] = \varepsilon^2 \tau_{ij} \dfrac{\partial u_i}{\partial x_j} + \dfrac{1}{\mathrm{Pr}} \dfrac{\partial}{\partial x_j}\left(\lambda \dfrac{\partial T}{\partial x_j}\right) + \delta \dot{q}, & \text{(B6)} \end{cases}$$

where ε is a measure of the flow Mach number and δ a measure of the relative amplitude of temperature fluctuations. ε and δ are defined as:

$$\varepsilon = \sqrt{\gamma}\left(\frac{u_0}{c_0}\right) \; ; \; \delta = \frac{\gamma}{\gamma - 1}\left(\frac{\Delta T_0}{T_0}\right).$$

Next, we perform an analysis that is similar to that found in references [153-155]. The scope of this analysis is limited by a number of simplifying assumptions. First, we assume "nearly incompressible" conditions and treat the flow variables as asymptotic expansions in ε and δ (both parameters ε and δ are considered small). In addition, we choose the scaling $\delta = \varepsilon$ and limit our discussion to the heat-fluctuation-dominated hydrodynamics (HFDH) regime of reference [153]: in this regime, density and temperature fluctuations are dominant and pressure fluctuations are small in comparison. Finally, we consider that the fluid fluctuates close to a reference state assumed to be uniform: $p_0 = 1$; $\rho_0 = 1$; $T_0 = \gamma/(\gamma\text{-}1)$. These assumptions are consistent with the following leading order expansions:

$$\begin{cases} u_i = u_i^{(0)} + \varepsilon\, u_i^{(1)} \\ \rho = 1 + \varepsilon\, \rho^{(1)} \\ p = 1 + \varepsilon^2 p^{(2)} \\ T = \dfrac{\gamma}{\gamma - 1} + \varepsilon\, T^{(1)} \end{cases}$$

and as shown in references [153-155], the corresponding leading order equations are:

$$\begin{cases} \dfrac{\partial u_j^{(0)}}{\partial x_j} = 0, & \text{(B7)} \\ \dfrac{\partial u_i^{(0)}}{\partial t} + u_j^{(0)} \dfrac{\partial u_i^{(0)}}{\partial x_j} = -\dfrac{\partial p^{(2)}}{\partial x_i} + \dfrac{\partial \tau_{ij}^{(0)}}{\partial x_j}, & \text{(B8)} \\ \left[\dfrac{\partial T^{(1)}}{\partial t} + u_j^{(0)} \dfrac{\partial T^{(1)}}{\partial x_j} \right] = \dfrac{1}{\mathrm{Pr}} \dfrac{\partial}{\partial x_j} \left(\lambda \dfrac{\partial T^{(1)}}{\partial x_j} \right) + \dot{q}. & \text{(B9)} \end{cases}$$

As expected, the pressure term on the left-hand-side of the energy equation (B3) does not contribute to the leading order dynamics in equation (B9), an observation that is central to the ASR proposition that the pressure term in the energy equation may be freely manipulated.

We now consider the ASR-modified, non-dimensional, compressible, reactive flow equations:

$$\begin{cases} \dfrac{\partial \rho}{\partial t} + \dfrac{\partial}{\partial x_j}(\rho u_j) = 0, & \text{(B10)} \\ \dfrac{\partial}{\partial t}(\rho u_i) + \dfrac{\partial}{\partial x_j}(\rho u_i u_j) = -\dfrac{1}{\varepsilon^2} \dfrac{\partial p}{\partial x_i} + \dfrac{\partial \tau_{ij}}{\partial x_j}, & \text{(B11)} \\ \rho \left[\dfrac{\partial T}{\partial t} + u_j \dfrac{\partial T}{\partial x_j} \right] - \beta \left[\dfrac{\partial p}{\partial t} + u_j \dfrac{\partial p}{\partial x_j} \right] = \varepsilon^2 \tau_{ij} \dfrac{\partial u_i}{\partial x_j} + \dfrac{1}{\mathrm{Pr}} \dfrac{\partial}{\partial x_j} \left(\lambda \dfrac{\partial T}{\partial x_j} \right) + \delta \dot{q}, & \text{(B12)} \end{cases}$$

where β is a parameter to be determined. To obtain an expression for β, we must go beyond the previous analysis of the incompressible flow dynamics and include some representation of the acoustic physics. Following the approach proposed in [153], we consider the interaction of the incompressible flow solution described by equations (B7)-(B9) with superposed acoustic perturbations, and perform a multi-scale expansion in terms of long-time/short-wavelength convective scales, denoted τ and η_j, and fast-time/long-wavelength acoustic scales, denoted τ' and ξ_j:

$$\left.\begin{aligned} &\tau = t \;;\; \tau' = t/(\alpha\varepsilon) \\ &\eta_j = x_j \;;\; \xi_j = (\alpha\varepsilon)x_j \end{aligned}\right\} \tag{B13}$$

where the ASR factor α has been introduced in order to account for the intended artificial increase in the flow Mach number. We have the relations:

$$\frac{\partial}{\partial t} = \frac{\partial}{\partial \tau} + \frac{1}{(\alpha\varepsilon)}\frac{\partial}{\partial \tau'} \;;\; \frac{\partial}{\partial x_j} = \frac{\partial}{\partial \eta_j} + (\alpha\varepsilon)\frac{\partial}{\partial \xi_j}.$$

We also represent the variables as:

$$\left.\begin{aligned} u_i &= u_i^{(0)} + (\alpha\varepsilon)u_i^{(1)} \\ \rho &= 1 + (\alpha\varepsilon)\rho^{(1)} \\ p &= 1 + \varepsilon^2\left(p^{(2)} + p^*\right) \\ T &= \frac{\gamma}{\gamma - 1} + (\alpha\varepsilon)T^{(1)} \end{aligned}\right\} \tag{B14}$$

where $u_i^{(0)}$ and $p^{(2)}$ are solutions of the incompressible equations (B7)-(B8) (and are independent of the fast-time/long-wavelength acoustic scales τ' and ξ_j); where the ASR-modified scaling $\delta = (\alpha\varepsilon)$ has been assumed; and where p^* is the acoustic perturbation.

The expansion of equations (B10)-(B12) in terms of (B13) and (B14) gives (see reference [153] for more details):

$$\begin{cases} \dfrac{\partial \rho^{(1)}}{\partial \tau'} = 0, & \text{(B15)} \\ \dfrac{\partial \rho^{(1)}}{\partial \tau} + u_j^{(0)}\dfrac{\partial \rho^{(1)}}{\partial \eta_j} + \dfrac{\partial u_j^{(1)}}{\partial \eta_j} = 0, & \text{(B16)} \\ \dfrac{\partial u_i^{(1)}}{\partial \tau'} = -\dfrac{\partial p^*}{\partial \eta_i}, & \text{(B17)} \\ \dfrac{\partial T^{(1)}}{\partial \tau'} = 0, & \text{(B18)} \\ \dfrac{\partial T^{(1)}}{\partial \tau} + u_j^{(0)}\dfrac{\partial T^{(1)}}{\partial \eta_j} - \dfrac{\beta}{\alpha^2}\dfrac{\partial p^*}{\partial \tau'} = \dfrac{1}{\mathrm{Pr}}\dfrac{\partial}{\partial \eta_j}\left(\lambda\dfrac{\partial T^{(1)}}{\partial \eta_j}\right) + \dot{q}. & \text{(B19)} \end{cases}$$

Equations (B15) and (B18) show that the heat transfer variables ρ_1 and T_1 fluctuate on incompressible slow time scales; and it is worth noting that this basic result remains unchanged in presence of an ASR modification ($\alpha \neq 1$; $\beta \neq 1$). Note also that equation (B19) suggests that the interaction between slow/convective and fast/acoustic motions in the energy equation is dependent on α and β and may be altered by ASR modifications; this point deserves more scrutiny and will be addressed in future work.

We now proceed to establish the wave equation for the acoustic perturbations p^*. We first use the (non-dimensional) ideal gas law:

$$p = \frac{\gamma - 1}{\gamma} \rho T \,,$$

which together with the expansions (B14) leads to the following relations:

$$\begin{cases} \dfrac{\partial \rho^{(1)}}{\partial \tau} = -\dfrac{\gamma - 1}{\gamma} \dfrac{\partial T^{(1)}}{\partial \tau} + \dfrac{1}{\alpha^2} \dfrac{\partial p^*}{\partial \tau'}, & \text{(B20)} \\ \dfrac{\partial \rho^{(1)}}{\partial \eta_j} = -\dfrac{\gamma - 1}{\gamma} \dfrac{\partial T^{(1)}}{\partial \eta_j}. & \text{(B21)} \end{cases}$$

Combining equations (B20)-(B21) with equation (B16), we obtain:

$$\frac{\partial T^{(1)}}{\partial \tau} + u_j^{(0)} \frac{\partial T^{(1)}}{\partial \eta_j} - \frac{\gamma}{\gamma - 1} \frac{\partial u_j^{(1)}}{\partial \eta_j} - \frac{\gamma}{\gamma - 1} \frac{1}{\alpha^2} \frac{\partial p^*}{\partial \tau'} = 0 \,,$$

or, after using Eq. (B19):

$$\left(\frac{\gamma}{\gamma - 1} - \beta \right) \frac{1}{\alpha^2} \frac{\partial p^*}{\partial \tau'} + \frac{\gamma}{\gamma - 1} \frac{\partial u_j^{(1)}}{\partial \eta_j} = \frac{1}{\mathrm{Pr}} \frac{\partial}{\partial \eta_j} \left(\lambda \frac{\partial T^{(1)}}{\partial \eta_j} \right) + \dot{q} \,. \qquad \text{(B22)}$$

Finally, equations (B17) and (B22) lead to the following acoustic wave equations:

$$\begin{cases} \dfrac{\partial^2 p^*}{\partial \tau'^2} - \dfrac{\gamma\alpha^2}{\gamma-\beta(\gamma-1)}\dfrac{\partial^2 p^*}{\partial \eta_j^2} = 0, & \text{(B23)} \\ \dfrac{\partial^2 u_i^{(1)}}{\partial \tau'^2} - \dfrac{\gamma\alpha^2}{\gamma-\beta(\gamma-1)}\dfrac{\partial^2 u_j^{(1)}}{\partial \eta_i \partial \eta_j} = -\dfrac{(\gamma-1)\alpha^2}{\gamma-\beta(\gamma-1)}\left[\dfrac{1}{\mathrm{Pr}}\dfrac{\partial^2}{\partial \eta_i \partial \eta_j}\left(\lambda\dfrac{\partial T^{(1)}}{\partial \eta_j}\right) + \dfrac{\partial \dot{q}}{\partial \eta_i}\right]. & \text{(B24)} \end{cases}$$

The non-dimensional speed of sound in equations (B23)-(B24) is:

$$c = \frac{1}{(\alpha\varepsilon)}\sqrt{\frac{\gamma\alpha^2}{\gamma-\beta(\gamma-1)}} = \frac{c_0}{\sqrt{\gamma-\beta(\gamma-1)}}.$$

Since ASR modifications are introduced in order to reduce the speed of sound by an arbitrary factor α, we find that the parameter β must be selected as follows:

$$\sqrt{\gamma-\beta(\gamma-1)} = \alpha \;\Rightarrow\; \beta = \frac{\gamma-\alpha^2}{\gamma-1}.$$

The corresponding expression for the ASR-modified temperature equation is:

$$\rho c_p\left[\frac{\partial T}{\partial t} + u_j\frac{\partial T}{\partial x_j}\right] - \left(\frac{\gamma-\alpha^2}{\gamma-1}\right)\left[\frac{\partial p}{\partial t} + u_j\frac{\partial p}{\partial x_j}\right] = \tau_{ij}\frac{\partial u_i}{\partial x_j} + \frac{\partial}{\partial x_j}\left(\lambda\frac{\partial T}{\partial x_j}\right) + \dot{q}\,, \qquad \text{(B25)}$$

where equations are now written in dimensional form. With the full multi-component gas effects included, the equation becomes:

$$\rho c_p\left[\frac{\partial T}{\partial t} + u_j\frac{\partial T}{\partial x_j}\right] - \left(\frac{\gamma-\alpha^2}{\gamma-1}\right)\left[\frac{\partial p}{\partial t} + u_j\frac{\partial p}{\partial x_j}\right] = \tau_{ij}\frac{\partial u_i}{\partial x_j} - \frac{\partial q_j}{\partial x_j} + \sum_{k=1}^{N_S} h_k\frac{\partial}{\partial x_j}(\rho Y_k V_{k,j}) - \sum_{k=1}^{N_S} h_k\dot{\omega}_k. \qquad \text{(B26)}$$

This equation is the ASR-modified version of equation (A2). The corresponding ASR-modified version of equation (A4) is:

$$\frac{\partial p}{\partial t} + u_j\frac{\partial p}{\partial x_j} + \frac{\gamma p}{\alpha^2}\frac{\partial u_j}{\partial x_j} = \frac{(\gamma-1)}{\alpha^2}\left[\tau_{ij}\frac{\partial u_i}{\partial x_j} - \frac{\partial q_j}{\partial x_j} - \sum_{k=1}^{N_S}\left(h_k - \frac{Mc_pT}{M_k}\right)\left(-\frac{\partial}{\partial x_j}(\rho Y_k V_{k,j}) + \dot{\omega}_k\right)\right], \qquad \text{(B27)}$$

and the corresponding equation for total energy is identical to equation (2.12):

$$\frac{\partial}{\partial t}(\rho E)+\frac{\partial}{\partial x_j}(\rho E u_j)=-\frac{\partial}{\partial x_j}(p u_j)+\frac{\partial}{\partial x_j}(\tau_{ij}u_i)-\frac{\partial q_j}{\partial x_j}+\rho g_j u_j-\left(\frac{\alpha^2-1}{\gamma-1}\right)\left[\frac{\partial p}{\partial t}+u_j\frac{\partial p}{\partial x_j}\right],$$

or, after using Eq. (B27):

$$\left.\begin{aligned}\frac{\partial}{\partial t}(\rho E)+\frac{\partial}{\partial x_j}(\rho E u_j)=&-\frac{\partial}{\partial x_j}(p u_j)+\frac{\partial}{\partial x_j}(\tau_{ij}u_i)-\frac{\partial q_j}{\partial x_j}+\rho g_j u_j\\&+\left(1-\frac{1}{\alpha^2}\right)\frac{\gamma p}{\gamma-1}\frac{\partial u_j}{\partial x_j}\\&-\left(1-\frac{1}{\alpha^2}\right)\left[\tau_{ij}\frac{\partial u_i}{\partial x_j}-\frac{\partial q_j}{\partial x_j}-\sum_{k=1}^{N_s}\left(h_k-\frac{Mc_pT}{M_k}\right)\left(-\frac{\partial}{\partial x_j}(\rho Y_k V_{k,j})+\dot{\omega}_k\right)\right]\end{aligned}\right\}\quad\text{(B28)}$$

In conclusion, the analysis performed in this Appendix shows how the ASR modifications proposed in Section 2.2 may be derived from a mathematically rigorous expansion of the governing equations under weak compressibility conditions. The ASR modifications are shown to achieve the intended decrease in acoustic speeds while preserving the leading order slow flow dynamics. It is important to also recognize that the scope of the asymptotic analysis is limited ("nearly incompressible" flow conditions, homogeneous reference state, simplified description of combustion, no specific treatment of chemical time scales); it is performed in fact far from combustion conditions. Future work will be aimed at removing some of those limitations.

C: An Extension of the Burke-Schumann Solution

The diffusion flame structure near a solid wall surface may be significantly different from that found in traditional wall-free configurations. We discuss in this appendix some of the complications found in the description of diffusion flames evolving near

cold wall boundaries. We limit our discussion to the classical Burke-Schumann theoretical framework for non-premixed combustion, in which equilibrium chemistry is assumed and the flame is controlled by the fuel-air mixing process [22, 54, 147]. Furthermore, we limit our discussion to the flame-wall configuration of figure 6-2, in which deviations from adiabatic behavior is due to convective heat transfer at the wall, with the wall located at the $y = 0$ boundary. Equal molecular diffusion coefficients for mass and thermal energy are also assumed, and following standard practice, a non-dimensional fuel-air mixing variable, known as the mixture fraction and noted Z, is used as principal variable:

$$Z = \frac{Y_{C_2H_4} - (Y_{O_2} / r_s) + (Y_{O_2}^{\infty} / r_s)}{Y_{C_2H_4}^{\infty} + (Y_{O_2}^{\infty} / r_s)}, \tag{C1}$$

where $Y_{C_2H_4}^{\infty}$ is the fuel mass fraction in the fuel supply stream; $Y_{O_2}^{\infty}$ the oxygen mass fraction in the air free stream; and r_s the stoichiometric oxygen-to-fuel mass ratio. Z is a passive scalar with well-defined boundary conditions: $Z = 0$ in the air stream; $Z = 1$ in the fuel stream; and $\partial Z / \partial y = 0$ at the wall. In the Burke-Schumann framework, the full reactive mixture composition is uniquely described in terms of Z; for instance, the fuel and oxygen mass fractions are given by:

$$\begin{cases} Y_{C_2H_4} = 0, & Y_{O_2} = Y_{O_2}^{\infty}(1 - \dfrac{Z}{Z_{st}}), & 0 \le Z \le Z_{st}, \\ Y_{C_2H_4} = Y_{C_2H_4}^{\infty} \dfrac{(Z - Z_{st})}{(1 - Z_{st})}, & Y_{O_2} = 0, & Z_{st} \le Z \le 1, \end{cases} \tag{C2}$$

where Z_{st} is the stoichiometric value of mixture fraction, $Z_{st} = Y_{O_2}^{\infty} / (r_s Y_{C_2H_4}^{\infty} + Y_{O_2}^{\infty})$.

We now turn to the problem of describing the fluid temperature variations. Following the classical Burke-Schumann theory, we consider some alternative

definitions of mixture fraction using fuel-temperature or oxygen-temperature mixing variables:

$$\begin{cases} Z_2 = \dfrac{Y_{C_2H_4}}{Y^{\infty}_{C_2H_4}} + \dfrac{c_p(T - T^{\infty})}{Y^{\infty}_{C_2H_4}\Delta H_c}, \\ Z_3 = (1 - \dfrac{Y_{O_2}}{Y^{\infty}_{O_2}}) - \dfrac{c_p(T - T^{\infty})}{(Y^{\infty}_{O_2}/r_s)\Delta H_c}, \end{cases} \tag{C3}$$

where T^{∞} is the air free stream temperature (assumed equal to the fuel supply stream temperature); and c_p the specific heat of the reactive mixture at constant pressure (assumed constant). Z_2 and Z_3 satisfy the same convection-diffusion equation that Z does; these variables also satisfy the same well-defined boundary conditions in the reactants supply streams: $Z_2 = Z_3 = 0$ in the air stream; $Z_2 = Z_3 = 1$ in the fuel stream. The wall boundary conditions, however, may or may not be the same as that for Z.

Let us first consider the adiabatic wall case. In this case, the wall boundary conditions for Z_2 and Z_3 are identical to that for Z, $\partial Z_2 / \partial y = \partial Z_3 / \partial y = 0$, and we have the trivial result $Z = Z_2 = Z_3$. This result leads in turn to the classical Burke-Schumann temperature solution in which T is a piecewise linear function of Z [22, 54, 147]:

$$\begin{cases} T^{ad} = T^{\infty} + (\dfrac{Y^{\infty}_{C_2H_4}\Delta H_c}{c_p})Z, & 0 \le Z \le Z_{st}, \\ T^{ad} = T^{\infty} + (\dfrac{Y^{\infty}_{O_2}\Delta H_c}{r_s c_p})(1 - Z), & Z_{st} \le Z \le 1. \end{cases} \tag{C4}$$

In equation (C4) and in what follows, we use the *ad* superscript to refer to this adiabatic Burke-Schumann solution, $T^{ad}(Z)$. Equations (C2) and (C4) show that in the adiabatic case, the Z-structures of the wall-flame and wall-free flame are identical.

Next we consider the case of a cold wall surface with a prescribed temperature, $T(x,0,t) = T_w$. In that case, Z_2 and Z_3 are found to satisfy more complex wall boundary conditions:

$$\begin{cases} \dfrac{\partial Z_2}{\partial y} = -\dfrac{(c_p/\lambda)}{Y^{\infty}_{C_2H_4}\Delta H_c}\dot{q}''_w, \\ \dfrac{\partial Z_3}{\partial y} = +\dfrac{(c_p/\lambda)}{(Y^{\infty}_{O_2}/r_s)\Delta H_c}\dot{q}''_w, \end{cases} \tag{C5}$$

where λ is the mixture thermal conductivity, and $\dot{q}''_w$ the solid-to-gas heat flux ($\dot{q}''_w$ is negative in the present problem). The boundary conditions in equation (C5) differ from the zero normal-gradient condition satisfied by Z. The implications are then two-fold: first, Z, Z_2 and Z_3 are not identical variables; and second, the temperature is not a function of Z only, as was the case in equation (C4).

The deviations of Z_2 and Z_3 from Z may in fact be interpreted as a direct measure of the amount of heat loss resulting from the wall cooling process. Before we make that point, it is worth noting that Z, Z_2 and Z_3 are simply related by the following relationship:

$$Z = Z_3 \times Z_{st} + Z_2 \times (1 - Z_{st}) . \tag{C6}$$

In the following, we stop discussing Z_2 and use Z and Z_3 as principal variables. Combining the definition of Z_3 in equation (C3) with the Z-variations of oxygen mass fraction in equation (C2), the temperature variations under non-adiabatic combustion conditions may be expressed as:

$$\begin{cases} T = T^{\infty} + (\dfrac{Y^{\infty}_{O_2}\Delta H_c}{r_s c_p})(\dfrac{Z}{Z_{st}} - Z_3), & 0 \le Z \le Z_{st}, \\ T = T^{\infty} + (\dfrac{Y^{\infty}_{O_2}\Delta H_c}{r_s c_p})(1 - Z_3), & Z_{st} \le Z \le 1, \end{cases} \tag{C7}$$

where T is now described as a function of Z and Z_3. Equation (C7) may be re-cast in yet another form, in which temperature is expressed as the sum of the adiabatic Burke-Schumann solution plus a perturbation:

$$T = T^{ad}(Z) - (\frac{Y_{O_2}^{\infty}\Delta H_c}{r_s c_p})(Z_3 - Z). \quad \text{(C8)}$$

In this expression, temperature is now described as a function of both the fuel-air-based mixture fraction Z and the difference (Z_3-Z). The role of the latter quantity is now more readily understood: under adiabatic conditions, (Z_3-Z) = 0 and $T = T^{ad}(Z)$, whereas under non-adiabatic conditions, (Z_3-Z) $\neq$ 0 and $T \leq T^{ad}(Z)$.

An alternative form of equation (C8) is:

$$(Z_3 - Z) = \frac{T^{ad}(Z) - T}{T_{st}^{ad} - T^{\infty}} \times (1 - Z_{st}) \quad \text{(C9)}$$

where T_{st}^{ad} is the adiabatic flame temperature, $T_{st}^{ad} = T^{ad}(Z_{st})$. Equation (C8) shows that the maximum value of (Z_3-Z) is (1-Z_{st}), and therefore suggests using the following re-normalization:

$$H_m = \frac{(Z_3 - Z)}{(1 - Z_{st})} = \frac{T^{ad}(Z) - T}{T_{st}^{ad} - T^{\infty}} \quad \text{(C10)}$$

where H_m is a non-dimensional heat loss variable that varies between 0 and 1, is equal to 0 under adiabatic conditions, and is positive otherwise.

A similar quantity was previously introduced in reference [149, 150] in two different studies of non-adiabatic diffusion flames. The flame configuration studied in [149] includes radiative heat losses, while the configuration studied in [150] features

convective wall cooling. The quantity proposed in [149, 150] is called the excess enthalpy variable and is noted H. H is defined as:

$$H = \frac{c_p (T - T^\infty)}{\Delta H_c} \left(\frac{1}{Y^\infty_{C_2H_4}} + \frac{1}{(Y^\infty_{O_2} / r_s)} \right) + \frac{Y_{C_2H_4}}{Y^\infty_{C_2H_4}} + \frac{Y_{O_2}}{Y^\infty_{O_2}} - 1 \qquad \text{(C11)}$$

Using equations (C2), (C4) and (C10), it is straightforward to show that $H = -H_m$. H is therefore a non-dimensional quantity that varies between (-1) and 0, is equal to 0 under adiabatic conditions, and is negative otherwise. In the main body of the text, we follow the choice made in [149, 150] and use H to describe the modifications in flame structure due to the presence of a cold wall surface.

In conclusion, the Burke-Schumann temperature variations are given by the following two-parameter expression:

$$T(Z, H) = T^{ad}(Z) + H \times (T^{ad}_{st} - T^\infty) \qquad \text{(C12)}$$

where $(-1) \leq H \leq 0$, and where $T^{ad}(Z)$ is given by equation (C4) and $T^{ad}_{st} = T^{ad}(Z_{st})$. Equations (C2) and (C12) provide a complete description of the flame structure under non-adiabatic conditions, in the limit of infinitely fast chemistry.

Bibliography

1. Moin, P., Mahesh, K., *Direct Numerical Simulation: a Tool in Turbulence Research.* Annual Review of Fluid Mechanics, 1998. **30**: p. 539-578.
2. Piomelli, U., *Large-eddy and direct simulation of turbulent flows*, in *Lecture series on "Introduction to Turbulence Modeling"*. 2004, von Karman Institute for Fluid Dynamics.
3. Rogallo, R., Moin, P., *Numerical Simulation of Turbulent Flows.* Ann. Rev. Fluid Mech., 1984. **16**: p. 99-137.
4. Piomelli, U., and Balaras, E., *Wall-layer models for large-eddy simulations.* Annu. Rev. Fluid Mech., 2002. **34**: p. 349-374.
5. Forsythe, J.R., Squires, K.D., Wurtzler, K. E., and Spalart, P. R., *Detached-eddy simulation of fighter aircraft at high alpha.* AIAA Paper 2002-0591, 2002.
6. Selle, L., Lartigue, G., Poinsot, T., Koch, R., Schildmacher, K.U., Krebs, W., Prade, B., Kaufmann, P., and Veynante, D., *Compressible large eddy simulation of turbulent combustion in complex geometry on unstructured meshes.* Combust. Flame, 2004. **137**(4): p. 489-505.
7. McGrattan, K., *Fire dynamics simulator (Version 4) technical reference guide.* NIST Special Publication 1018, 2004.
8. Mansour, N.N., Wray, A. A., *Decay of isotropic turbulence at low Reynolds number.* Phys. Fluids, 1994. **6**(2): p. 808-814.

9. Spalart, P.R., *Direct numerical simulation of a turbulent boundary layer up to $Re_\theta = 1410$.* J. Fluid Mech., 1988. **187**: p. 61.

10. Kim, J., Moin, P., and Moser, R., *Turbulence statistics in fully developed channel flow at low Reynolds number.* J. Fluid Mech., 1987. **177**: p. 133-166.

11. Moser, R.D., Kim, J., and Mansour, N. N., *Direct numerical simulation of turbulent channel flow up to $Re_\tau = 590$.* Phys. Fluids, 1999. **11**(4): p. 943-945.

12. Poinsot, T., Candel, S., Trouvé, A., *Applications of Direct Numerical Simulation to Premixed Turbulent Combustion.* Prog. Energy Combust. Sci., 1996. **21**: p. 531-576.

13. Vervisch, L., Poinsot, T., *Direct Numerical Simulation of Non-Premixed Turbulent Flames.* Annual Review of Fluid Mechanics, 1998. **30**: p. 655-691.

14. Rutland, C.J., Trouvé, A., *Direct simulations of premixed turbulent flames with nonunity Lewis numbers.* Combustion and Flame, 1993. **94**: p. 41-57.

15. Lee, Y.Y., Pope, S. B., *Nonpremixed Turbulent Reacting Flow near Extinction.* Combustion and Flame, 1995. **101**: p. 501-528.

16. Bruneaux, G., Akselvoll, K., Poinsot, T., Ferziger, J. H., *Flame-Wall Interaction Simulation in a Turbulent Channel Flow.* Combustion and Flame, 1996. **107**: p. 27-44.

17. Sripakagorn, P., Mitarai, S., Kosaly, G., Pitsch, H., *Extinction and Reignition in a Diffusion Flame: a Direct Numerical Simulation Study.* J. Fluid Mech., 2004. **518**: p. 231-259.

18. Poinsot, T., Veynante, D., Candel, S., *Quenching processes and premixed turbulent combustion diagrams.* J. Fluid Mech., 1991. **228**: p. 561-606.

19. Baum, M., Poinsot, T., Haworth, D. C., Darabiha, N., *Direct numerical simulation of $H_2/O_2/N_2$ flames with complex chemistry in two-dimensional turbulent flows.* J. Fluid Mech., 1994. **281**: p. 1-32.

20. Echekki, T., Chen, J. H., *Direct numerical simulation of autoignition in nonhomogeneous hydrogen-air mixtures.* Combustion and Flame, 2003. **134**: p. 169-191.

21. Hawkes, E.R., Chen, J. H., *Direct numerical simulation of hydrogen-enriched lean premixed methane-air flames.* Combustion and Flame, 2004. **138**: p. 242-258.

22. Williams, F.A., *Combustion Theory*. 1985, Menlo Park, CA: Benjamin Cummings.

23. Veynante, D., Trouvé, A., Bray, K. N. C. and Mantel, T., *Gradient and counter-gradient scalar transport in turbulent premixed flames.* J. Fluid Mech., 1997. **332**: p. 263-293.

24. Peters, N., *Laminar flamelet concepts in turbulent combustion.* Proc. Combust. Inst., 1986. **21**: p. 1231-1250.

25. Trouvé, A., and Poinsot, T., *The evolution equation for the flame surface density in turbulent premixed combustion.* J. Fluid Mech., 1994. **278**: p. 1-31.

26. Zhang, S., and Rutland, C. J., *Premixed flame effects on turbulence and pressure-related term.* Combustion and Flame, 1995. **102**: p. 447-461.

27. Chen, J.H., Kollmann, W., *Topological and geometrical properties of turbulent flames.* AIAA paper, 94-0098, 1994.

28. Bédat, B., Egolfopoulos, F. N., Poinsot, T., *Direct Numerical Simulation of Heat Release and NO_x Formation in Turbulent Nonpremixed Flames.* Combustion and Flame, 1999. **119**: p. 69-83.

29. van Kalmthout, E., Veynante, D., *Direct numerical simulations analysis of flame surface density models for nonpremixed turbulent combustion.* Phys. Fluids, 1998. **10**(9): p. 2347-2368.

30. Cuenot, B., Poinsot, T., *Effects of curvature and unsteadiness in diffusion flames. Implications for turbulent diffusion combustion.* Proc. Combust. Inst., 1994. **25**: p. 1383-1390.

31. Domingo, P.V., L., *Triple flames and partially premixed combustion in autoignition of nonpremixed mixtures.* Proc. Combust. Inst., 1996. **26**: p. 233-240.

32. Favier, V., Vervisch, L., *Edge flames and partially premixed combustion in diffusion flame quenching.* Combustion and Flame, 2001. **125**: p. 788-803.

33. Im, H.G., Chen, J. H., *Effects of flow strain on triple flame propagation.* Combust. Flame, 2001. **126**: p. 1384-1392.

34. Alshaalan, T., Rutland, C. J., *Wall Heat Flux in Turbulent Premixed Reacting Flow.* Combust. Sci. and Tech., 2002. **174**: p. 135-165.

35. Wang, Y., and Rutland, C. J., *Effect of temperature and equivalence ratio on the ignition of n-heptane fuel droplets in turbulent flow.* Proc. Combust. Inst., 2005. **30**: p. 893-900.

36. Reveillon, J.a.V., L., *Spray vaporization in nonpremixed turbulent combustion modeling: a single droplet model.* Combustion and Flame, 2000. **121**: p. 75-90.

37. *Terascale high-fidelity simulations of turbulent combustion with detailed chemistry*, SciDAC Computational Chemistry Program, DOE, Office of Basic Energy Sciences, http://purl.org/net/tstc/.

38. Kennedy, C.A., Carpenter, M. H., *A comparison of several numerical methods for the simulation of compressible shear layers.* Appl. Num. Math., 1994. **14**(4): p. 397-433.

39. Kennedy, C.A., Carpenter, M. H., Lewis, R. H., *Low-storage, explicit Runge-Kutta schemes for the compressible Navier-Stokes equations.* Appl. Num. Math., 2000. **35**(3): p. 177-219.

40. Poinsot, T., Lele, S. K., *Boundary conditions for direct simulations of compressible viscous flows.* J. Comp. Phys., 1992. **101**: p. 104-129.

41. Baum, M., Poinsot, T., Thevenin, D., *Accurate boundary conditions for multi-component reactive flows.* J. Comp. Phys., 1995. **116**(2): p. 247-261.

42. Kee, R.J., Rupley, F. M., Meeks, E., Miller, J. A., *CHEMKIN-III: a Fortran Chemical Kinetics Package for the Analysis of Gas-phase Chemical and Plasma Kinetics.* Sandia National Laboratories Report, 1996(SAND96-8216).

43. Oran, E.S., Boris, J. P., *Numerical Simulation of Reactive Flow*. 2 ed. 2001: Cambridge Univ. Press.

44. Rehm, R.G., Baum, H. R., *The equations of motion for thermally driven, buoyant flows.* J. Res. Nat. Bur. Stand., 1978. **83**: p. 297-308.

45. Majda, A., Sethian, J., *The derivation and numerical solution of the equations for zero Mach number combustion.* Combust. Sci. Technol., 1985. **42**: p. 185-205.

46. Najm, H.N., Wyckoff, P. S., Knio, O. M., *A semi-implicit numerical scheme for reacting flow. I. Stiff chemistry.* J. Comput. Phys., 1998. **143**: p. 381-402.

47. Knio, O.M., Najm, H. N., Wyckoff, P. S., *A semi-implicit numerical scheme for reacting flow. II. Operator-split formulation.* J. Comput. Phys., 1999. **154**: p. 428-467.

48. Pember, R.B., Howell, L. H., Bell, J. B., Colella, P., Crutchfield, W. Y., Fiveland, W. A., Jessee, J. P., *An adaptive projection method for unsteady, low-Mach number combustion.* Combust. Sci. Tech., 1998. **140**: p. 123-168.

49. Patnaik, G., Guirguis, R. H., Boris, J. P., Oran, E. S., *A barely implicit correction for flux-corrected transport.* J. Comput. Phys., 1987. **71**: p. 1-20.

50. Choi, Y.-H., Merkle, C. L., *The application of preconditioning in viscous flows.* J. Comput. Phys., 1993. **105**: p. 207-223.

51. Turkel, E., *Preconditioning techniques in computational fluid dynamics.* Annu. Rev. Fluid Mech., 1999. **31**: p. 385-416.

52. O'Rourke, P.J., Bracco, F. V., *Two scaling transformations for the numerical computation of multidimensional unsteady laminar flames.* J. Comput. Phys., 1979. **33**: p. 185-203.

53. Ramshaw, J.D., O'Rourke, P. J., Stein, L. R., *Pressure gradient scaling method for fluid flow with nearly uniform pressure.* J. Comput. Phys., 1985. **58**: p. 361-376.

54. Poinsot, T., Veynante, D., *Theoretical and Numerical Combustion*. 2001: Edwards.

55. Yetter, R.A., Dryer, F. L., Rabitz, H., *A comprehensive reaction mechanism for carbon monoxide/hydrogen/oxygen kinetics.* Combust. Sci. Tech., 1991. **79**: p. 97-128.

56. Tsuji, H., *Counterflow diffusion flames.* Prog. Energy Combust. Sci., 1982. **8**: p. 93-119.

57. Williams, F.A., *Progress in knowledge of flamelet structure and extinction.* Prog. Energy Combust. Sci., 2000. **26**: p. 657-682.

58. Lutz, A.E., Kee, R.J., Grcar, J.F., Rupley, F.M., *OPPDIF: A Fortran program for computing opposed-flow diffusion flames*. 1996, Sandia National Laboratories Report, SAND96-8243.

59. Mastorakos, E., Taylor, A.M.K.P., Whitelaw, J.H., *Extinction of turbulent counterflow flames with reactants diluted by hot products.* Combust. Flame, 1995. **102**: p. 101-114.

60. Blouch, J.D., Chen, J.Y., Law, C.K., *A joint scalar PDF study of nonpremixed hydrogen ignition.* Combust. Flame, 2003. **135**: p. 209-225.

61. Kitajima, A., Torikai, H., Takeuchi, M., Oya, M., *Experimental study of extinction and its quantification in laminar and turbulent counterflow CH4-N2/O2-N2 nonpremixed flames.* Combust. Flame, 2004. **137**: p. 93-108.

62. Engquist, B., Majda, A., *Absorbing Boundary Conditions for the Numerical Simulation of Waves.* Mathematics of Computation, 1977. **31**(139): p. 629-651.

63. Hedstrom, G.W., *Nonreflecting Boundary Conditions for Nonlinear Hyperbolic Systems.* J. Comp. Phys., 1979. **30**: p. 222-237.

64. Thompson, K.W., *Time Dependent Boundary Conditions for Hyperbolic Systems.* J. Comp. Phys., 1987. **68**: p. 1-24.

65. Thompson, K.W., *Time-Dependent Boundary Conditions for Hyperbolic Systems, II.* J. Comp. Phys., 1990. **89**: p. 439-461.

66. Rudy, D., Strikwerda, J., *A Nonreflecting Outflow Boundary Condition for Subsonic Navier-Stokes Calculations.* J. Comp. Phys., 1980. **36**: p. 55-70.

67. Giles, M.B., *Nonreflecting Boundary Conditions for Euler Equation Calculations.* AIAA Journal, 1990. **28**(12): p. 2050-2058.

68. Baum, M., Poinsot, T., Thevenin, D., *Accurate Boundary Conditions for Multicomponent Reactive Flows.* J. Comp. Phys., 1994. **116**: p. 247-261.

69. Okong'o, N., Bellan, J., *Consistent boundary conditions for multicomponent real gas mixtures based on characteristic waves.* J. Comp. Phys., 1994. **176**: p. 330-344.

70. Sutherland, J.C., Kennedy, C. A., *Improved Boundary Conditions for Viscous, Reacting, Compressible Flows.* J. Comp. Phys., 2003. **191**: p. 501-524.

71. Prosser, R., Schlüter, J., *Toward improved boundary conditions DNS and LES of turbulent subsonic flows.* Proc. Summer Program, Center for Turbulence Research, Stanford University, 2004: p. 395-410.

72. Colonius, T., *Modeling Artificial Boundary Conditions for Compressible Flow.* Annu. Rev. Fluid Mech., 2004. **36**: p. 315-345.

73. Schonfeld, T., Poinsot, T., *Influence of boundary conditions in LES of premixed combustion instability.* Center for Turbulent Research Annual Review Briefs, 1999: p. 73-84.

74. Yoo, C.S., Wang, Y., Trouvé, A., Im, H.G., *Characteristic boundary conditions for direct simulations of turbulent counterflow flames.* to be appeared in Combust. Theory and Modelling, 2005.

75. Nicoud, F., *Defining Wave Amplitude in Characteristic Boundary Conditions.* J. Comp. Phys., 1999. **149**: p. 418-422.

76. Mueller, M.A., Yetter, R.A., Dryer, F.L., *Measurement of the rate constant for H+O2+ M -> HO2+M (M = N2, Ar) using kinetic modeling of the high-pressure H2/O2/NOx reaction.* Proc. Combust. Inst., 1998. **27**: p. 177-184.

77. Passot. T., P., A., *Numerical simulation of compressible homogeneous flows in the turbulent regime.* J. Fluid. Mech., 1987. **118**: p. 441-466.

78. Lee, S., Lele, S. K., Moin, P., *Simulation of Spatially Evolving Turbulence and the Applicability of Taylor's Hypothesis in Compressible Flow.* Phys. Fluids A, 1992. **4**(7): p. 1521-1530.

79. Hamins, A., *Soot*, in *Environmental Implications of Combustion Processes*, I.K. Puri, Editor. 1993, CRC Press. p. 71-96.

80. Guo, H., Liu, F., Smallwood, G., J., *Soot and NO formation in counterflow ethylene/oxygen/nitrogen diffusion flames.* Combust. Theory Modelling, 2004. **8**: p. 475-489.

81. Kennedy, I.M., *Models of Soot Formation and Oxidation.* Prog. Energy Combust. Sci., 1997. **23**: p. 95-132.

82. Bockhorn, H., ed. *Soot Formation in Combustion*. 1994, Springer-Verlag: Berlin.

83. Frenklach, M., Wang, H., *Detailed mechanism and modeling of soot particle formation*, in *Soot formation in combustion*, H. Bockhorn, Editor. 1994, Springer-Verlag. p. 165-192.

84. Smooke, M.D., Mcenally, C. S., Pfefferle, L. D., Hall, R. J., Colket, M. B., *Computational and experimental study of soot formation in a coflow, laminar diffusion flame.* Combust. Flame, 1999. **117**: p. 117-139.

85. Moss, J.B., Stewart, C. D., Syed, K. J. *Flowfield Modelling of Soot Formation at Elevated Pressure*. in *Twenty-Second Symposium (International) on Combustion*. 1988: The Combustion Institute, Pittsburgh, PA.

86. Syed, K.J., Stewart, C. D. Moss, J. B. *Modelling Soot Formation and Thermal Radiation in Buoyant Turbulent Diffusion Flames*. in *Twenty-Third Symposium (International) on Combustion*. 1990: The Combustion Institute, Pittsburgh, PA.

87. Moss, J.B., Stewart, C. D., Young, K. J., *Modeling Soot Formation and Burnout in a High Temperature Laminar Diffusion Flame Burning under Oxygen-Enriched Conditions.* Combustion and Flame, 1995. **101**: p. 491-500.

88. Friedlander, S.K., *Smoke Dust and Haze-Fundamentals of Aerosol Dynamics*. 2 ed. 2000: Oxford University Press.

89. Kaplan, C.R., Shaddix, C. R., Smyth, K. C., *Computations of Enhanced Soot Production in Time-Varying CH_4/Air Diffusion Flames.* Combustion and Flame, 1996. **106**: p. 392-405.

90. Kaplan, C.R., Patnaik, G., Kailasanath, K., *Universal Relationships in Sooting Methane-Air Diffusion Flames.* Combust. Sci. Tech., 1998. **131**: p. 39-65.

91. Kaplan, C.R., Kailasanath, K., *Flow-field Effects on Soot Formation in Normal and Inverse Methane-Air Diffusion Flames.* Combustion and Flame, 2001. **124**: p. 275-294.

92. Leung, K.M., Lindstedt, R. P. and Jones, W. P., *A Simplified Reaction Mechanism for Soot Formation in Nonpremixed Flames.* Combustion and Flame, 1991. **87**: p. 289-305.

93. Fairweather, M., Jones, W. P., Ledin, H. S., Lindstedt, R. P. *Predictions of Soot Formation in Turbulent Non-premixed Propane Flame*. in *Twenty-Fourth Symposium (International) on Combustion*. 1992: The Combustion Institute, Pittsburgh, PA.

94. Lindstedt, P.R., *Simplified soot nucleation and surface growth steps for non-premixed flames*, in *Soot Formation in Combustion*, H. Bockhorn, Editor. 1994, Springer-Verlag: Berlin. p. 417-439.

95. Fairweather, M., Jones, W. P., Lindstedt, R. P., *Predictions of radiative transfer from a turbulent reacting jet in a cross-wind.* Combustion and Flame, 1992. **89**: p. 45-64.

96. Ezekoye, O.A., Zhang, Z., *Soot Oxidation and Agglomeration Modeling in a Microgravity Diffusion Flame.* Combustion and Flame, 1997. **110**: p. 127-139.

97. Brookes, S.J., Moss, J. B., *Prediction of Soot and Thermal Radiation Properties in Confined Turbulent Jet Diffusion Flames.* Combustion and Flame, 1999. **116**: p. 486-503.

98. Liu, F.G., H., Smallwood, G. J., Gulder, O. L., *Numerical modelling of soot formation and oxidation in laminar coflow non-smoking and smoking ethylene diffusion flames.* Combust. Theory Modelling, 2003. **7**: p. 301-315.

99. Vandsburger, U., Kennedy, I., Glassman, I., *Sooting Counterflow Diffusion Flames with Varying Oxygen Index.* Combustion Science and Technology, 1984. **39**: p. 263-285.

100. Westbrook, C.K., Dryer, F. L., *Simplified Reaction Mechanism for the Oxdiation of Hydrocarbon Fuels in Flames.* Combust. Sci. Tech., 1981. **27**: p. 31-43.

101. Hwang, J.Y., Chung, S. H., *Growth of soot particles in counterflow diffusion flames of ethylene.* Combust. Flame, 2001. **125**: p. 752-762.

102. Tieszen, S.R., *On the Fluid Mechanics of Fires.* Annual Review of Fluid Mechanics, 2001. **33**: p. 67-92.

103. Fernandez-Pello, A., C., *Flame spread modeling.* Combustion Science and Technology, 1984. **39**: p. 119-134.

104. Karlsson, B., Quintiere, J. G., *Enclosure Fire Dynamics*. 2000: CRC Press.

105. Wang, J., Niioka, T., *The effect of radiation reabsorption on NO formation in CH_4/air counterflow diffusion flames.* Combut. Theory Modelling, 2001. **5**: p. 385-398.

106. Frank, J.H., Barlow, R. S., Lundquist, C., *Radiation and Nitric Oxide Formation in Turbulent Non-premixed Jet Flames.* Proceedings of the Combustion Institute, 2000. **28**: p. 447-454.

107. Ju, Y., Guo, H., Maruta, K., Liu, F., *On the Extinction Limit and Flammability Limit of Non-adiabatic Stretched Methane-air Premixed Flames.* Journal of Fluid Mechanics, 1997. **342**: p. 315-334.

108. Wu, Y., Haworth, D. C., Modest, M. F., Cuenot, B. *Direct Numerical Simulation of Turbulence/Radiation Interaction in Premixed Combustion Systems*. in *Thirtieth Symposium (International) on Combustion*. 2004: The Combustion Institute, Pittsburgh, PA.

109. Coelho, P.J., Teerling, O. J., Roekaerts, D., *Spectral Radiative Effects and Turbulence/Radiation Interaction in a Non-luminous Turbulent Jet Diffusion Flame.* Combustion and Flame, 2003. **133**: p. 75-91.

110. Modest, M.F., *Radiative Heat Transfer*. 2 ed. 2003, San Diego, CA: Academic Press.

111. Viskanta, R., Mengüç, M. P., *Radiation Heat Transfer in Combustion Systems.* Prog. Energy Combust. Sci., 1987. **13**: p. 97-160.

112. Carvalho, M.G., Farias, T. L., *Modeling of Heat Transfer in Radiating and Combusting Systems.* Trans IchemE, 1998. **76**(Part A): p. 175-184.

113. Fiveland, W.A., *Discrete-ordinates Solutions of the Radiative Transport Equation for Rectangular Enclosures.* Journal of Heat Transfer, 1984. **106**: p. 699-706.

114. Lockwood, F.C., Shah, N. G. *A New Radiation Solution Method for Incorporation in General Combustion Prediction Procedures*. in *Eighteenth Symposium (International) on Combustion*. 1981: The Combustion Institute, Pittsburgh, PA.

115. Selcuk, N., Kayakol, N., *Evaluation of discrete ordinates method for radiative transfer in rectangular furnaces.* Int. J. Heat Mass Transfer, 1997. **40**(2): p. 213-222.

116. Yan, Z.H., *Parallel Computation of Turbulent Combustion and Flame Spread in Fires.* Numerical Heat Transfer B, 2002. **41**: p. 191-208.

117. Chi, J.C., Lee, H. S., Patankar, S. V., *Ray effect and false scattering in the discrete ordinates method.* Numerical Heat Transfer B, 1993. **24**: p. 373-389.

118. Coelho, P.J., Carvalho, M. G., *A Conservative Formulation of the Discrete Transfer Method.* ASME Journal of Heat Transfer, 1997. **76**: p. 919-929.

119. Cumber, P.S., *Improvements to the Discrete Transfer Method of Calculating Radiative Heat Transfer.* Int. J. Heat Mass Transfer, 1995. **38**(12): p. 2251-2258.

120. Versteeg, H.K., Henson, J. C., Malalasekera, *Approximation Errors in the Heat Flux Integral of the Discrete Transfer Method, Part 1: Transparent Media.* Numerical Heat Transfer B, 1999. **36**: p. 387-407.

121. Versteeg, H.K., Henson, J. C., Malalasekera, *Approximation Errors in the Heat Flux Integral of the Discrete Transfer Method, Part 2: Participating Media.* Numerical Heat Transfer B, 1999. **36**: p. 409-432.

122. Versteeg, H.K., Henson, J. C., Malalasekera, *Spatial Discretization Errors in the Heat Flux Integral of the Discrete Transfer Method.* Numerical Heat Transfer B, 2000. **38**: p. 333-352.

123. Cumber, P.S., *Ray Effect Mitigation in Jet Fire Radiation Modelling.* Int. J. Heat Mass Transfer, 2000. **43**: p. 935-943.

124. Versteeg, H.K., Henson, J. C., Malalasekera, *An Adaptive Angular Quadrature for the Discrete Transfer Method Based on Error Estimation.* Journal of Heat Transfer, 2003. **125**: p. 301-311.

125. Novo, P.J., Coelho, P. J.,Carvalho, M. G., *Parallelization of the Discrete Transfer Method.* Numerical Heat Transfer B, 1999. **35**: p. 137-161.

126. Lu, J.H., Ezekoye, O., Greif, R., Sawyer, R. F., *Unsteady Heat Transfer During Side Wall Quenching of a Laminar Flame.* Proceedings of the Combustion Institute, 1990. **23**: p. 441-446.

127. Ezekoye, O., Greif, R., Sawyer, R. F., *Increased Surface Temperature Effects on Wall Heat Transfer During Unsteady Flame Quenching.* Proceedings of the Combustion Institute, 1992. **28**: p. 447-454.

128. Poinsot, T., Haworth, D., Bruneaux, G., *Direct Simulation and Modelling of Flame-wall Interaction for Premixed Turbulent Combustion.* Combustion and Flame, 1993. **95**: p. 118-133.

129. Wichman, I.S., Bruneaux, G., *Head-on Quenching of a Premixed Flame by a Cold Wall.* Combustion and Flame, 1995. **103**: p. 296-310.

130. Popp, P., Smooke, M., and Baum, M., *Heterogeneous/homogeneous reaction and transport coupling during flame-wall interaction.* Proc. Combust. Inst., 1996. **26**: p. 2693-2700.

131. Popp, P., Baum, M., *Analysis of Wall Heat Fluxes, Reaction Mechanisms, and Unburnt Hydrocarbons during the Head-on Quenching of a Laminar Methane Flame.* Combustion and Flame, 1997. **108**: p. 327-348.

132. Bruneaux, G., Poinsot, T. and Ferziger, J. H., *Premixed flame-wall interaction in a turbulent channel flow: budget for the flame surface density evolution equation and modelling.* J. Fluid Mech., 1997. **349**: p. 191-219.

133. Alshaalan, T., Rutland, C. J., *Turbulence, scalar transport, and reaction rates in flame-wall interactions.* Proc. Combust. Inst., 1998. **27**: p. 793-799.

134. Aghalayam, P., Bui, P. A. and Vlachos, D. G., *The role of radical wall quenching in flame stability and wall heat flux: hydrogen-air mixtures.* Combust. Theory Modelling, 1998. **2**: p. 515-530.

135. Raimondeau, S., Norton, D., Vlachos, D. G. and Masel, R. I., *Modeling of high-temperature microburners.* Proc. Combust. Inst., 2002. **29**: p. 901-907.

136. Dabireau, F., Cuenot, B., Vermorel, O., Poinsot, T., *Interaction of Flames of $H_2 + O_2$ with Inert Walls.* Combustion and Flame, 2003. **135**: p. 123-133.

137. De Lataillade, A., Dabireau, F., Cuenot, B., Poinsot, T., *Flame/wall interaction and maximum wall heat fluxes in diffusion burners.* Proceedings of the Combustion Institute, 2002. **29**: p. 775-779.

138. Babrauskas, V., *Specimen heat fluxes for bench-scale heat release rate testing.* Proc. Interflam, 1993: p. 57-74.

139. Lattimer, *Heat Fluxes from Fires to Surfaces*, in *SFPE Handbook of Fire Protection Engineering*. 2003, NFPA. p. 269-296.

140. Ahmad, T., Faeth, G. M., *An investigation of the laminar overfire region along upright surfaces.* J. Heat Transfer, 1978. **100**: p. 112-119.

141. Ahmad, T., Faeth, G. M., *Turbulent Wall Fires.* Proc. Combust. Inst., 1979. **17**: p. 1149-1160.

142. Quintiere, J.G., Cleary, T. G., *Heat Flux from Flames to Vertical Surfaces.* Fire Technology, 1994. **30**: p. 209-231.

143. Back, G., Beyler, C., DiNenno, P. and Tatem, P., *Wall incident heat flux distributions resulting from an adjacent fire.* Proc. Fourth Intl. Symp. Fire Safety Sci., IAFSS, 1994: p. 241-252.

144. You, H.Z., Faeth, G. M., *Ceiling Heat Transfer during Fire Plume and Fire Impingement.* Fire and Materials, 1979. **3**: p. 140-147.

145. Kokkala, M.A., *Experimental study of heat transfer to ceiling from an impinging diffusion flame.* Proc. Third Intl. Symp. Fire Safety Sci., IAFSS, 1991: p. 261-270.

146. San-Diego-Mech, http://maeweb.ucsd.edu/combustion/cermech/.

147. Veynante, D., Vervisch, L., *Turbulent combustion modeling.* Prog. Energy Combust. Sci., 2002. **28**: p. 193-266.

148. Ghoniem, A.F., Soteriou, M. C., Knio, O. M. and Cetegen, B., *Effect of steady and periodic strain on unsteady flamelet combustion.* Proc. Combust. Inst., 1992. **24**: p. 223-230.

149. Ray, A., Wichman, I. S., *Influence of Fuel-Side Heat Loss on Diffusion Flame Extinction.* International Journal of Heat and Mass Transfer, 1998. **41**: p. 3075-3085.

150. Vance, R., Wichman, I. S., *Heat Transfer Analysis of a Diffusion Flame Leading Edge Near a Cold, Chemically Inert Surface.* International Journal of Heat and Mass Transfer, 2000. **43**: p. 921-933.

151. Wang, Y., Trouvé, A., *Artificial Acoustic Stiffness Reduction in Fully Compressible Direct Numerical Simulation of Combustion.* Combustion Theory and Modelling, 2004. **8**: p. 633-660.

152. Wang, Y., Trouvé, A., *Direct numerical simulation of non-premixed flame-wall interaction.* submitted for publication to Combustion and Flame, 2005.

153. Zank, G., P., Matthaeus, W. H., *The equations of nearly incompressible fluids. I. Hydrodynamics, turbulence, and waves.* Phys. Fluids A, 1991. **3**: p. 69-82.

154. Bayly, B.J., Levermore, C. D., Passot, T., *Density variations in weakly compressible flows.* Phys. Fluids A, 1992. **4**: p. 945-954.

155. Ali, G., *Low Mach number flows in time-dependent domains.* SIAM J. Appl. Math., 2003. **63**: p. 2020-2041.